

# THE OPTICAL PROPERTIES OF LUMINESCENCE CENTRES IN SILICON

Gordon DAVIES

*Physics Department, King's College London, Strand, London WC2R 2LS, UK*



NORTH-HOLLAND – AMSTERDAM

## THE OPTICAL PROPERTIES OF LUMINESCENCE CENTRES IN SILICON

Gordon DAVIES

Physics Department, King's College London, Strand, London WC2R 2LS, UK

Received May 1988

*Contents:*

1. Introduction	85	6.4. Effects of carbon during irradiation above room temperature	147
2. Relevant properties of pure silicon	87	6.5. Quantitative aspects of room temperature irradiation	147
2.1. Phonon-related properties	87	6.6. Subthreshold damage creation of photoluminescence centres	150
2.2. Electron-related properties	91		
3. Methods of experimental study	100	6.7. Heavy-particle damage	151
3.1. Photoluminescence	100	7. Vibronic properties	152
3.2. Absorption measurements and decay times	106	7.1. Basic bandshapes	152
3.3. Luminescence excitation measurements	110	7.2. Link to uniaxial stress data	156
3.4. Cathodoluminescence, electroluminescence, photo-thermal ionisation, two-beam absorption	111	7.3. Local and resonant modes	158
4. Impurities	113	7.4. Nearly degenerate excited states	161
4.1. Carbon	113	7.5. Quadratic electron-phonon coupling and isotope effects	165
4.2. Oxygen	118	8. Electronic states	167
4.3. Donors and acceptors	120	9. Closely related photoluminescent centres	172
5. Specific photoluminescence bands	128	9.1. Centres like the 969 meV centre	172
5.1. 789 meV C-O band	128	9.2. Centres like the 1018 meV centre	174
5.2. 969 meV (two-carbon atom band)	131	10. Widths of zero-phonon lines	175
5.3. 1014 meV Cu band	137	10.1. Stress-induced widths	175
5.4. 1018 meV W or I1 band	138	10.2. Isotope-induced widths	178
5.5. 1045 meV 4-Li atom complex	139	Appendix. Published photoluminescence and related electronic transitions in bulk crystalline silicon	179
6. Radiation-induced photoluminescence centres	142	References	182
6.1. Rate of primary atomic displacements by electrons	142	Notes added in proof	187
6.2. Rate of production of observable damage	144		
6.3. Effects of carbon for irradiation below room temperature	146		

*Abstract:*

Over one hundred independent photoluminescence transitions are now known in crystalline silicon. This paper begins by outlining those properties of silicon which are relevant to understanding the photoluminescence. The advantages of, and problems with, the different optical techniques are outlined. Topics discussed in detail include the quantitative understanding of the optical effects of radiation damage, and the vibronic bandshapes of the photoluminescence, including local and resonant modes, the vibronic coupling of nearly degenerate excited states and isotope effects. The link is described between the excited states of some of the centres and the band states of the silicon host lattice. Relationships within groups of similar optical centres, and the widths of the zero-phonon transitions are also discussed. Tables include a list of published photoluminescence transitions indicating their key properties.

*Single orders for this issue*

PHYSICS REPORTS (Review Section of Physics Letters) 176, Nos. 3 & 4 (1989) 83-188.

Copies of this issue may be obtained at the price given below. All orders should be sent directly to the Publisher. Orders must be accompanied by check.

Single issue price Dfl. 79.00, postage included.

## 1. Introduction

Since the mid 1970s there has been a huge increase in our understanding of photoluminescence from silicon. Applications include non-destructive measurements of the concentrations of shallow donors and acceptors (see, e.g., ref. [1]), and the detection of very low levels of carbon in silicon [2-4]. Photoluminescence also provides a probe of processes occurring within the silicon (e.g. thermal diffusion of oxygen atoms [5]) and it can indicate the state of laser annealing of an ion-implanted sample [6]. In addition, basic research is continuing rapidly into the properties of the photoluminescent centres.

This review outlines the state of work on photoluminescence centres in silicon (viewed from early 1988). It is organised as follows. Relevant properties of pure silicon are given in section 2. In section 3 the usefulness and limitations of different optical techniques are discussed. Section 4 outlines the properties of some important impurities in silicon. Representative optical centres are treated in detail in section 5. One major way of generating photoluminescence centres is by radiation damage, and this is described in section 6. The vibronic properties of the bands (their bandshapes, temperature dependences and isotope effects) are discussed in section 7. In section 8 we see that data for many centres can be rationalised by constructing electronic states from the valence and conduction band extrema. We then bring together data on different centres which form identifiable groups of closely related centres (section 9). Finally the widths of zero-phonon lines are described for the first time in section 10. The appendix lists the photoluminescence centres reported in the literature.

Throughout this review it should be remembered that the optical centres discussed are almost always those which produce sharp line spectra, for these are the spectra whose properties can be measured most accurately. Unfortunately a large fraction of the luminescence from some samples of silicon is in the form of broad featureless bands (fig. 1) and almost nothing is known about them.

Rapid developments in studying photoluminescence from silicon began in the mid-1970s. Up to then

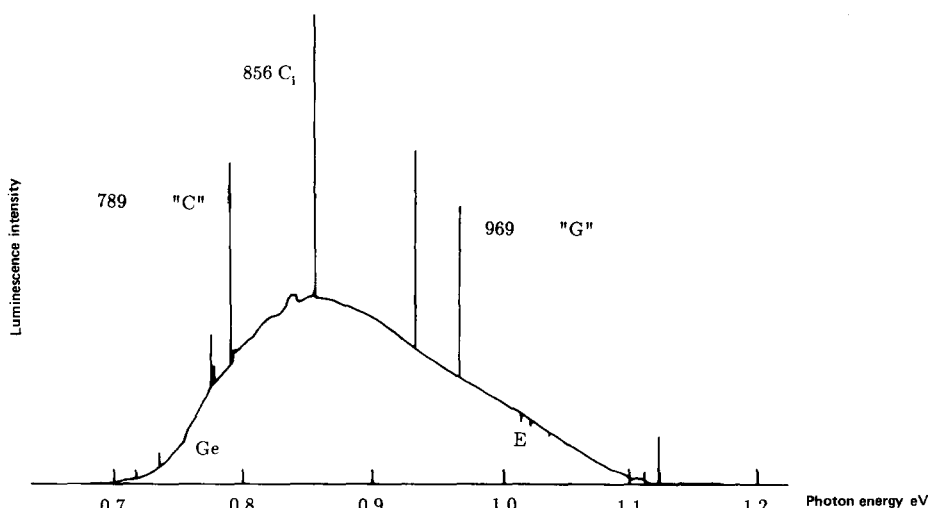


Fig. 1. Photoluminescence spectrum of float-zone silicon containing  $5.4 \times 10^{16} \text{ cm}^{-3}$  carbon atoms, after irradiation at 220 K with  $5 \times 10^{16} \text{ cm}^{-2}$  2 MeV electrons. The spectrum was recorded at 4.2 K using a Fourier transform spectrometer fitted with a germanium detector; the feature marked Ge is caused by part of the absorption edge of Ge. Sharp lines at 789, 856 and 969 meV are produced by atomic sized defects (see sections 5.1, 5.2 and 4.1.2). However, the spectrum is dominated by a broad underlying band of unknown origin. (E.C. Lightowlers, private communication 1988)

almost all the work had been done using PbS photoconductive cells. Consequently, definitive work had been carried out on only the highest-energy photoluminescence from silicon—that produced by free excitons (e.g. ref. [7]), and by the singly and multiply bound excitons trapped at shallow centres (e.g. ref. [8]). About 1976 intrinsic germanium detectors began to be used, particularly the North Coast Optical Systems detectors, which have become the standard tool in this area. An increase by several orders of magnitude became available in the signal to noise ratio.

For the first time the resolution of photoluminescence from silicon became limited by the quality of the silicon, and not by the optics (section 10). The most important application of this increase in resolution has been the detection of isotope effects in the zero-phonon lines (fig. 2), enabling unambiguous chemical identifications to be made of the optical centres. However, these improvements were limited to photon energies greater than  $\sim 0.75$  eV, the onset of high sensitivity in the germanium detectors. More recently, the power of Fourier transform spectrometers has been applied to photoluminescence (see, e.g. ref. [1]). Today spectroscopic tools are no longer the limiting factor in carrying out accurate spectroscopy in silicon.

As well as advances in conventional spectroscopy the late 1970s saw the introduction to defect work in silicon of Deep Level Transient Spectroscopy [9], and Optically Detected Magnetic Resonance [10]. Other “traditional” tools (e.g. ENDOR) have continued to be applied with great success.

It is intriguing to compare silicon with diamond, the group IV cubic semiconductor of smallest atomic number. In only a few experiments have isotope data been used to probe optical centres in diamond [12, 13]. However, most natural diamonds contain primarily only one impurity, nitrogen (see, e.g., ref. [141]) because the lattice has a small interatomic spacing and exceptionally high resistance to deformation. In addition to being a clean system, the large energy gap (5.49 eV [15]) facilitates optical measurements on diamond, and the high Debye temperature ( $\sim 2000$  K) allows “low temperature” measurements to be carried out mainly at only 77 K. Impurity-related absorption and luminescence in diamond was recognised in the nineteenth century [16], vibronic processes were discussed in 1941 [17], and systematic radiation damage studies began in the 1950s [18]. The symmetry of all the common optical centres are known (e.g. ref. [19]), their extensive Jahn–Teller and pseudo-Jahn–Teller effects are largely understood [20] and their radiative decay times known [21].

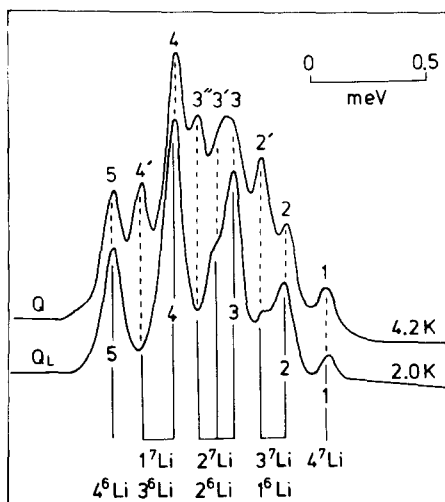


Fig. 2. Photoluminescence of the 1044 “QL” and “Q” 1045 meV lines (section 5.5), measured in silicon doped with approximately equal concentrations of  ${}^6\text{Li}$  and  ${}^7\text{Li}$  [11], establishing that the centre contains 4 Li atoms. The composition of the centre producing each line is shown at the bottom.

## 2. Relevant properties of pure silicon

Silicon, with atomic number 14, has natural isotopes in the abundance ratios

$$^{28}\text{Si} : ^{29}\text{Si} : ^{30}\text{Si} = 0.922 : 0.047 : 0.031 . \quad (1)$$

### 2.1. Phonon-related properties

Silicon crystallises in the diamond type of face-centred lattice, with two Si atoms at each lattice site. The interatomic spacing at room temperature is 0.234 nm [22], corresponding to a lattice parameter of 0.543 nm, a density of  $2330 \text{ kg m}^{-3}$  and  $5.0 \times 10^{22} \text{ cm}^{-3}$  atoms. With increasing temperature the lattice parameter is constant (on the scale of interest here) from 0 to 20 K, and then *decreases*, reaching a minimum at  $T \sim 120$  K (fig. 3 [23]). Many optical transitions are perturbed to higher energy by a lattice contraction. The negative thermal expansion tends to *increase* the energy of those optical lines as the temperature increases, the opposite of what is usually observed in crystals, in the important range  $0 < T < 100$  K (section 7.5).

For a crystal with a cubic lattice, like silicon, three elastic constants are required in linear elastic theory to relate the stress tensor components  $s_{ij}$  to the strain tensor components  $e_{ij}$  in the form

$$s_{xx} = c_{11}e_{xx} + c_{12}e_{yy} + c_{12}e_{zz}, \quad s_{xy} = c_{44}e_{xy},$$

with similar equations given by permutations of the subscripts  $x, y, z$ . In the limit of low temperature [24]

$$c_{11} = 168 \text{ GPa}, \quad c_{12} = 65 \text{ GPa}, \quad c_{44} = 80 \text{ GPa}. \quad (2)$$

Consequently Poisson's ratio  $\sigma$  (the ratio of the strains perpendicular and parallel to an applied unidirectional stress) differs with the direction of the stress. For  $\langle 001 \rangle$  stresses

$$\sigma = c_{12}/(c_{11} + c_{12}) = 0.28, \quad (3)$$

and generally a working value of about 0.25 can be used.

The phonon dispersion curves are shown in fig. 4 for the major symmetry directions [25], measured at 300 K. The few data available at lower temperatures ( $T = 80$  K [27]) show phonon energies  $\sim 1\%$  larger, but this is of the order of the experimental uncertainties. Photoluminescence data allow some

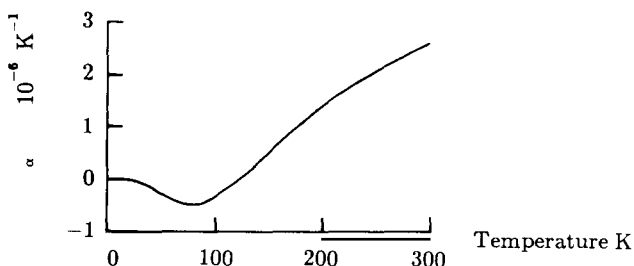


Fig. 3. Line of data for the coefficient of linear expansion [23].

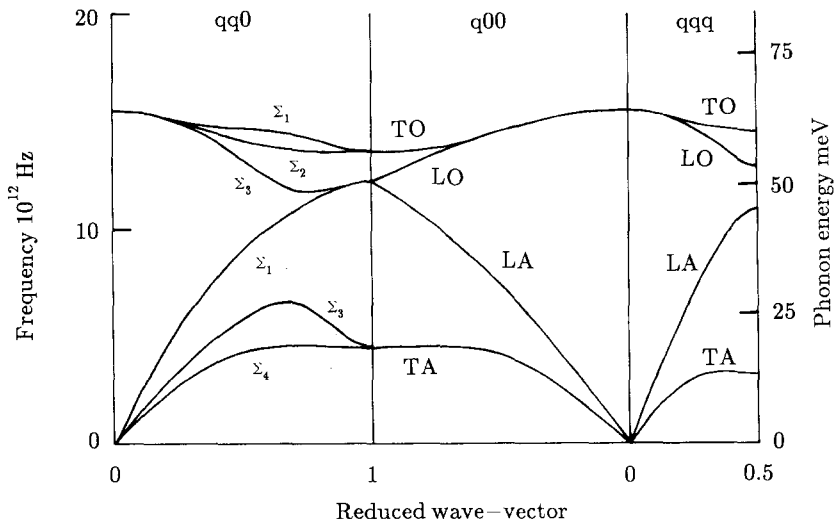


Fig. 4. Phonon dispersion curves at 300 K for propagation on  $\langle 001 \rangle$ ,  $\langle 111 \rangle$ ,  $\langle 110 \rangle$  axes calculated using a five-neighbour Born-von Karman model [25].

critical points to be measured at 2 K (fig. 45). There is general agreement about the shape of the one-phonon density of states function (fig. 5 [28]), but different calculations show variations of up to 5% in the energies at which the critical points occur. An extensive tabulation of phonon calculations is given by Torres and Stoneham [29]. The dispersion curves, and hence the density of state curve, scale closely to those of germanium [26]. However, compared to diamond, the ratio of the frequencies at the critical points of the transverse modes to the frequency of the Raman mode is small. Qualitatively, compared with diamond, silicon and germanium are easier to shear, and so we can anticipate that optical centres in these crystals will be more prone to spontaneous deformations than the corresponding defects in diamond. The Raman phonon energy in the limit of low temperature is [30]

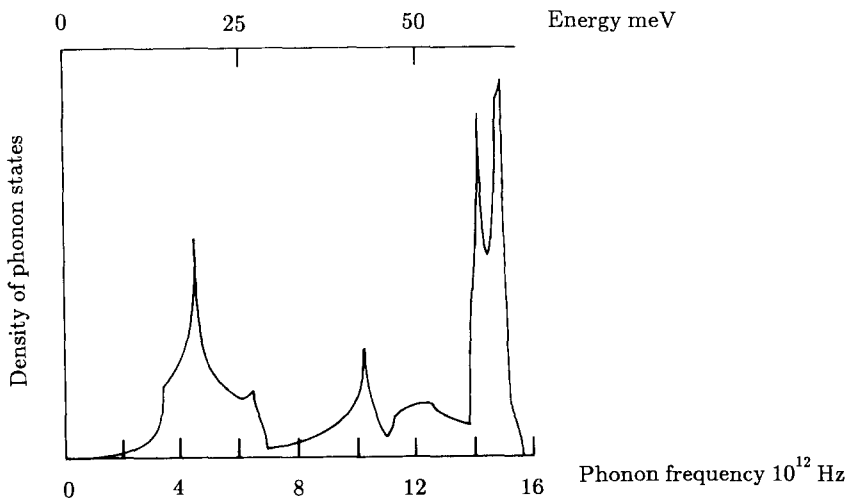


Fig. 5. Density of phonon states at 300 K, calculated using a six-neighbour Born-von Karman model [28].

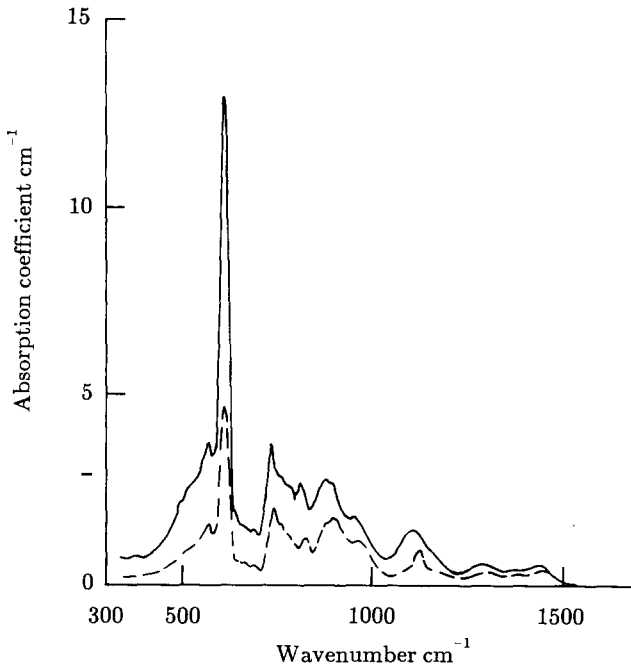


Fig. 6. Two-phonon intrinsic lattice absorption measured at 20 (dashed line) and 365 K (solid line) [32].

$$\hbar\omega = 524 \text{ cm}^{-1}, \quad (4)$$

decreasing to  $510 \text{ cm}^{-1}$  at 750 K. Two-phonon Raman scattering data are given in ref. [31].

Absorption of photons with the creation of one phonon is forbidden in perfect silicon, but photons may be absorbed in transitions involving two or more phonons (fig. 6 [32, 33]). For two-phonon processes involving phonons of frequencies  $\omega_1$  and  $\omega_2$  the intensity of the absorption increases with temperature as  $[1 + n(\omega_1)][1 + n(\omega_2)]$ , where the phonon population terms are

$$n(\omega) = 1 / [\exp(\hbar\omega/kT) - 1]. \quad (5)$$

Some impurities produce local mode absorption, which is then superimposed on this underlying two-phonon absorption. For example, the local mode of substitutional carbon is close to the strong intrinsic absorption at  $610 \text{ cm}^{-1}$ , limiting the sensitivity of detecting the mode (section 4.1.1).

Usually photoluminescence is generated in silicon by illuminating it with a laser beam running at power densities of up to  $\sim 100 \text{ mW mm}^{-2}$ , and the temperature of the silicon may be significantly increased (section 3.1.2). The thermal conductivity  $K$  increases to a maximum near 30 K (fig. 7 [34]). At temperatures of interest in optical measurements ( $T < 10 \text{ K}$ ),  $K$  is proportional to  $T^3$ . Heat deposited by a localised excitation such as a laser beam cannot diffuse easily. Because the specific heat is also proportional to  $T^3$  (fig. 8 [35]), this “trapped” energy can produce a very large fractional change in temperature (section 3.1.2).

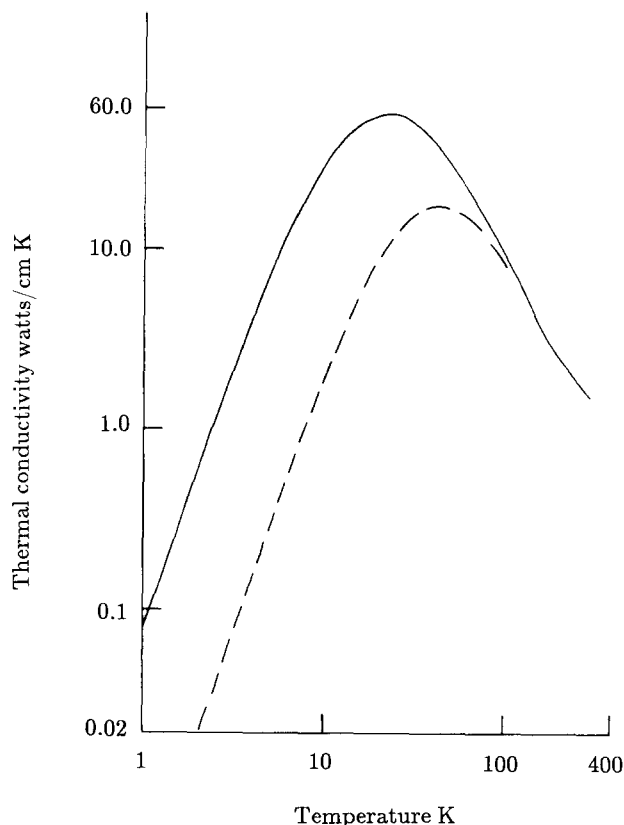


Fig. 7. Dependence of thermal conductivity on temperature for samples of similar cross sections (approximately  $6 \times 6 \text{ mm}^2$ ), but with low impurity concentrations,  $[B] = 1 \times 10^{13} \text{ cm}^{-3}$ ,  $[P] = 3.7 \times 10^{15} \text{ cm}^{-3}$  (solid line), and higher impurity concentrations,  $[B] = 4 \times 10^{16} \text{ cm}^{-3}$  and  $[P] < 10^{15} \text{ cm}^{-3}$  (broken line). Thermal conductivity at 3 K varies by a factor of over 60 between these samples, decreasing in proportion to  $[B]$  when  $[B] > 10^{15} \text{ cm}^{-3}$  [34].

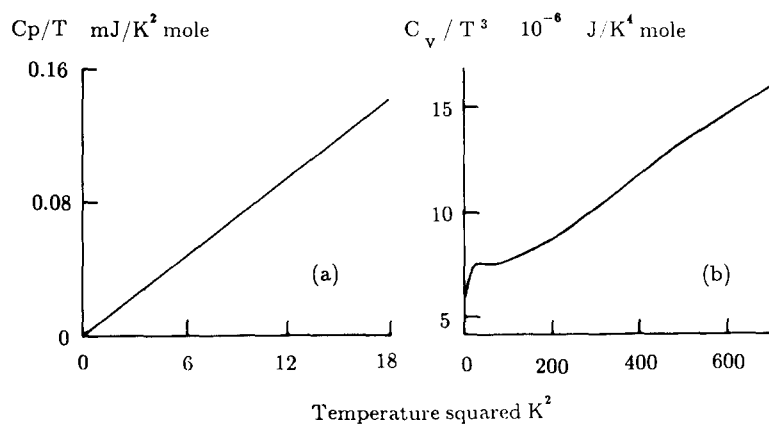


Fig. 8. Specific heat of pure silicon for  $T < 4.2 \text{ K}$  and  $T < 27 \text{ K}$  [35, 36].

## 2.2. Electron-related properties

The fundamental energy gap between the valence and conduction bands is indirect, decreasing monotonically from 1.170 eV at 0 K to  $\sim$ 1.125 eV at room temperature (fig. 9 [37]). This indirect gap is located at

$$k_m \sim 0.80 \pm 0.05 \quad (6)$$

of the zone boundary lattice vector along the 001 axes from  $k = 0$  [38]. These parameters were determined using optical absorption measurements, as described below, and so depend on knowing the values of the exciton binding energy and the phonon dispersion curves. The energy gap therefore has an uncertainty of  $\sim$ 1 meV. Eaves et al. [39] have located  $k_m = 0.85 \pm 0.01$  of the  $\langle 001 \rangle$  zone boundary, based on the energy of the intervalley scattering phonon and the dispersion curves. At the minimum energy point the conduction band has elliptical energy contours with electron effective masses (in terms of the free electron mass  $m_0$ )

$$m_\ell = 0.9163m_0, \quad m_t = 0.1905m_0, \quad (7)$$

along and perpendicular to the unique  $\langle 001 \rangle$  axis at that point [40]. The g-factor of the electrons at these conduction band minima is isotropic [41],

$$g_e = 1.99893. \quad (8)$$

The valence band maximum at  $k = 0$  contains the atomic 3p orbitals, and in the absence of spin-orbit interaction would be six-fold degenerate. Spin-orbit interaction splits the  $j = 1/2$  states to lower (electron) energy by [42]

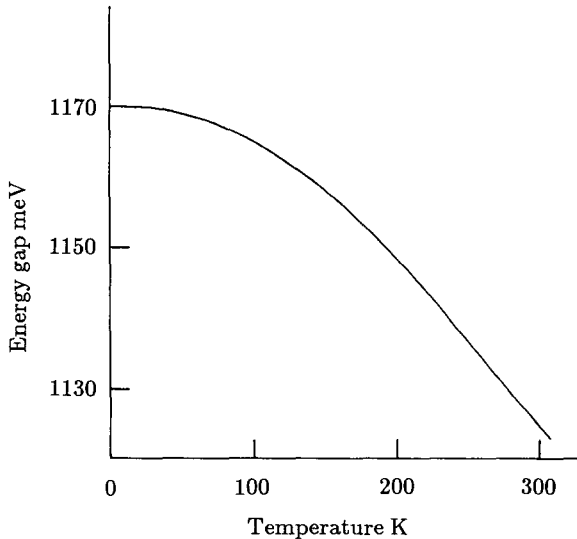


Fig. 9. Temperature dependence of the intrinsic energy gap [37].

$$\Delta = 44 \text{ meV} \quad (9)$$

relative to the  $j = 3/2$  states. In the limit of low temperature the  $j = 3/2$  states have heavy and light hole masses [43],

$$m_h = 0.537m_0, \quad m_\ell = 0.153m_0, \quad (10)$$

and the  $j = 1/2$  states have [44]

$$m_{\text{so}} = 0.29m_0. \quad (11)$$

The band structure is given in fig. 10 [45].

For photons with energies substantially greater than the band gap energy, absorption occurs by electron excitation at constant wavevector. The absorption is strong (fig. 11 [46]). When photoluminescence is excited by visible radiation, for example at photon energies of  $h\nu \sim 1.84 \text{ eV}$  (for krypton lasers) or  $2.5 \text{ eV}$  (for argon lasers), the penetration depths  $d$  at the  $1/e$  intensity level are (from fig. 11)

$$d \sim 5 \mu\text{m} \text{ at } 1.84 \text{ eV} \text{ to } 1 \mu\text{m} \text{ at } 2.5 \text{ eV}. \quad (12)$$

It is these surface layers which predominate in the luminescence from a bulk crystal excited by visible light if there is a sufficient concentration of exciton traps that there is little migration of the excitons. Visible light is also strongly reflected from silicon. At normal incidence the reflection coefficient  $R$  is [47]

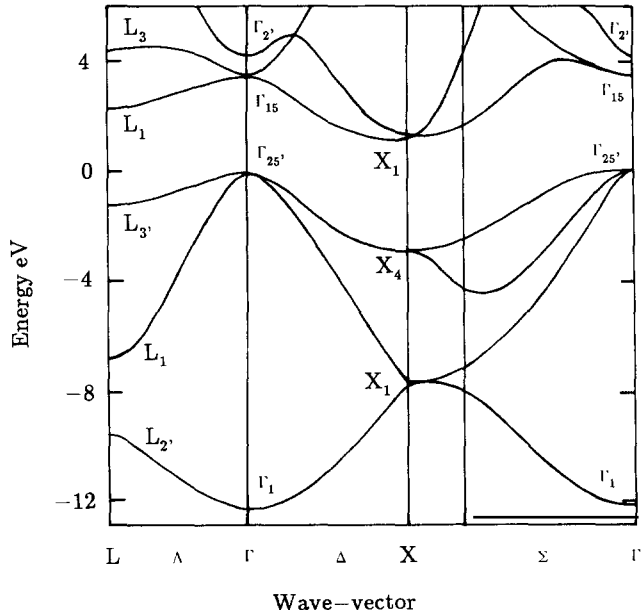


Fig. 10. Electron dispersion curves calculated by the non-local pseudopotential method [45].

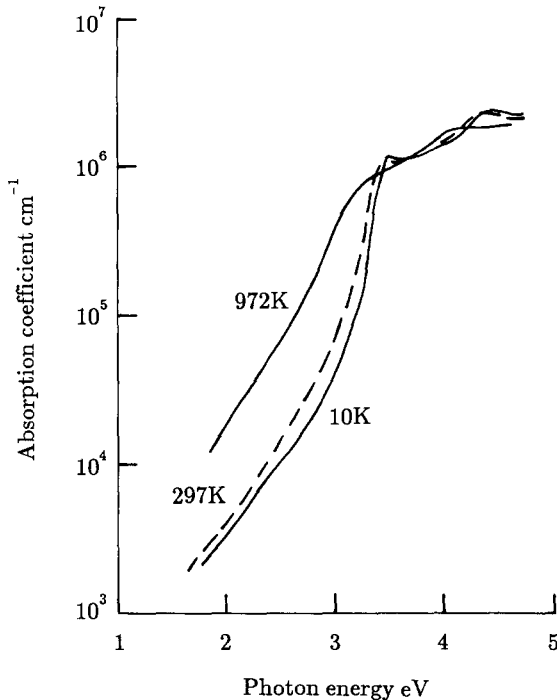


Fig. 11. Absorption coefficient (on log scale) for visible photons, measured at 10, 297 and 972 K [46].

$$R \sim 0.35 \text{ at } 1.84 \text{ eV to } 0.4 \text{ at } 2.5 \text{ eV}, \quad (13)$$

and  $R \sim 0.3$  for photons of energy less than the gap.

At photon energies close to the energy gap, excitation of an electron from the upper valence band with  $k = 0$  to the conduction band minima at  $k_m$  (eq. 6) requires a phonon of wavevector  $-k_m$  to be created or one of  $k_m$  absorbed to conserve wavevector in the transition. In addition to the free particle transitions (valence band to conduction band), Wannier excitons may be created, involving the same phonons (since the electron and hole states are essentially the same). Accurate measurements of the properties of the absorption edge have been made using the thresholds at which absorption occurs with exciton creation, the spectral appearance of the thresholds being sharpened by wavelength modulation [37]. Since the Wannier exciton is a hydrogen-like system, the binding energy  $E_x$  in its ground 1s state can be calculated from the energy spacings of the Rydberg series of states [48, 49],

$$E = 14.3 \pm 0.5 \text{ meV}. \quad (14)$$

In practice only the energy difference between the 1s and 2s states (10.7 meV) have been used. These already differ in absorption strength in the ratio  $I_1/I_2 = 7$ , and transitions to higher excited states will be weaker. Direct optical transitions from the 1s to the 2p states have been detected by far infra-red absorption with the exciton population being maintained by pumping with visible radiation [50]. The 2p states lie 10.2, 11.4 and 12.0 meV above the 1s state.

The energy of the  $k_m$  phonon was obtained initially by comparing the absorption and emission of phonons at high temperature [51]. Current values are [48, 52]

$$\begin{aligned}
 \hbar\omega &= 18.4 \pm 0.2 \text{ meV}, & \text{TA mode}, \\
 &= 56.2 \pm 1 \text{ meV}, & \text{LO mode}, \\
 &= 58.0 \pm 1 \text{ meV}, & \text{TO mode}.
 \end{aligned} \tag{15}$$

Knowing  $E_x$  and the phonon energies, the temperature dependence of the energy gap could be measured, using the threshold of exciton absorption, enhanced by wavelength modulation [37]. Note how the derivation of  $E_x$ ,  $\hbar\omega$  and  $k_m$  are all strongly interconnected.

In photoluminescence at low temperature ( $T < 30$  K), photons are emitted when the free exciton self-annihilates, and phonons of  $k_m$  are emitted. In addition a weak zero-phonon component has been reported (fig. 12 [53]), made allowed by small deviations from a non-cubic environment. Assuming that the energy of the zero-phonon component is not changed by the environment, this spectrum gives a check that the values of eqs. (14) and (15) are essentially correct. To lower energy, near 1.03 eV, weak luminescence can also be seen on fig. 12, involving the emission of two phonons. Since the total wavevector must add to  $k_m$ , these processes are clearest when they involve one  $k \sim 0$  optic mode ( $\Gamma$  on fig. 12). A full tabulation is given by Vouk and Lightowers [52].

The relative ratios of the phonon-assisted peaks are temperature dependent. At temperatures  $T \gtrsim 15$  K the relative intensities are [52, 54]

$$\text{TA : LO : TO} = 0.03 : 0.1 : 1, \tag{16}$$

in agreement with the ratios measured in absorption [49]. At lower temperatures the LO peak increases in relative strength, becoming 0.33 of the TO peak in the limit of low temperature [53]. The

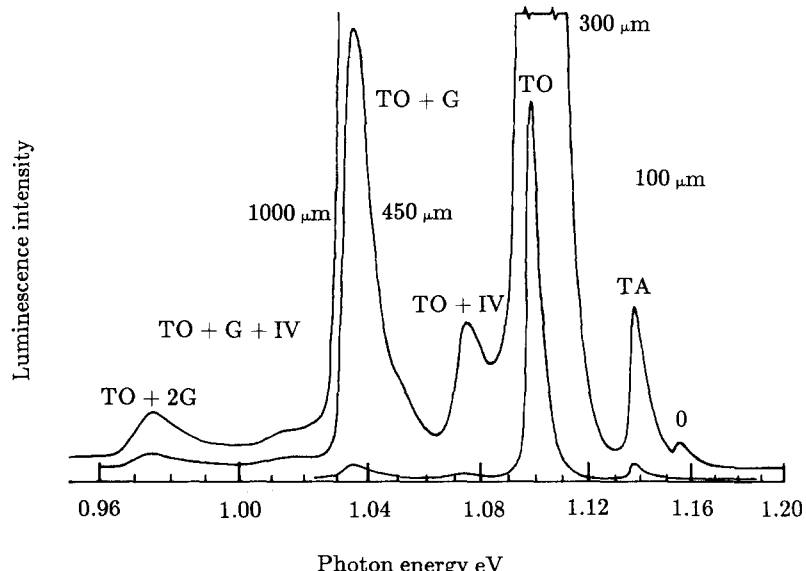


Fig. 12. Intrinsic photoluminescence of silicon at 26 K recorded with four different slit widths (100 to 1000  $\mu\text{m}$ ) to give varying amplification. Labels refer to the phonon combinations involved [eq. (15), G is  $k = 0$  optic mode]. LO and TO components are not resolved (see fig. 15). Peak 0 is the ideally forbidden zero-phonon component [53].

temperature dependence is caused by a splitting of the ground state of the exciton. The ground state is formed from an electron in a conduction band minimum being located near a hole in one of the four-fold degenerate valence band maximum states. The mass anisotropy of the electron (eq. 7) produces a non-spherical negative charge distribution with respect to the hole, lifting the degeneracy of the hole states and splitting the ground state of the exciton by

$$\Delta = 0.29 \pm 0.05 \text{ meV}. \quad (17)$$

This small splitting has been measured by extrapolating to zero stress the perturbations of the two exciton states produced by uniaxial compressions [55]. At low enough temperature only the lower energy exciton state is appreciably populated and the selection rules for the indirect gap transition favour LO phonon participation [54].

The shapes of the free exciton photoluminescence bands are accurately described by

$$I(E) \sim (E - E_0)^{1/2} \exp[-(E - E_0)/kT], \quad (18)$$

where  $E_0$  is the threshold of luminescence [55]. The square root term arises from the density of exciton states of different kinetic energy  $(E - E_0)$ , and the Boltzmann factor gives the relative probability of occupying each of these states. The free exciton bands therefore have a full width  $W$  at half height [56]

$$W = 1.795kT, \quad (19)$$

with a characteristic linear dependence on temperature.

Because the free exciton consists of electron and hole states widely separated in  $\mathbf{k}$  space, their probability of recombination is low. During the lifetime of the free exciton there is therefore a significant probability of the exciton being trapped at crystal defects. The intrinsic radiative decay time  $T_{fe}$  of the exciton is therefore uncertain, but is at least the maximum reported value, which is 60  $\mu\text{s}$  [58]. The radiative decay time decreases rapidly with the increasing concentration of traps which can capture the exciton (e.g. to 2  $\mu\text{s}$  at a boron concentration of  $5 \times 10^{12} \text{ cm}^{-3}$  [57]). In ideally perfect silicon at temperatures sufficiently low that there is no thermal dissociation of the electron and hole [ $T \leq 15 \text{ K}$ , cf. eq. (8)] the free exciton density  $n_{fe}$  would presumably decay exponentially with time, with a decay time  $T_{fe}$ . In real silicon, traps capture the excitons at a rate proportional to the diffusion speed  $v$  of the exciton, to its capture cross section  $\sigma_i$  at the  $i$ th species of trap, and to the concentrations  $n_i$  of those traps. The equation for the free exciton concentration  $n_{fe}$  is

$$\frac{dn_{fe}}{dt} = -n_{fe}/T_{fe} - \sum_i n_i \sigma_i v n_{fe}, \quad (20)$$

at 0 K. When the traps are shallow donors and acceptors (e.g. boron or phosphorus atoms), the exciton is bound with a binding energy of only a few meV (3.8 meV for B, section 4.3). Consequently, as the temperature increases from 0 K there is a rapid increase in the probability of thermal ionisation of the excitons off the shallow centres, increasing the probability that they can undergo radiative decay (fig. 13 [58]). At higher temperatures the intensity of the free exciton emission decreases, probably as the excitons become thermally dissociated (fig. 14). Very similar effects are seen in the intensity of the luminescence from many defects in silicon (section 3.1.1).

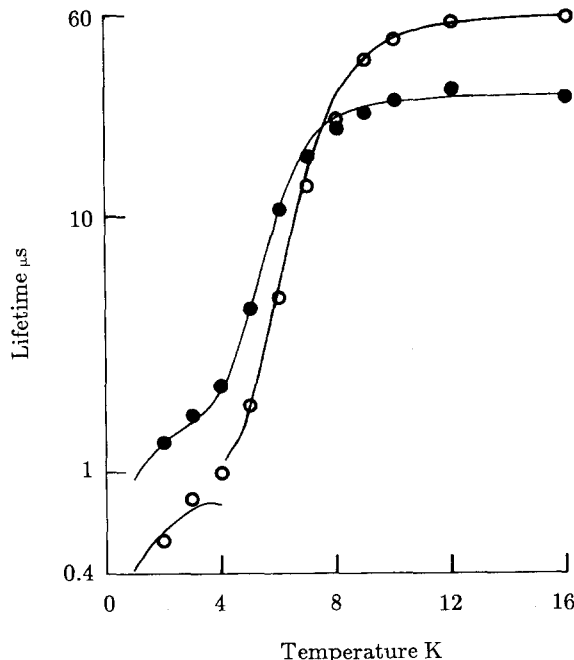


Fig. 13. Points show measured lifetimes of free exciton luminescence in two samples. One has  $[B] \sim 10^{12}$ ,  $[P] \sim 4 \times 10^{10} \text{ cm}^{-3}$  (filled circles), the other  $[P] \sim 2 \times 10^{12}$ ,  $[B] \sim 10^{12} \text{ cm}^{-3}$  (open circles) [276].

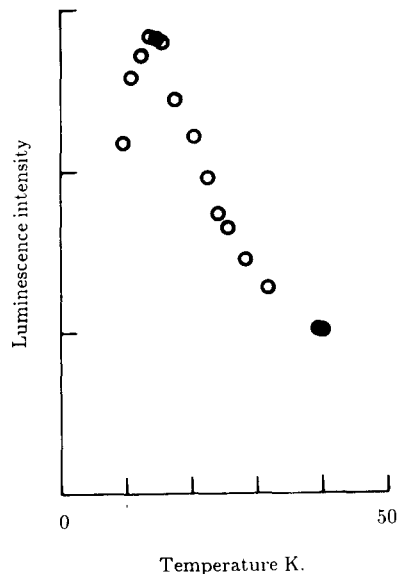


Fig. 14. Intensity of free exciton luminescence in high-purity ( $21 \text{ k}\Omega$ ) silicon in the higher temperature regime (cf. fig. 13). Data by E.C. Lightowlers (private communication 1987).

The diffusion coefficient  $D$  of the exciton is not known. Assuming it is similar to that of the free electron, Cuthbert [7] has derived a value  $D \sim 34 \text{ cm}^2/\text{s}$  at 20 K. The mean distance of diffusion in the maximum decay time of  $T_{fe} = 60 \mu\text{s}$  is therefore estimated to be

$$R = (DT_{fe})^{1/2} \sim 430 \mu\text{m}. \quad (21)$$

In impure silicon, capture at impurities will lower  $T_{fe}$  and  $R$  will be less. There are no published data for  $R$  in silicon; with  $10^{13} \text{ cm}^{-3}$  B atoms, M. Gregson (private communication) estimates that at 4.2 K,  $\sim 10\%$  of the excitons penetrate through a thickness of 150  $\mu\text{m}$ , decreasing by an order of magnitude for a factor of 10 higher concentration. In germanium, the diffusion coefficient for excitons has been measured at 3 K as  $D \sim 1500 \text{ cm}^2/\text{s}$  [59], giving (with  $T_{fe} = 8 \mu\text{s}$ ) also a diffusion length  $R \sim 400 \mu\text{m}$ . Since photo-excitation usually occurs only a few  $\mu\text{m}$  into the silicon (eq. 12), strains caused by a rough surface may attract the excitons into non-radiative trapping points, greatly reducing the luminescence efficiency. It is known that the efficiency of free exciton luminescence excited close to the surface is critically dependent on the quality of the surface finish.

With increasing excitation energy density, for example with  $\sim 3 \text{ W mm}^{-2}$  of visible light incident on the silicon, the electrons are unable to de-excite fast enough through exciton recombination. Electrons and holes begin to pile up in the conduction band minima and valence band maximum states [60]. In silicon the electron-hole densities in these "electron-hole droplets" are  $3 \times 10^{18} \text{ cm}^{-3}$  [61], considerably higher than in germanium.

As a result of this high density, the dominant electron-hole recombination process is non-radiative.

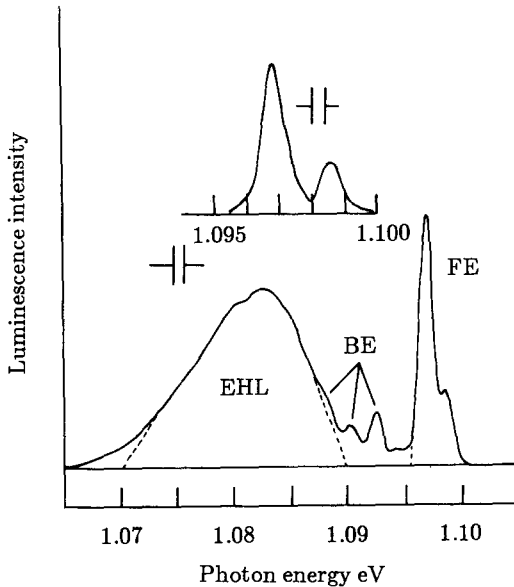


Fig. 15. TO- and LO-phonon-assisted luminescence from electron–hole droplets at 2.1 K. The binding energy of an electron and hole in the droplet relative to a free exciton is 5 meV, the energy difference between the low-energy cut-off of the free exciton peak and the high-energy cut-off of the electron–hole liquid. The free exciton structure is shown in detail in the inset [61].

One electron recombines with one hole, a phonon being emitted to conserve  $k$ , and with the remainder of the energy being used to excite an electron (or hole) into its band continuum in a (phonon-assisted) Auger process [62]. This fast process gives a decay time for the droplets in silicon of  $\sim 0.15 \mu\text{s}$  [7] compared with  $\sim 40 \mu\text{s}$  in Ge [63], and produces a low luminescence efficiency in silicon,  $\sim 5 \times 10^{-4}$  [7], compared with  $\sim 25\%$  in germanium. The weak recombination luminescence produces a broad band on the low energy side of the free exciton structure (fig. 15). In a photoluminescence experiment, observation of this rapidly decaying band indicates that other, slower, de-excitation processes for the excitons are saturated. The Auger process cited here as the dominant de-excitation mechanism results in one electron (or one hole) being excited deep ( $\sim E_g \sim 1 \text{ eV}$ ) into the conduction (or valence) band. The hot electron de-excites by optical and acoustic phonon emission at a rate [64]

$$\frac{dE}{dt} \sim 5 \times 10^{11} \text{ eV/s}, \quad (22)$$

when they have  $\sim 1 \text{ eV}$  excess energy above the conduction band minima; the holes are de-excited faster [64] and so can be ignored in the following. Before electron de-excitation occurs there is a small probability of the hot electron recombining with a thermalised hole (near the valence band's extremum) in the electron–hole droplet. The photon emission is weak ( $\sim 1$  photon per second in the experimental conditions [64]). The recorded spectrum (fig. 16) is structured with major peaks separated by the optic phonon energy ( $\sim 50 \text{ meV}$ ) and with weaker structure from the acoustic phonon de-excitation processes. At low temperature, luminescence is also detected near 2.27 eV from the simultaneous recombination of two electrons and two holes in the dense electron–hole droplets (fig. 17 [64, 65]).

At  $\sim 20 \text{ K}$  the droplets are “vaporised”, increasing the density of free excitons, and consequently increasing the bi-exciton luminescence at 2.31 eV and inducing reactions between pairs of electrons with pairs of holes in tri-excitons and quatra-excitons (X2 to X4 on fig. 17). The X2 line is symmetric in

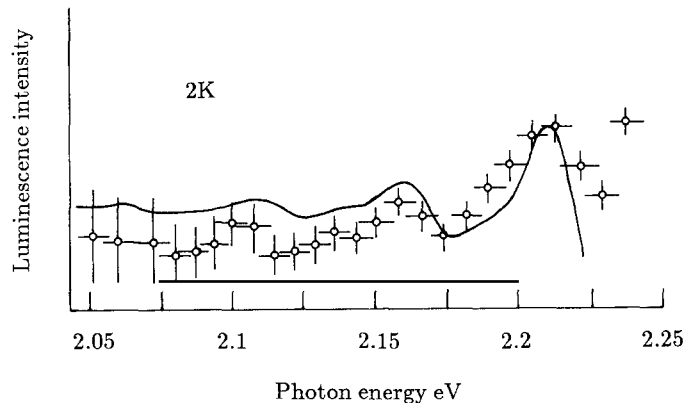


Fig. 16. Photoluminescence near twice the energy gap measured at 2 K [57].

contrast to the X3 and X4 lines. This is a consequence of the emitted photon having essentially zero momentum. For the X2 line two electrons annihilate two holes, leaving no free particles and so zero momentum. If the holes were in thermal equilibrium at the top of the valence band, the electrons must have come from opposite conduction band minima. The bi-excitons had zero translational momentum and so no spread in energy.

For the X3 line, the ground state consists of the one surviving exciton. If the initial state had translational motion, that momentum is given to the surviving exciton. However, because the final mass is one third of the tri-exciton's mass, the surviving exciton must have three times the speed and so three times the kinetic energy. A tri-exciton of kinetic energy  $K$  emits a photon of energy  $2K$  less than the photon of a tri-exciton at rest. The Maxwell-Boltzmann distribution of tri-exciton speeds produces an

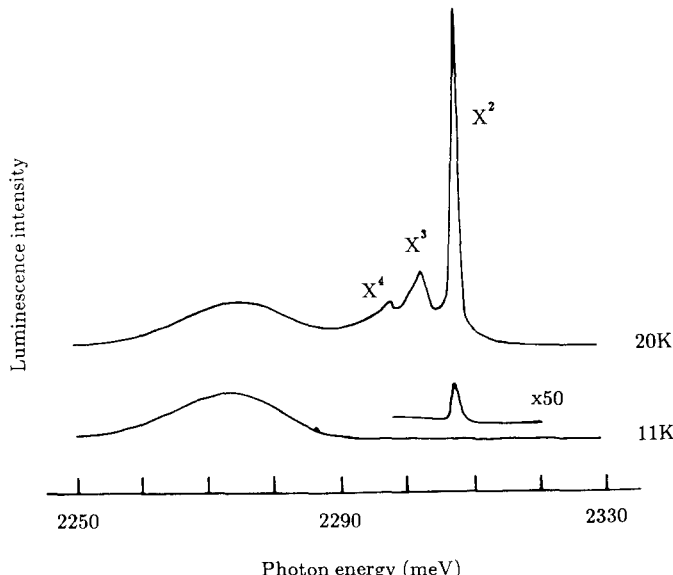


Fig. 17. Luminescence near twice the energy gap from recombination of two electrons and two holes in the droplets at 11 K, and at 20 K from bi-, tri-excitons etc. (peaks X<sub>2</sub>, X<sub>3</sub>, . . .). Note the asymmetric shape of X<sub>3</sub> and X<sub>4</sub> with the long tail to low energy, in contrast to free exciton luminescence (fig. 12) [65].

asymmetric X3 line, with the tail to lower energies (fig. 17) in contrast to the lineshape (eq. 18) of single excitons.

This is one example of the valuable data contained in lineshapes (see also section 10). Weak photoluminescence can also occur near twice the energy gap by recombination of a thermalized electron (or hole) with a hole (or electron) which is highly excited after an Auger kick-off from a trap [66].

We will later be concerned with the effects of strains on the band extrema. A compressive hydrostatic strain  $e$ , which maintains the symmetry of the crystal, reduces the indirect energy gap by [67]

$$\frac{dE}{de} = -1.8 \pm 0.2 \text{ eV}, \quad (23)$$

corresponding to a hydrostatic stress dependence

$$\frac{dE}{ds} = -15 \text{ meV/GPa}. \quad (24)$$

When a uniaxial compression is applied along the  $\langle 111 \rangle$  axes, the six conduction band minima (along the  $x$ ,  $y$ ,  $z$ ,  $-x$ ,  $-y$  and  $-z$  axes) are all equally perturbed, and so there is no lifting of their degeneracy. The other extreme situation is to apply a compression along one of the cube axes, say the  $z$  axis. The  $+z$  and  $-z$  oriented conduction band minima are lowered in energy relative to the  $x$ ,  $y$ ,  $-x$  and  $-y$  minima. The splitting is given by

$$\frac{dE}{ds} = 92.5 \text{ meV/GPa}. \quad (25)$$

Under a  $[110]$  uniaxial stress the  $[001]$  valleys lie at a higher energy than the  $[010]$  and  $[100]$  valleys. The splitting is by

$$\frac{dE}{ds} = 46.3 \text{ meV/GPa}, \quad (26)$$

to first order in the stress (valid for our purposes for  $s < 0.2 \text{ GPa}$ ). At higher stresses the  $[001]$  valley is repelled from higher lying conduction band states [67].

The valence band at  $k=0$  is split by all directions of uniaxial stresses. In photoluminescence we are often concerned only with the  $j=3/2$  (lowest energy hole) states. To first order in the stress (i.e. neglecting the stress-induced interaction of the  $j=3/2$  with the  $j=1/2$  states 44 meV away) the splitting amounts to [67]

$$\begin{aligned} \frac{dE}{ds} &= 45 \pm 2 \text{ meV GPa}^{-1}, \quad \text{for } [001] \text{ stress,} \\ \frac{dE}{ds} &= 35 \pm 2 \text{ meV GPa}^{-1}, \quad \text{for } [111] \text{ stress,} \\ \frac{dE}{ds} &= 48 \pm 2 \text{ meV GPa}^{-1}, \quad \text{for } [110] \text{ stress.} \end{aligned} \quad (27)$$

Note that because the valence band states are being split, the hole will always be able to lower its energy in a symmetry-lowering strain, and so the exciton is attracted into a strained area. This effect and the interactions of the  $j=3/2$  and  $1/2$  states are discussed in section 8.

One important feature of the effect of uniaxial stress on free excitons is that the perturbed states may

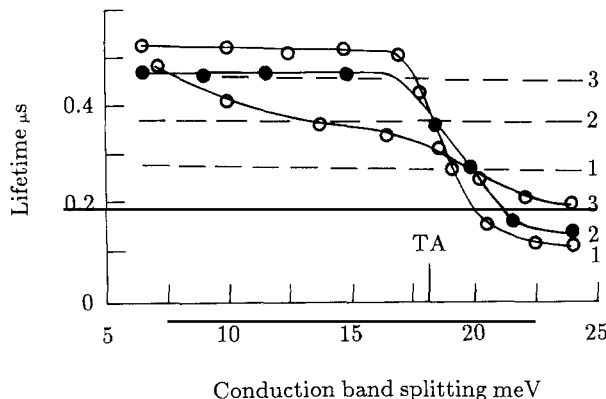


Fig. 18. Dependence of the radiative decay time of luminescence from “hot” (continuous lines) and “cold” (broken lines) excitons as functions of the stress-induced splitting between conduction band minima. Temperatures are 2, 4.2 and 15 K for curves 1, 2, 3, respectively [68]. The energy of the TA phonons connecting the conduction band minima is shown by “TA”.

not be in thermal equilibrium with each other. Under [001] stress at low temperature ( $T \leq 4$  K) electrons in the four [100] and [010] conduction band minima are unable to de-excite into the two [001] lower minima until the splitting exceeds  $\sim 16$  meV, when a  $k$  conserving phonon can be emitted (fig. 18 [68]). The phonons are transverse acoustic (fig. 4); scattering between neighbouring conduction band minima by TA phonons is forbidden in an ideally cubic lattice [69], but only a weak relaxation of the selection rule in the deformed crystal is necessary in view of the long ( $\mu\text{s}$ ) lifetime of the free exciton. Very similar non-thermalisation is observed in photoluminescence from some optical centres (section 8).

### 3. Methods of experimental study

#### 3.1. Photoluminescence

##### 3.1.1. Principles

Despite its importance in studying the optical properties of silicon, there has been little work on the mechanisms by which photoluminescence is generated. For example, there are few data on the dependence of the luminescence on the wavelength of the exciting light. Optical centres located within a few  $\mu\text{m}$  of the surface are preferentially excited by above-band-gap radiation (eq. 12), while centres distributed through the crystal may be more effectively excited by, e.g.,  $1.064 \mu\text{m}$  (1.165 eV) Nd-YAG radiation, to which silicon is almost transparent. Near-surface centres include those formed by the rapid quenching technique [70] since the surface cools more rapidly than the bulk. The dislocation luminescence lines D1 and D2 are preferentially excited by surface excitation (fig. 19) consistent with their being located within  $10 \mu\text{m}$  of the surface [71, 72]. There are also few data on the quantum efficiency of photoluminescence. Because silicon has an indirect energy gap, the radiative decay times of free excitons (and so of shallow bound excitons) are long (section 2.2), allowing non-radiative decay channels to lower the luminescence efficiency (section 4.3). To achieve a high quantum efficiency generally requires a deeper centre, such as the “ $1.32 \mu\text{m}$ ” band ascribed to sulphur doping with (external) quantum efficiencies up to 5% [73, 74].

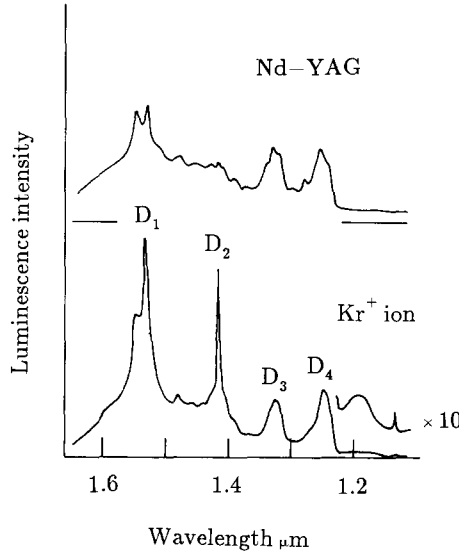


Fig. 19. Photoluminescence peaks D<sub>1</sub>-D<sub>4</sub> from dislocations excited by below-band-gap radiation (Nd-YAG at 1.165 eV) and above-band-gap (Kr<sup>+</sup> at 1.915 eV) [71]. Part of the lower spectrum has been enhanced by a factor of 10.

Usually photoluminescence is excited by a visible laser, operating at  $\sim 2$  eV, about double the energy gap. The highly excited electrons de-excite slower than the holes, by optic mode emission at the rate [75]

$$\frac{dE}{dt} = -\frac{m_t m_\ell^{1/2} D^2 \{(E - \hbar\omega)^{1/2} - (E + \hbar\omega)^{1/2} \exp(-x)\}}{2^{1/2} \pi \hbar^2 \rho [1 - \exp(-x)]}, \quad (28)$$

where  $m_t$ ,  $m_\ell$  are the transverse and longitudinal electron masses (eq. 10),  $D$  is the optical deformation potential constant,  $\hbar\omega$  is the optic mode quantum [ $\sim 58$  meV, eq. (15)], and  $x = \hbar\omega/kT$  is the reduced reciprocal temperature. Over the temperature range of interest ( $T < 100$  K),  $dE/dt$  is essentially independent of  $T$  at  $dE/dt = 3 \times 10^{11}$  eV/s when the excess energy is  $E \sim 1$  eV. As  $E$  reduces, energy loss by optic mode emission slows, and becomes zero at  $T = 0$  K when  $E = \hbar\omega$ . Acoustic phonon emission then dominates [75],

$$\frac{dE}{dt} = -\frac{2^{3/2} m_t^2 m_\ell^{1/2} \xi^2 E^{3/2}}{\pi \hbar^4 \rho}, \quad (29)$$

where

$$\xi^2 = \frac{2}{3} \xi_d^2 + \frac{m_\ell}{3m_t} (\xi_u + \xi_d)^2,$$

$\xi_u$ ,  $\xi_d$  are the acoustic deformation potentials and  $\rho$  is the density of silicon. At  $E \sim 1$  eV, acoustic emission gives  $dE/dt \sim 1.3 \times 10^{11}$  eV/s, decreasing as  $E^{3/2}$ . These times, verified by Betzler et al. [64], imply that for low excitation powers the electrons and holes thermalise on a negligible timescale compared with the microseconds typical of photoluminescence processes in silicon (section 2.2).

Recombination radiation is not observed at low temperature from free electrons and holes: the particles form excitons (at low excitation levels, when electron–hole droplets, section 2.2, can be ignored). Diffusion of the excitons allows them to be captured at photoluminescent centres. The free exciton recombination radiation is therefore a small fraction of the total, e.g.  $\sim 1\%$  at 4.2 K in silicon containing  $10^{15} \text{ cm}^{-3}$  B atoms [1], even though the B bound exciton emission has a low quantum efficiency.

The luminescence output from many deep optical centres has two temperature regimes. At higher temperatures,  $T \gtrsim 30 \text{ K}$ , the photoluminescence decreases rapidly (figs. 20, 22). In addition, at lower temperatures,  $0 < T < 25 \text{ K}$ , the luminescence intensity often increases with  $T$ , the increase being sample dependent.

We take first the decrease at higher temperatures. The dots on fig. 20a show data for the intensity of the 1018 meV zero-phonon line (section 5.4) as a function of temperature *measured in absorption*—these data establish that the transition probability for this line is only very weakly temperature dependent. (Other lines are also shown to have a weak temperature dependence in section 7.1.) In contrast the luminescence decreases rapidly at  $T > 30 \text{ K}$  (fig. 20). Two simple reasons can be put forward for the decrease: either a thermal equilibrium exists between excitons captured by the optical centre and free excitons, or the excitons cannot be captured by the centre (e.g., they are thermally dissociated before capture). Either way, if  $E$  is the relevant ionisation energy, the probability of luminescence will be

$$I(T) = I(0)/(1 + P), \quad P = gT^{3/2} \exp(-E/kT), \quad (30)$$

where  $gT^{3/2}$  is the effective density of band continuum states into which the ionisation occurs, assuming that the probability of capturing an exciton at the centre is independent of temperature. The line on fig. 20 shows  $I$  calculated with

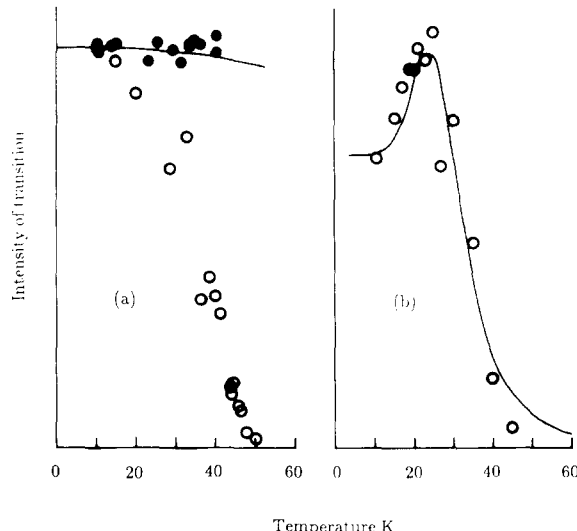


Fig. 20. Temperature dependence of zero-phonon lines of deep centres. (a) Filled circles show absorption in the 1018 meV line (section 5.4), open circles luminescence. The line is eq. (105). (b) Open circles show 1018 meV luminescence from a sample different from that in (a), with a moderate growth at  $T < 20 \text{ K}$ . The line is eq. (32).

$$E = 14.7 \text{ meV}. \quad (31)$$

This is very close to the ionisation energy of the free exciton (eq. 14), which would be consistent with thermal dissociation of the exciton limiting the luminescence output of this centre. At other centres the decrease in luminescence intensity occurs at the same temperature as a rapid decrease in the measured radiative decay time (e.g. fig. 21), indicating unambiguously that excitons captured by the centre have a shorter lifetime at higher temperature.

Below 25 K the luminescence from different samples has a different temperature dependence (figs. 20a,b), confirming that the growth in luminescence is sample dependent. Possibly the growth occurs as a result of competition for capturing the excitons between the optical centres and other (shallow) traps. With increasing temperature the excitons freed from the traps become available for capture by other, deeper, exciton traps, including photoluminescence centres. Consequently a rise in photoluminescence is frequently seen, especially up to  $\sim 25$  K (fig. 22). This is similar to the increase in free exciton luminescence in fig. 13. If the binding energy of the exciton at a trap is  $E$ , and we assume that all species of traps in a particular sample can be parametrised by traps of one effective  $E_t$ , then a fraction fraction

$$f = 1/[1 + bT^{3/2} \exp(-E_t/kT)]$$

of the traps are not ionised and can compete with the luminescence centres for the capture of excitons. The luminescence intensity at  $T$  is then

$$I(T) = I(0)/[(1 + f')(1 + P)], \quad (32)$$

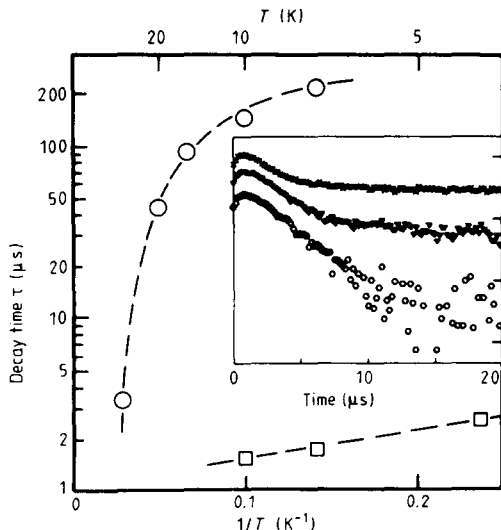


Fig. 21. Main plot shows measured radiative decay time of the 789 meV band (section 5.1). Inset shows decay curves of the intensity as a function of time after excitation at temperatures of (from top to bottom) 10, 7, 4.2 K. At  $T < 10$  K an initial fast decay is observed, with decay time as shown by the squares on the main figure [177].

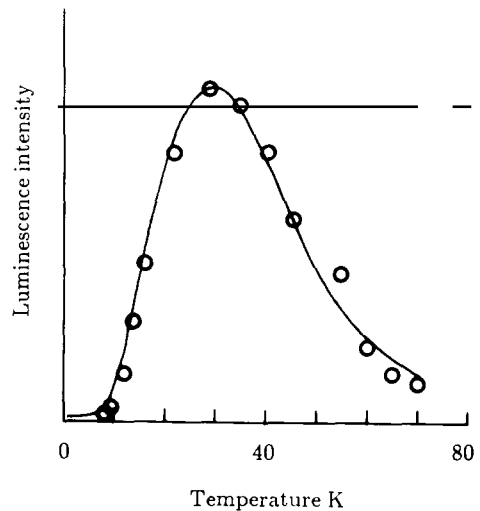


Fig. 22. Temperature dependence of the 767 meV "P" zero-phonon line generated in Czochralski (oxygen-rich) silicon after 48 hours at 450°C, and excited by above-band-gap photons, showing a strong increase in intensity at  $T < 30$  K. The line is eq. (32) with  $E_t = 3$  meV.

where  $f' = cf$  and includes the temperature independent ratio of the trapping cross sections for excitons at the luminescence centres and the competing traps. This expression fits the data on figs. 20b and 22 when  $E_t \sim 5$  to 10 meV and  $E = 14.7$  meV again. In particular, fig. 22 shows data for the 767 meV line (section 5), produced by thermal annealing for 48 hours at 450°C. This treatment also produces thermal donors (section 4.2), which could act as competing traps for excitons. The fit on fig. 22 has  $E_t = 3$  meV, a plausible value for exciton binding to shallow donors (section 4.3).

This growth mechanism amounts to a thermally induced transfer of energy from the shallow traps to the deeper photoluminescence centres. A similar process has been reported by Weman et al. [76], in which shallow bound exciton luminescence (section 4.3) is quenched by impact ionisation of electrons and/or holes from the bound exciton complexes. The effect requires accelerating fields of  $\sim 50$  V/cm for donor concentrations of  $\sim 4 \times 10^{14}$  cm $^{-3}$ , increasing with donor concentration as the mean free path decreases (fig. 23). At the same field strengths, a growth in intensity of deep level luminescence occurs (e.g. from the 903 meV line [77]) as the energy removed from the shallow centres is deposited on the deeper levels. At higher fields impact ionisation of the deep centres themselves decreases their luminescence intensity.

Some photoluminescence transitions decay at significantly higher temperatures, at  $T \geq 40$  K, even when there is no growth at low temperature. Examples are the 935 meV line [78], the 969 meV line (section 5) and the Be-related isoelectronic centre (section 8).

An important conclusion is that it is often much easier to detect the luminescence from a centre near 25 K than at lower temperatures. Comparison of the defects in different samples of silicon by comparing their luminescence spectra measured at liquid helium temperature may be misleading. If the traps competing for exciton capture below 20 K can be neutralized, for example by hydrogen, then a large increase in photoluminescence would be expected.

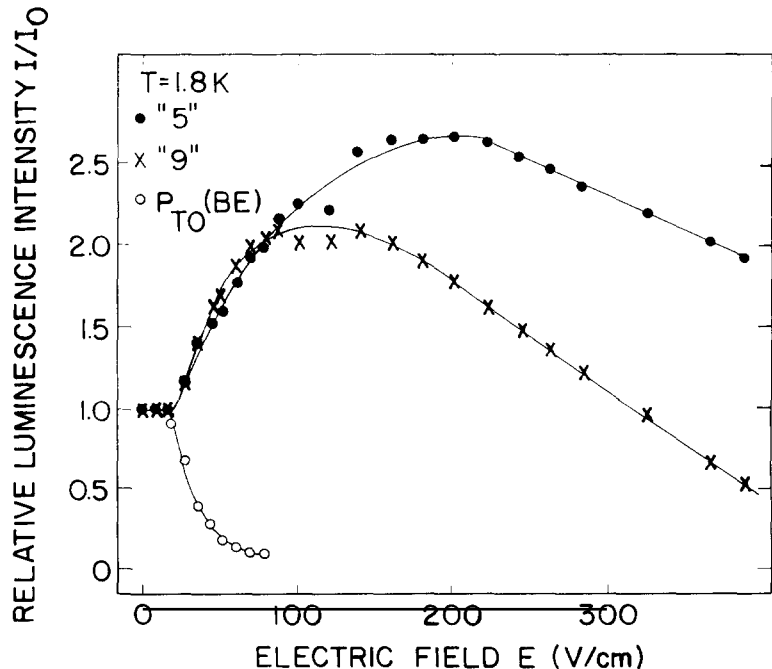


Fig. 23. Intensities of photoluminescence as functions of the electric field for excitons bound to phosphorus, the 903 meV line (9), and a line at 1119 meV (5) [77].

### 3.1.2. Practice

The data of section 2 are directly relevant to the way silicon crystals are mounted for luminescence measurements. Photoluminescence can be detected at 90° to the direction of excitation, so as to reduce the amount of exciting light scattered into the spectrometer. However a "135°" geometry gives a better efficiency when the exciting light is absorbed very close to the surface of the silicon (eq. 12). The luminescence originates in essentially a surface layer and is refracted on exiting the crystal as shown in fig. 24, giving a maximum light output at approximately 45° to the excitation axis. For further improvement in light output, but at a cost in convenience, the silicon can be machined into a Weierstrass sphere [79].

It is important to know the temperature of that part of the silicon which is producing the luminescence. Significant heating of the excited part of the crystal occurs readily, especially at low temperatures when both the thermal conductivity and the thermal capacity are small (figs. 7, 8). If the sample is immersed in a cryogenic liquid, minimal heating occurs for excitation power less than  $\sim 250 \text{ mW/mm}^2$ . Samples immersed in liquid hydrogen at  $\sim 20 \text{ K}$  (near the peak thermal conductivity, fig. 7) are heated by less than 0.5 K with excitation powers of  $1.5 \text{ W/mm}^2$  (E.C. Lightowlers, private communication 1987). However, many measurements (e.g. temperature dependence studies) require a less intimate contact between the cryogenic liquid and the sample. For illustration, consider a slice of silicon, thickness  $l$ , mounted in a vacuum on a metal heat sink maintained rigorously at temperature  $T_0$ . Suppose the front face of the crystal is excited uniformly over its area  $A$  so that after reflection losses (eq. 13) the power absorbed is  $dQ/dt$ . The only exit route for this heat is through the sample to the heat sink. In the steady state the heat flow  $dQ/dt$  at any depth  $x$  is  $dQ/dt = KA dT/dx$ . At sufficiently low  $T$  ( $T < 10 \text{ K}$ ),  $K = aT^3$ , where  $a = 0.08 \text{ W/cm K}$  for pure silicon (fig. 7). Integrating through the thickness of the sample shows that the excited face has a temperature  $T_e$  where

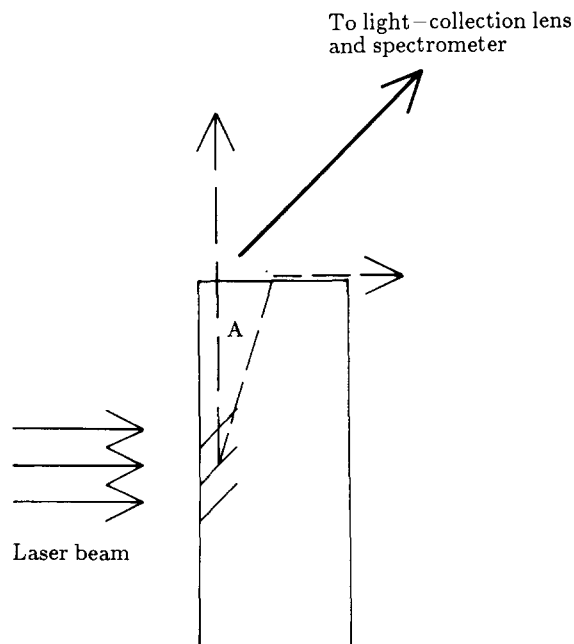


Fig. 24. Refraction of the luminescence originating (in the hatched area) near the surface of a cuboid of silicon is efficiently collected with "135° geometry"; total internal reflection occurs for  $A > 17^\circ$ .

$$T_e^4 - T_0^4 = (4l/aA)(dQ/dt) .$$

For a sample of 2 mm thickness excited uniformly with the moderate power of  $(dQ/dt)/A = 100 \text{ mW/mm}^2$ , and with a base temperature  $T_0 = 2 \text{ K}$ ,  $T_e = 3.3 \text{ K}$ . Impurities or radiation damage in the crystal may lower  $K$  by an order of magnitude (fig. 7), when  $T_e = 5.5 \text{ K}$ . In addition, phonon scattering at the interface between the Si and the heat sink will increase  $T_e$ . The large fractional increase in temperature can be critical when measuring temperature dependent properties, for example, the thermalisation between two states separated by  $\sim 1 \text{ meV} = 11.6 \text{ K}$  (section 8).

To overcome “beam heating” the temperature of the luminescing part of the crystal can be measured from the known temperature dependence of other spectral features. For example the common radiation-induced lines at 789 and 795 meV (section 5) have an intensity ratio determined by the Boltzmann ratio in the two excited states, which are split by 5 meV. The ratio can be used as a thermometer near 40 K. Similarly the Al acceptor bound exciton zero-phonon multiplet at 1150 meV (section 4.3) can be used near 10 K. Alternatively the measurements can be taken as a function of excitation power with a constant base temperature  $T_0$ . The correct value is then the limit of the measured values extrapolated to zero excitation power. Temperature dependent studies are trivial in principle but require a lot of care in practice.

The situation is worse when pulsed excitation is used. The time dependent equation to be solved for the same one-dimensional geometry is

$$dT/dt = (K/pC) d^2T/dx^2 ,$$

where  $p$  is the density ( $2330 \text{ kg m}^{-3}$ ) and  $C$  the specific heat. Both  $K$  and  $C$  are proportional to  $T^3$  at low temperatures (figs. 7 and 8, with  $C/T^3 = 2.8 \times 10^{-4} \text{ J/K}^4 \text{ kg}$ ). Following an instantaneous pulse the temperature decays exponentially with a decay time of

$$\tau = 4l^2 Cp / K\pi^2 = 0.2 \mu\text{s} \quad \text{as } T \rightarrow 0 . \quad (33)$$

If laser power is delivered in pulses which are short compared with this decay time, the energy of each pulse is bottle-necked in the excited region of the crystal. We have to be very careful how data taken under these circumstances are interpreted.

The small width of zero-phonon lines in silicon ( $\sim 0.1 \text{ meV}$  as  $T \rightarrow 0 \text{ K}$ ) results in very large peak absorption coefficients being obtained even for relatively weak integrated absorptions. This can have a pronounced effect on the luminescence intensity, especially if the luminescence travels through a long length (i.e. a few mm) of crystal. Self-absorption can produce an apparent doublet effect in a zero-phonon line when the transmission at the peak [which varies exponentially with absorbance, as  $\exp(-\mu t)$ ] dominates the luminescence (which is proportional to the transition probability, and hence proportional to  $\mu$ ). However, severe reduction of the integrated intensity may occur before the effects on the lineshape become obvious.

The competition between defects for excitation (section 3.1.1), and the experimental problems listed in this section, imply that the total amount of luminescence in a zero-phonon line is not necessarily proportional to the concentration of optical centres.

### 3.2. Absorption measurements and decay times

Very low concentrations of optical centres (e.g.,  $< 10^{13} \text{ cm}^{-3}$  [1]) can be detected using photo-

luminescence, but it is not generally a quantitative technique (section 3.1). The main scientific limitation of photoluminescence is that many optical centres in silicon have multiple excited states, which are not populated at low temperature. In contrast, the strength of absorption in an optical transition is always proportional to the concentration of optical centres capable of producing that absorption, and there is no thermal distribution factor working against detecting absorption into excited states. However, optical centres in silicon usually give weak absorption for two reasons:

(a) The concentration of the optical centres is usually low ( $<10^{16} \text{ cm}^{-3}$ ). Many centres are formed from carbon, which is typically present at  $\leq 10^{17} \text{ cm}^{-3}$ , of which only a quarter may be convertible to desired optical centres (section 6.3).

(b) Transition probabilities in silicon are frequently low because the transitions involve perturbed valence band and conduction band states (section 8), and transitions across the indirect gap have a low probability (section 2.2).

All known photoluminescence in silicon is caused by electric dipole transitions. The corresponding absorption coefficient  $\mu(E)$  at photon energy  $E$ , integrated over the entire absorption band, is related to the radiative decay time  $\tau$  of the luminescence band and the concentration [C] of the optical centres by the detailed balance relation (in SI units)

$$\int dE \mu(E) \sim \frac{\pi^2 h^3 c^2 (n^2 + 2)^2 g_i [C]}{9e^2 \tau n^2 g_f}, \quad (34)$$

where  $e$  is the mean energy of the emitted luminescence,  $n$  ( $\sim 3.5$ ) is the refractive index,  $c$  is the speed of light, and  $g_f/g_i$  is the ratio of the electronic degeneracies in the ground and excited electronic states of the centre. The following notes are in order.

(a) Equation (34) is approximate because there is an unknown correction to be made to the electric field near the optical centre, and because of the simple use of a mean luminescence energy  $e$  (see ref. [80]). It appears to give results which are correct within a factor of about three. For example, the 789 meV line has a decay time  $\tau \sim 200 \mu\text{s}$  (section 5). It occurs at a radiation-induced complex of C and O, and the concentration of the centres can be estimated from the rate of introduction of radiation damage (section 5). Equation (34) predicts the concentration of 789 meV centres to be  $\sim 0.8$  times that expected from the rate of introduction of radiation damage (section 6.4). For another check on eq. (34) we note that absorption in the local-mode vibrational bands of a defect is related to the apparent charge  $\eta$ , the refractive index  $n$  and the effective mass  $m$  of the oscillating atoms by (in SI units)

$$\int dE \mu(E) = (h/4\epsilon_0 c) \eta^2 [C]/nm. \quad (35)$$

The 789 meV line occurs at identically the same centre as the “C(3)” vibrational bands and the ratio of the electronic to the vibrational absorption is known for a given [C] (section 5). Assuming that  $\eta = 2.5$  times the electronic charge (the mean of the values for the isolated C and O atoms [81]), we can calculate [C] from the measured vibrational absorption. The result is 2.5 times the value of [C] calculated from eq. (34) using the measured electronic absorption in the same sample.

(b) In eq. (34) the concentration [C] is the concentration of the optical centres which can produce the transition of interest. They must be in the appropriate charge state (and, for bistable centres, the correct structural form). The charge state depends on the equilibrium conditions of the crystal (the energy of the ground state of the centre relative to the Fermi energy) and on the shift away from that equilibrium resulting from the experimental conditions, such as the illumination of the sample. For

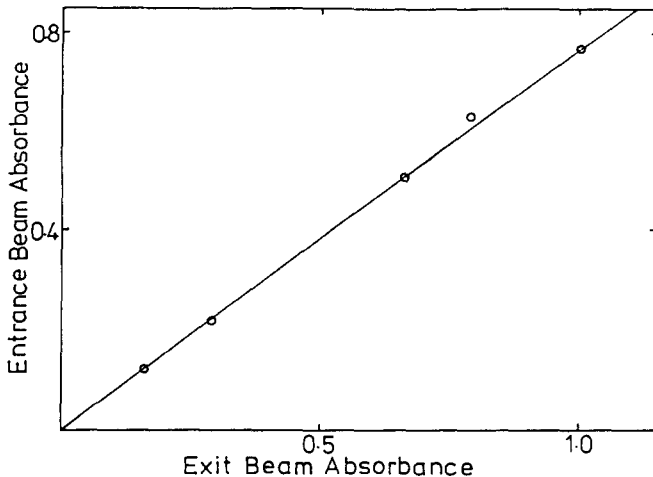


Fig. 25. Absorption in the 789 meV line (section 5.1) when the sample is mounted in the dark (i.e. in monochromated light at the exit slit of the monochromator) compared with the absorption in the same samples when bathed in above-band-gap radiation ("entrance slit") [82].

example, the 789 meV absorption line is consistently weaker when measured with the sample illuminated by strong visible light than when measured in weak illumination (e.g. after the exit slit of a monochromator; fig. 25 [82]). The charge states of defects may also change over large temperature ranges. For example, the vacancy–oxygen centres are converted from the negative charge state (giving the  $884\text{ cm}^{-1}$  absorption line, which dominates at the lowest temperatures  $\sim 20\text{ K}$ ) to the neutral charge state (giving the  $835\text{ cm}^{-1}$  line, which dominates at room temperature) [83].

(c) In eq. (34) the radiative decay time  $\tau$  is the intrinsic radiative decay time of the transition. This may not be the measured decay time because of competing decay channels. Many photoluminescence centres in silicon have multiple excited states and transitions from these have different probabilities. For example, fig. 26 shows the measured decay time  $\tau$  for luminescence from the 1045 meV band (section

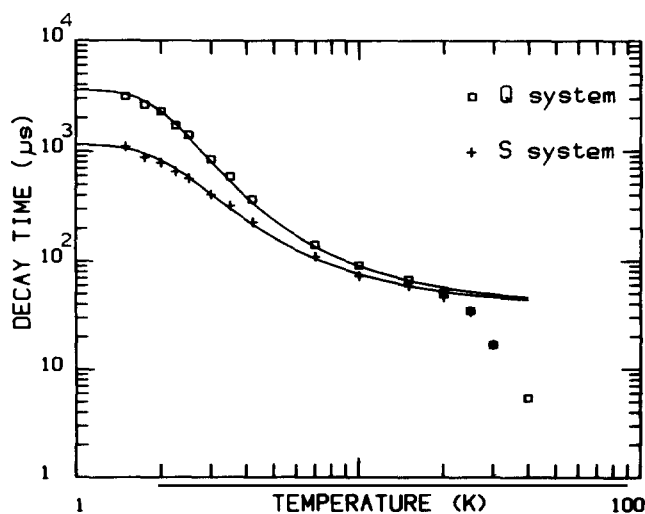


Fig. 26. Radiative decay time of the 1045 "Q" and 1082 meV "S" systems, excited by above-band-gap radiation [211].

5.5). This centre has two excited states, 1044 and 1045 meV above the ground state. The solid line on fig. 26 allows for the populations of the two excited states separated by  $\Delta E = 1$  meV and with relative degeneracies  $g_2/g_1 = 1/3$  (section 5), using

$$1/\tau = [g_1/\tau_1 + (g_2/\tau_2) \exp(-\Delta E/kT)]/[g_1 + g_2 \exp(-\Delta E/kT)]. \quad (36)$$

The calculated values of the radiative decay times for transitions from the two excited states are  $\tau_1 = 3600 \mu\text{s}$  and  $\tau_2 = 9.5 \mu\text{s}$ .  $\tau_2$  is the relevant time for use in eq. (34), since the strongly allowed transition produces most of the absorption. Finally, at  $T \geq 25 \text{ K}$  the usual quenching occurs (section 3.1).

Table 1 lists the radiative decay times and calibration factors which relate the measured strength of absorption to the concentration of various photoluminescence centres.

Taking the important 969 meV band as an example, from table 1 the integrated zero-phonon absorption at a concentration of  $10^{16} \text{ cm}^{-3}$  is  $6.8 \text{ cm}^{-2}$ . The line has a width  $\sim 0.2 \text{ cm}^{-1}$  (eq. 138), giving a peak absorption coefficient of  $\sim 30 \text{ cm}^{-1}$ . If measurements are made through a 2 mm slice, at the peak of the line only 5% of the light is transmitted. The strong peak absorption and the small linewidth create a major problem: a linewidth of  $0.2 \text{ cm}^{-1}$  at  $7800 \text{ cm}^{-1}$  is equivalent to a resolving power of 39 000, greater than the resolution possible with standard spectrometers. A dispersive spectrometer transmits a signal

Table 1

Radiative decay times of photoluminescence centres, and calibration factors  $c$  between concentrations and absorption intensity. The constant  $c$  relates the absorption coefficient  $\mu(\nu)$  in  $\text{cm}^{-1}$  integrated over the extent of the zero-phonon line to the concentration  $[o]$  in  $\text{cm}^{-3}$  of the optical centre,  $\int d\nu \mu(\nu) = c[o]$ , where  $\nu$  is in  $\text{cm}^{-1}$  and the measurement is at low temperature.

Line (meV)	Decay time ( $\mu\text{s}$ )	Temperature (K)	$c$ ( $10^{-16}$ )	Comments
488			$\sim 7$	C + O + (vacancy?). $c$ estimated from modelling radiation damage (section 6)
789	95, 200		0.43	C + O-related centre (section 5.1). Lifetimes from refs. [177, 182], $c$ from modelling radiation damage (section 6). See fig. 21
856			0.26	Interstitial carbon [224]
969	< 4		7	C-related centre (section 5.2). Lifetime from ref. [182], $c$ from section 6.2
978	3000	< 10		S-related centre [73]
1014	500	$2 < T < 13$		Cu-related centre (section 5.3) [199]
1044	3600	< 2		"Forbidden" transition of Li centre (section 5) [211]. See fig. 26
1045	9			"Allowed" transition of Li centre (section 5) [211]. See fig. 26
1050	25	$10 < T < 30$		High temperature form of Tl-related centre (section 8) [261]
1051	2	4.2		"O1'" line, split ground state
		60	1.8	With transition from lower state "forbidden" [148]
1076.3	480	< 5		Be-related isoelectronic [101]
1081	1150	< 2		"Forbidden" transition of Li + C-related centre [211]. See fig. 26.
1082	9.5			"Allowed" transition of Li + C-related centre [211]. See fig. 26
1087	53	< 10		Low temperature form of Tl-related centre (section 8) [261]
1115	2300	$T < 1$		Be-related isoelectronic [101]
1117.5	163, 3400			Two-exponential decay resulting from two atomic configurations of In-related centre [261]

See eq. (59) for decay times of excitons bound to donors and acceptors, and refs. [1, 156, 275] for calibration of the concentrations of donors and acceptors in terms of the intensity of luminescence from excitons bound to them.

$$T(\nu) = \int d\nu' I(\nu') S(\nu - \nu'),$$

where  $I(\nu)$  is the true spectral intensity at photon frequency  $\nu$  and  $S(\nu - \nu')$  is the signal recorded by the instrument at frequency  $\nu'$  for an infinitely sharp input at  $\nu$ . Because the absorption coefficient depends on the reciprocal of  $I(\nu)$ , the apparent reduction of absorption can be considerable. The effect depends on the lineshape and  $S(\nu)$ . However, if a zero-phonon line is being detected with a spectral resolution equivalent to the linewidth and the transmission at the peak of the zero-phonon line is *observed* to be 30% of that in the absence of the line, the integrated absorption in the zero-phonon line will be underestimated by  $\geq 30\%$  if no correction is made for the lack of resolution. An alternative to making a correction is to measure some weaker feature of the band such as a local-mode sideband or, for the 969 meV line, the isotope structure in the zero-phonon line (section 5).

A typical vibronic band in silicon has  $\sim 10\%$  of its intensity concentrated in the zero-phonon line (section 7.1). The remaining 90% is spread out in the vibronic sideband over  $\sim 0.1$  eV, giving a mean absorption of  $10^{-2} \text{ cm}^{-1}$ . This is sufficiently small that only very sharp spectral features can be detected. Local-mode sidebands typically have about the same width as zero-phonon lines but have integrated absorption some 10 times smaller (see section 7.1); they are already difficult to detect in absorption. Only a few vibronic sidebands have been measured fully in absorption (e.g. the 488 and 969 meV bands, section 7.1, and the 1045 meV band, section 5). In contrast the majority of the optical centres in the first group IV semiconductor, diamond, can be readily detected in absorption. The radiative decay times are shorter ( $\sim 10$  ns [21]) and many of the centres in diamond are formed from nitrogen impurity, which is present in large concentrations ( $\sim 10^{21} \text{ cm}^{-3}$ ). To measure the weak absorption spectra in silicon, the luminescence excitation technique can be used (section 3.3).

### 3.3. Luminescence excitation measurements

Luminescence excitation measurements combine the sensitivity of luminescence experiments with the ability of absorption measurements to probe higher excited states of the optical centres. The sample is excited by photons of energy  $h\nu$  chosen so that they can be absorbed directly by the optical centres. If  $\mu_c$  is the absorption coefficient of the optical centres at frequency  $\nu$ , and  $\mu_b$  is the background absorption produced by all other processes, then a fraction

$$f = \mu_c / (\mu_b + \mu_c) \quad (37)$$

of the light will be absorbed by the centres. The intensity  $I_a(\nu)$  absorbed in the sample is related to the total absorption  $\mu = \mu_b + \mu_c$ , the sample thickness  $t$ , the reflection coefficient  $R$  and the incident light intensity  $I_0(\nu)$  by

$$I_a(\nu) = I_0(\nu)(1 - R)[1 - \exp(-\mu t)] / [1 - R \exp(-\mu t)]. \quad (38)$$

Of the energy  $fI_a(\nu)$  absorbed, some fraction is emitted as luminescence. In the luminescence excitation experiment this emission is detected as a function of the excitation frequency. The plot is therefore an approximation to the absorption spectrum  $\mu_c(\nu)$  of the centre, and the exact spectrum  $\mu_c(\nu)$  can be calculated from eqs. (37) and (38) [84].

The technique requires a tunable excitation source—in practice an infra-red, continuous-output,

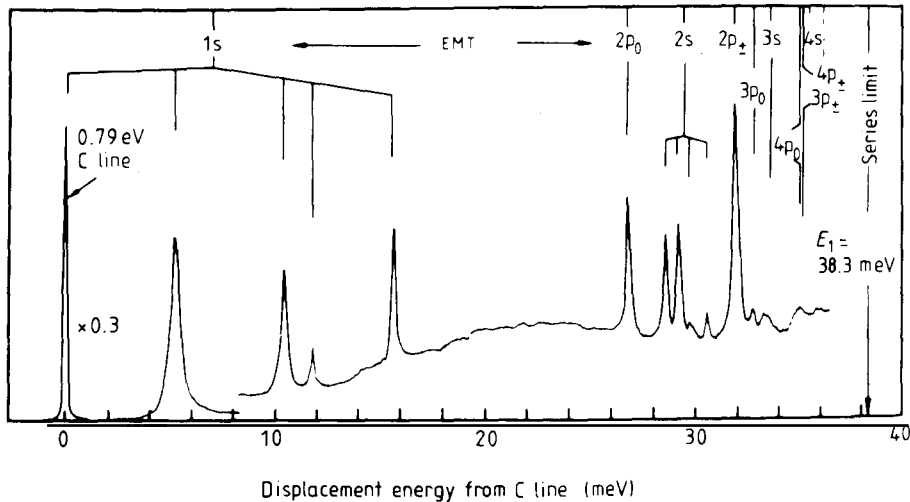


Fig. 27. Photoluminescence excitation spectrum of the 789 meV system [177].

tunable laser. The enormous potential of this technique is illustrated by the beautiful spectrum of absorption into the excited states of the 789 meV centre in fig. 27: the higher excited states are difficult to detect in direct absorption spectroscopy. Other applications of the technique to silicon are in refs. [85–89]; the phonon sidebands of the 1.17  $\mu\text{m}$  band (section 7.4) have also been measured.

### 3.4. Cathodoluminescence, electroluminescence, photothermal ionisation, two-beam absorption

Cathodoluminescence (luminescence excited by an electron beam) from silicon appears to be similar to photoluminescence excited by above-band-gap radiation. The spectra [90] have the same form, and the same temperature dependence [91] when measured by either process. The similarity is not unexpected since both excitation techniques operate by creating free electrons and holes, which subsequently de-excite to the optical centres. However, in diamond, a considerable amount of work has been done using photoluminescence excited by below-band-gap (<5.5 eV) excitation. Some optical bands (notably the 1945 meV nitrogen–vacancy band [92]) are known to be excited efficiently by photon absorption in their absorption bands but are not excited by an electron beam. Since a low energy electron beam (tens of kV) deposits its energy within a few  $\mu\text{m}$  of the surface, cathodoluminescence originates essentially from a thin surface layer, and is most efficiently collected by the 135° geometry (section 3.1.1). Note that a low energy electron beam easily creates radiation damage in silicon from bombardment by ions carried down the beam (section 6.5).

Electroluminescence, excited by an electrical current through the samples, was used in very early work on luminescence from silicon [93, 94], non-equilibrium carriers being injected through a p–n junction. Brown and Hall have shown that the efficiency of electroluminescence can be close to that of photoluminescence when carriers are injected through electrodes consisting simply of silver paint on the surface of the crystal [95]. They show that the 1117 meV In-related line is quenched at fields of 120 V/cm (in their samples), very close to the fields which produce impact ionisation in the samples of Weman et al. [76, 77]. Electroluminescence has technological applications in creating an optical communications system all on silicon.

Many defects in silicon (e.g. the divacancy [96]) are known to produce photoconductivity. Photoconductivity has been reported from the 789 and 969 meV bands [97] when the samples were held at 20 K. A potentially important advance has been reported by Kleverman et al. [98] using photothermal ionisation spectroscopy. In this technique (which is well established in studies of shallow donors and acceptors, see, e.g., ref. [99]) absorption of a photon excites a centre to a nearly ionised state. Ionisation is completed by thermal ejection of the particle into a band state. The weak optical transitions into the shallowest states are therefore enhanced, since these are the most easily thermally ionised. This technique has been applied to the excited (donor-like) states of the 789 meV centre [98], producing a spectrum similar to fig. 27.

Another way of measuring shallow excited states of photoluminescence centres is by using two light beams. One excites the centre to the first excited state, and must have sufficient energy to create a large population in that level. The second light beam is used to measure the far-infra-red absorption produced by transitions from the first excited state to the higher levels. The advantage of the method is that the selection rules for the far-infra-red absorption may allow observation of some excited states which are not easily seen by absorption from the ground state of the centre.

Figure 28 shows the energy levels of a Be-related bound exciton [100]. Photoluminescence occurs from the lowest multiplet,  $\sim$ 1075 to 1078 meV above the ground state (section 8). Photoluminescence excitation allows observation of a set of excited states at  $\sim$ 1099 to 1114 meV. These shallow states are remote from the central core of the optical centre and can be labelled with even or odd parity in the  $O_h$

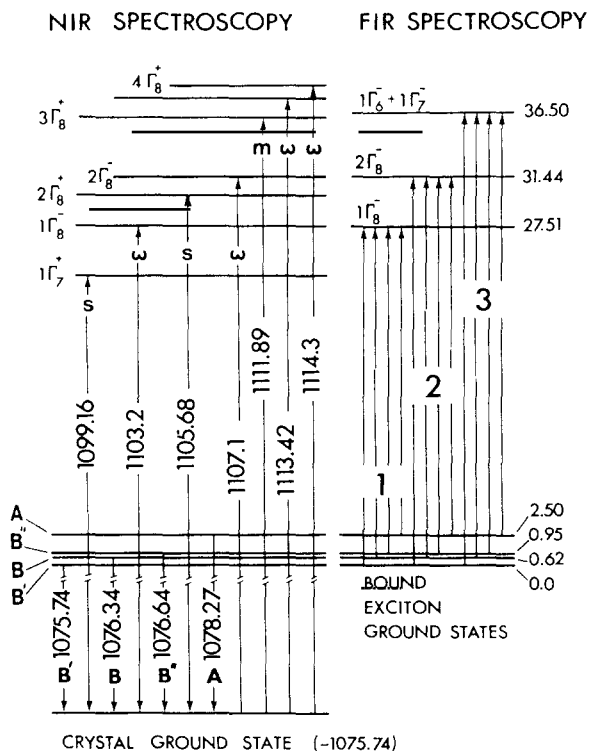


Fig. 28. Energy levels of the Be-related centre, determined by near-infra-red transitions from the ground state and by far-infra-red transitions from the first excited states of the centre [100].

crystal point group. The stronger optical transitions from the ground state are to the even-parity states. Far-infra-red absorption from the first excited multiplet occurs to the odd-parity states (fig. 28), allowing accurate measurement of these states without their being masked, as in photoluminescence excitation measurements, by the stronger transitions to the even-parity states. Since the radiative decay time of this Be centre is  $\sim 500 \mu\text{s}$  at low temperature [101], and concentrations of  $10^{16} \text{ cm}^{-3}$  are obtainable, a few tens of mW of above-band-gap laser power absorbed in  $\sim 10 \mu\text{m}$  of the sample will place a very large fraction of the centres in the first excited state, giving strong far-infra-red absorption.

## 4. Impurities

### 4.1. Carbon

Carbon complexes with many impurities in silicon, resulting in a large variety of photoluminescence centres. Photoluminescence has been unambiguously detected from carbon complexed with:

- 1) another C atom (969 meV band, section 5.2),
- 2) one oxygen atom (789 meV band, section 5.1),
- 3) one N atom (745.6 meV band),
- 4) one Ga atom (875 meV band),
- 5) the four-lithium atom complex (1082 meV band),
- 6) beryllium (1117 meV band),
- 7) numerous radiation damage centres, especially involving oxygen (e.g. at 488, 767, 769, 920, 925.5, 929, 935 and 950 meV).

In addition the (uncomplexed) carbon interstitial atom is photoluminescent (section 4.1.2). Other complexes, for example the "X" acceptors formed by pairing of a carbon atom with a Group III acceptor (B, Al or In [102]) appear to be non-luminescent [103], and further complexes (e.g. carbon + phosphorus) are reported from DLTS measurements [104, 127].

It is convenient to discuss first substitutional carbon atoms and then interstitial carbon.

#### 4.1.1. Substitutional carbon

Carbon is present in silicon primarily as a grown-in impurity, but it can also be introduced during processing (section 4.1.2). The solubility limit in conventionally grown silicon is  $(3.5 \pm 0.4) \times 10^{17} \text{ cm}^{-3}$  [105]. In commercial Czochralski silicon, [C] ranges from  $\sim 3 \times 10^{16}$  to  $2 \times 10^{17} \text{ cm}^{-3}$ , and spans about an order of magnitude lower in commercial float-zone silicon. In Czochralski silicon grown in a magnetic field values up to  $2 \times 10^{18} \text{ cm}^{-3}$  are possible [106].

The carbon atoms occupy substitutional sites, each C atom replacing one Si atom. The lattice parameter decreases with increasing carbon concentration [C] in  $\text{cm}^{-3}$  (for at least  $10^{16} < [\text{C}] < 1.3 \times 10^{17} \text{ cm}^{-3}$ ) [107],

$$\Delta d/d = -6.5 \times 10^{-24}[\text{C}]. \quad (39)$$

This change is close to that expected by linear interpolation between the extreme of pure silicon and  $\beta$ -SiC, consistent with the C atoms replacing Si atoms, rather than adding to the crystal in the form of interstitial atoms. The strain energy in the lattice resulting from this deformation is estimated at 1.76 eV

per C atom [108]. Substitutional carbon atoms have a large activation energy  $E$  in the diffusion coefficient  $D$  (in  $\text{cm}^2/\text{s}$ ) [109],

$$E = 3.15 \pm 0.2 \text{ eV}, \quad D = 1.9 \exp(-E/kT). \quad (40)$$

Energies of this size are typical of those for the established substitutional Group III and V impurities [110]. However, the enthalpy for creating monovacancies is of this order ( $3.6 \pm 0.2 \text{ eV}$  [111]). Activation energies for migration of this magnitude may therefore indicate a vacancy- or interstitial-enhanced process.

For the concentration range  $[C] \gtrsim 10^{15} \text{ cm}^{-3}$ ,  $[C]$  may be measured from the strength of the infra-red absorption produced by excitations of the local-mode vibrations of the isolated substitutional C atoms. The local-mode quanta, measured at room temperature for  $^{12}\text{C}$ ,  $^{13}\text{C}$  and  $^{14}\text{C}$  isotopes, are [112]

$$\begin{aligned} \hbar\omega(^{12}\text{C}) &= 607 \text{ cm}^{-1} = 75.3 \text{ meV}, & \hbar\omega(^{13}\text{C}) &= 586 \text{ cm}^{-1} = 72.7 \text{ meV}, \\ \hbar\omega(^{14}\text{C}) &= 572 \text{ cm}^{-1} = 70.9 \text{ meV}. \end{aligned} \quad (41)$$

These quanta increase by  $\sim 2.5 \text{ cm}^{-1}$  on cooling to 77 K [113]. The calibration was first established by Newman and coworkers [112, 113] using  $^{14}\text{C}$ -doped samples so that  $[C]$  could be measured. Later work [107, 114, 115] has substantially confirmed the original calibration, and the technique is now the recognised ASTM method [116]. The absorption coefficient  $A$  (in  $\text{cm}^{-1}$ ) produced at the peak of the  $607 \text{ cm}^{-1}$  line, measured at room temperature with a full width at half height of  $6 \text{ cm}^{-1}$ , is taken to be related to  $[C]$  in  $\text{cm}^{-3}$  by

$$[C] = 1.0 \times 10^{17} A, \quad (42)$$

and the conversion factor is  $4.5 \times 10^{16} \text{ cm}^{-2}$  for a linewidth of  $3 \text{ cm}^{-1}$  at 77 K; an accuracy of  $\pm 10\%$  is estimated. Comparison of the total amount of carbon in the silicon crystals (as measured by a mass-spectroscopic or radio-isotope method, which is insensitive to the lattice location of the atoms) with the  $607 \text{ cm}^{-1}$  absorption (which is specific to the substitutional site) shows that in typical as-grown silicon the carbon can be assumed to be primarily on the substitutional sites. However, complexing with oxygen is observed at high concentrations of C and O [117]. Carbon can also be precipitated, for example by prolonged heating ( $\sim 100$  hours) at high temperatures ( $\sim 1000$  to  $1250^\circ\text{C}$ ). Cubic  $\beta$ -SiC is then formed, and can be recognised by its absorption bands near  $830 \text{ cm}^{-1}$ .

The lower limit to measuring the concentration of carbon by the local-mode method (eq. 42) is determined by the  $607 \text{ cm}^{-1}$  peak being superimposed on the strongest intrinsic two-phonon lattice absorption peak formed from the TA and TO phonons from both the  $\langle 001 \rangle$  and  $\langle 111 \rangle$  zone boundaries [33] (fig. 6). When measuring at liquid nitrogen temperature (77 K), the intrinsic absorption is reduced relative to its room temperature value, and the C line is sharpened but not appreciably changed in intensity. Higher accuracy is then possible in samples of low  $[C]$ . Spectra are often measured using the difference in absorption of the sample under investigation and a supposedly carbon-free reference sample measured at precisely the same temperature, for the underlying two-phonon absorption is temperature dependent. A considerably more sensitive measurement of carbon is obtained using photoluminescence, but at the cost of its being a destructive method (section 4.1.2). There is no known electronic transition associated with the substitutional C atom, but a Raman scattering line is observed

with quanta reported at 10 K in  $^{12}\text{C}$ - and  $^{13}\text{C}$ -implanted silicon as [118]

$$\hbar\omega(^{12}\text{C}) = 604.1 \text{ cm}^{-1} = 74.9 \text{ meV}, \quad \hbar\omega(^{13}\text{C}) = 586.1 \text{ cm}^{-1} = 72.7 \text{ meV}. \quad (43)$$

These values (from implanted silicon) are lower than those of eq. (41) from more perfect crystals. For use in section 7.5 we note that the ratios of the frequencies are

$$\begin{aligned} \text{eq. (43): } & \hbar\omega(^{12}\text{C})/\hbar\omega(^{13}\text{C}) = 1.031, \\ \text{eq. (41): } & \hbar\omega(^{12}\text{C})/\hbar\omega(^{13}\text{C}) = 1.036, \\ \text{eq. (41): } & \hbar\omega(^{12}\text{C})/\hbar\omega(^{14}\text{C}) = 1.061, \end{aligned} \quad (44)$$

and are intermediate between the values expected for a C atom in an immovable environment,

$$(13/12)^{1/2} = 1.041, \quad (14/12)^{1/2} = 1.080, \quad (45)$$

and for a C atom vibrating against one Si atom in a diatomic molecule,

$$\begin{aligned} \hbar\omega(^{12}\text{C})/\hbar\omega(^{13}\text{C}) &= [13 \times 28 \times (12 + 28)/12 \times 28 \times (13 + 28)]^{1/2} = 1.028, \\ \hbar\omega(^{12}\text{C})/\hbar\omega(^{14}\text{C}) &= [14 \times 28 \times (12 + 28)/12 \times 28 \times (14 + 28)]^{1/2} = 1.054. \end{aligned} \quad (46)$$

#### 4.1.2. Interstitial carbon

A substitutional carbon atom C(s) is displaced by a self-interstitial I, creating an interstitial carbon atom C(i), with I moving into its vacant site [119, 121]. The displacement mechanism occurs down to at least 77 K (section 6.2); the lower temperature limit is not known.

The first optical identification of C(i) was by absorption in its local modes which have quanta at 77 K of [119, 120]

$$\hbar\omega(^{12}\text{C}) = 922 \text{ cm}^{-1} = 114 \text{ meV}; \quad \hbar\omega(^{14}\text{C}) = 932 \text{ cm}^{-1} = 115.(5) \text{ meV}. \quad (47)$$

In  $^{13}\text{C}$ - and  $^{14}\text{C}$ -doped silicon the two modes of C(i) are shifted to [121]

$$\hbar\omega(^{13}\text{C}) = 892 \text{ and } 904 \text{ cm}^{-1}, \quad \hbar\omega(^{14}\text{C}) = 867 \text{ and } 881 \text{ cm}^{-1}. \quad (48)$$

As for C(s), eq. (44), the frequencies are in the ratios  $\hbar\omega(^{12}\text{C})/\hbar\omega(^{13}\text{C}) = 1.03$  and  $\hbar\omega(^{12}\text{C})/\hbar\omega(^{14}\text{C}) = 1.06$ .

In photo-luminescence or absorption C(i) is identified by the electronic transition at 856 meV [122]. The photoluminescence band (fig. 29) shows no local modes, and the zero-phonon line shows no isotope effects in  $^{13}\text{C}$ -doped silicon: there are thus no isotope data to confirm unambiguously the presence of C in this centre. However, the production and destruction of the 856 meV line correlates accurately with the vibrational absorption in its local modes [121]. In addition a paramagnetic resonance signal ("G12" [124]) is identified at the centre (in a different charge state from that giving the infra-red

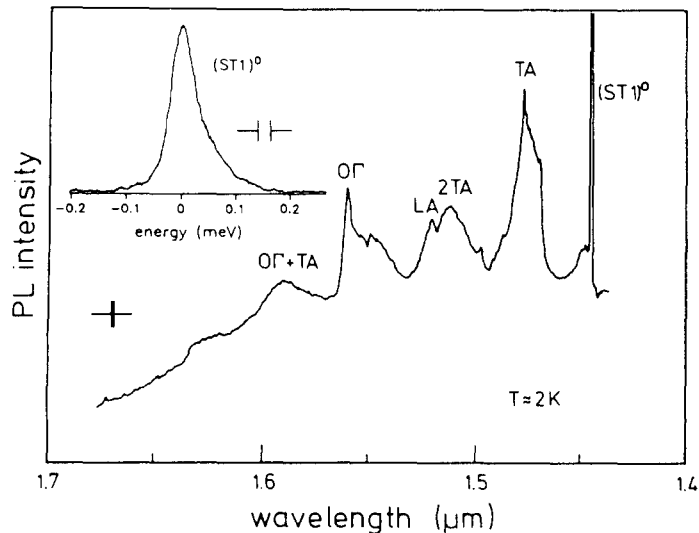


Fig. 29. Photoluminescence from the interstitial carbon atom, and (inset) its zero-phonon line. The band is superimposed on a broad background [123].

vibrational and electronic bands). A DLTS signal assigned to the positive charge state of the centre at  $E_v + 0.30 \pm 0.2$  eV [125, 126] shows evidence for bistability of the centre.

From the paramagnetic resonance data the carbon “interstitial” is found to share one lattice site with a Si atom (a  $\langle 001 \rangle$  split interstitial configuration [124], fig. 30). The same symmetry is found from the effects of uniaxial stresses on the electronic transition [122, 123]. Since no Zeeman splitting is observed in the 856 meV line, the electronic transition, and hence the vibrational absorption, apparently occur in

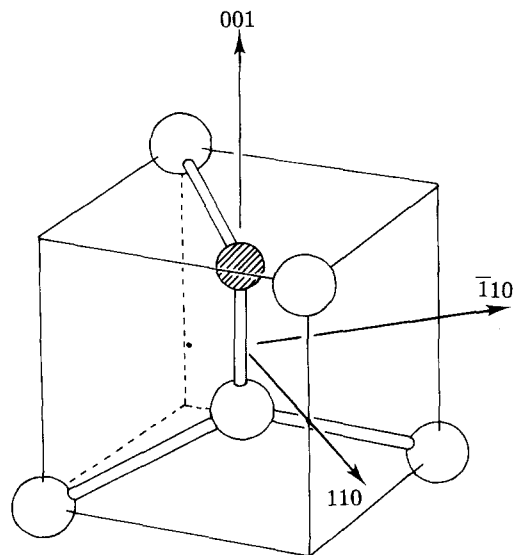


Fig. 30. Model from the Si-G12 paramagnetic resonance signal for the interstitial carbon atom, with the carbon atom shown shaded. The C atom and one Si share a crystal site [124].

the neutral charge state of the centre, in contrast to the positive state observed in paramagnetic resonance. Evidently the centre is stable in the same configuration in the two charge states. This nearly tetragonal symmetry splits the local modes of C(i) into the two observed lines at 922 and 932 cm<sup>-1</sup> with their intensity ratio of 2 : 1.

In contrast to substitutional carbon, “interstitial” C is highly mobile. Its thermally activated migration energy is currently uncertain but lies in the range [122, 124, 125, 128–130]

$$E = 0.72 \text{ to } 0.88 \text{ eV}. \quad (49)$$

Two traps for a migrating interstitial carbon atom are a substitutional carbon atom and an interstitial oxygen atom (section 6.4). In addition, C(i) atoms may be trapped at condensations of self-interstitials on C(i) atoms [131, 132]. After small radiation doses, in float-zone silicon (negligible oxygen content) with a concentration of substitutional carbon of [C] cm<sup>-3</sup>, the decay time *t* (s) for thermally activated trapping of C(i) at C(s) has been described by [131]

$$t = 1.7 \times 10^6 \exp(0.87 \text{ eV}/kT)/[C]. \quad (50)$$

In this limit of relatively sparse trapping points, the decay time is inversely proportional to the concentration of C(s) atoms.

Because a self-interstitial is captured by a C(s) atom to produce a C(i), the loss of C(s) (which can be measured, section 4.1.1) gives the production of C(i) atoms, and hence the oscillator strength of the C(i) absorption lines. The calibration, which must be done in the limit of low doses to avoid reactions of self-interstitials with C(i), gives [132]

$$\sum HW = 1.3 \times 10^{-16} [C(i)], \quad (51)$$

where the sum is over the peak absorption *H* (cm<sup>-1</sup>) and the full width at half height *W* (cm<sup>-1</sup>) in both the 922 and 932 cm<sup>-1</sup> lines. Because the absorption in the 922 cm<sup>-1</sup> line (2/3 of the sum of the two lines) has been related to the absorption in the 856 meV zero-phonon line (measured at 2 K [122]), we can cross-calibrate the absorption in the 856 meV line,

$$\int dE \mu(E) = 2.6 \times 10^{-17} [C(i)], \quad (52)$$

where the integral (in cm<sup>-2</sup>) is over the 856 meV zero-phonon line at 2 K and [C(i)] is in cm<sup>-3</sup>. This gives the first absolute determination of the dipole strength of an electronic band in silicon.

During processing, interstitial carbon atoms may be introduced into crystalline silicon. This provides a highly sensitive, but destructive, method of measuring the concentration of the substitutional carbon already in the silicon. For example, C atoms may be driven in from a CF<sub>4</sub> plasma [4], or as an incidental effect of irradiating the silicon with low energy (~20 keV) electrons (section 6.5). If the silicon is at a temperature greater than room temperature (eq. 49), the C(i) atoms are highly mobile. In Czochralski (oxygen-rich) silicon, mobile interstitial carbon atoms are captured either by existing substitutional carbon atoms C(s), or by oxygen atoms O (section 6.4). If enough C(i) atoms are introduced into the silicon that all the C(s) atoms are saturated, then the concentration of C(s) + C(i) centres will be proportional to [C(s)]. The photoluminescence intensity of the resulting 969 meV band (section 5),

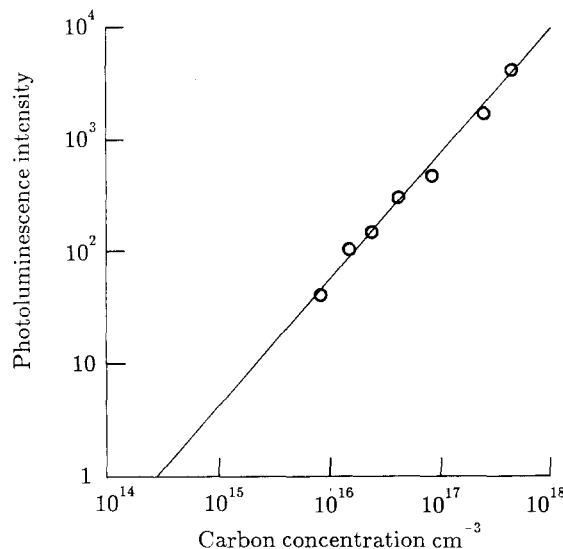


Fig. 31. Correlation obtainable between 969 meV luminescence measured under fixed conditions and carbon concentration, after in-diffusing C from  $\text{CF}_4$  [4].

measured under standardised conditions after in-diffusion of C(i) from a  $\text{CF}_4$  plasma, is proportional to  $[\text{C(s)}]$  (fig. 31) [4]. It is suggested that this method enables  $[\text{C(s)}]$  to be measured to two orders of magnitude lower than by the standard ASTM method (section 4.1.1). One major advantage of these techniques is that they enable the carbon concentration to be measured in the surface layer (the top few  $\mu\text{m}$ ) [3].

Because the capture radius of a self-interstitial I at C(s) is apparently not strongly dependent of temperature (over the range  $T < 500^\circ\text{C}$  [133]), carbon can be used to monitor interstitial processes in silicon. For example, from the removal of C(s) atoms during oxygen aggregation it has been deduced that one self-interstitial is released when a pair of O atoms coalesce [134]. Carbon interstitials are themselves traps for self-interstitials, and act as precipitation points for self-interstitials [132], as do other carbon complexes (section 6.4).

#### 4.2. Oxygen

Oxygen is a key impurity in silicon. Metallic contaminants are removed from processed silicon by trapping them during precipitation of the oxygen. Additionally there is considerable interest in the “thermal donors” produced by heating oxygen-rich silicon at  $\sim 450^\circ\text{C}$ . The structure of these donors remains unknown despite intensive work [135].

Oxygen is incorporated when a silicon crystal is pulled from molten Si held in a silica crucible in the Czochralski growth process. Dissolution of the crucible into the melt also releases other impurities, notably boron. The solubility of oxygen in silicon is described by [136]

$$[\text{O}] = C \exp(-E/kT), \quad C = 9 \times 10^{22} \text{ cm}^{-3}, \quad E = 1.52 \pm 0.3 \text{ eV}. \quad (53)$$

Consequently equilibrium concentrations at the melt temperature are  $\sim 2 \times 10^{18} \text{ cm}^{-3}$ . This concentration is largely frozen in during cooling, leaving the silicon crystal grossly supersaturated in oxygen.

The concentration  $[O]$  is determined spectroscopically from the absorption produced by a vibrational mode at  $1106\text{ cm}^{-1}$ .  $[O]$  in  $\text{cm}^{-3}$  is then given by  $(3.03 \pm 0.02) \times 10^{17}$  times the peak absorption coefficient in  $\text{cm}^{-1}$  measured at room temperature [137].

The oxygen is incorporated as isolated interstitial atoms, with preferential bonding to two adjacent Si atoms. Vibrational motion parallel to the  $\langle 111 \rangle$  axis of this pair of Si atoms produces the  $1106\text{ cm}^{-1}$  line [138]. Diffusion of the oxygen atom occurs by an elementary step in which it jumps from one  $\langle 111 \rangle$  bond to an adjacent one. The formation of oxygen pairs and larger clusters decreases the concentration of interstitial oxygen atoms towards the equilibrium value at the current temperature (eq. 53). Over the temperature range  $250^\circ\text{C}$  to the melting point the diffusion coefficient  $D$  in  $\text{cm}^2\text{ s}^{-1}$  is given by [136]

$$D = 0.1 \exp(-2.53 \text{ eV}/kT). \quad (54)$$

Individual diffusion steps may occur faster [139] depending on the presence of other defects in the silicon [140]. Consequently, an arbitrary piece of Czochralski silicon contains high concentrations of oxygen, mainly as isolated interstitial O atoms but with small clusters of oxygen atoms dependent on the thermal history. These clusters could have significant interaction with other mobile defects (as in the models of thermal donor formation by self-interstitials being captured at oxygen clusters [141]).

Interstitial oxygen expands the lattice linearly in the concentration  $[O]$  [142],

$$\Delta d/d = 1.04 \times 10^{-24} [O] \text{ cm}^3. \quad (55)$$

The lattice expansion is important in broadening photoluminescence lines (section 10.1). The expansion is in the opposite sense to the lattice changes produced by carbon. Preferential pairing of O and C occurs [113], giving vibrational absorption lines at 588, 640, 690 and  $1103\text{ cm}^{-1}$ . There is also a strong interaction between vacancies and oxygen to form the “A centre” (section 6.2). (An attraction between self-interstitials and oxygen has also been proposed [119].)

The isolated interstitial oxygen atoms do not produce photoluminescence. Heating Czochralski silicon at  $\sim 450^\circ\text{C}$  for tens of hours (the conditions for producing thermal donors) results in a variety of vibronic bands. The P and H luminescence centres with zero-phonon lines at 767 and 962 meV are carbon–oxygen complexes (section 7.5). The “F” series of bound multi-exciton lines (section 4.3) occur at a set of centres [144] which are produced more rapidly with increasing C content, again suggesting C–O complexes. Similarly the “S” lines (fig. 32) are preferentially produced in silicon of both high C and O content [144]. Complexes ascribed to Al–O are produced by heating aluminium-doped silicon at  $450^\circ\text{C}$  [145].

It appears that many photoluminescence lines are produced under conditions similar to those used for thermal donor production (e.g. ref. [3]). This is not surprising. Migration of oxygen allows complexing with other impurities. Oxygen complexing with itself liberates self-interstitials [146], which can make mobile other species (notably carbon, section 4.1.2). When thermal donors are destroyed by annealing further motion of defects is likely, modifying photoluminescence centres. The growth and destruction of luminescence centres in parallel with thermal donors is not surprising. Two sets of iso-electronic centres are tentatively assigned to the cores (and modified cores) of thermal donors [147, 148], but no photoluminescence complex has yet been unambiguously related to thermal donors. This failure may have a parallel with the carbon-related radiation damage centres. The 789 and 969 meV centres can capture self-interstitials (sections 5.1, 5.2), producing small condensations of defect atoms, none of which is observable by photoluminescence.

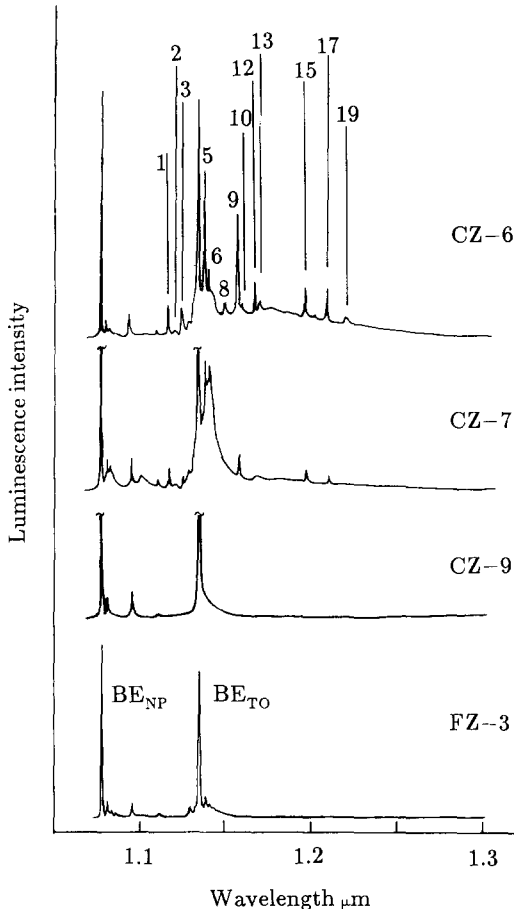


Fig. 32. Variations in luminescence after heating three samples of Czochralski silicon and one sample of float-zone silicon at 500°C for 100 h [144].

#### 4.3. Donors and acceptors

Effective mass donors are produced by substitutional Group V impurities (P, As, Sb, Bi) and by the interstitial Group I impurity Li. In its ground state the electron is perturbed by the impurity, splitting the six-fold orbital degeneracy of the conduction band minima (section 2.2) into  $\Gamma_1$ ,  $\Gamma_3$  and  $\Gamma_5$  states. For the substitutional impurities, the lowest energy state is the  $\Gamma_1$  orbital singlet, but for the Li interstitial the lowest are the almost degenerate  $\Gamma_3$  and  $\Gamma_5$  combinations, with the  $\Gamma_1$  state lying higher. This difference affects the luminescence properties as shown below. Effective mass acceptors are produced by substitutional B, Al, Ga, In and Ti.

Optical absorption is produced by creating an exciton bound to the donors and acceptors (e.g. refs. [149, 150]). However, the absorption is weak, with oscillator strengths  $\sim 10^{-5}$  to  $10^{-4}$ , corresponding to radiative lifetimes  $\tau_r$  [from eq. (34)] of

$$\tau_r \sim 750 \text{ } \mu\text{s}. \quad (56)$$

Luminescence from these impurities is easily observed [151] even though the luminescence efficiency is

less than 1% [152]. We consider the luminescence first from low concentrations of centres under low excitation powers, then under higher powers, and finally from high concentrations.

At low concentrations of donors and acceptors,  $\leq 10^{17} \text{ cm}^{-3}$ , excitation of the crystal by above-band-gap photons allows the neutral donors and acceptors to capture an exciton. The binding energies of the exciton are obtained as the difference between the corresponding free-exciton and bound-exciton luminescence. Acceptors have exciton binding energies  $B'$  [38, 153],

$$\begin{aligned} B'(\text{B}) &= 3.8 \text{ meV}, \quad B'(\text{Al}) = 5.1 \text{ meV}, \quad B'(\text{Ga}) = 5.7 \text{ meV}, \\ B'(\text{In}) &= 14.0 \text{ meV}, \quad B'(\text{Tl}) = 43.8 \text{ meV}, \quad \text{all } \pm 0.2 \text{ meV}. \end{aligned} \quad (57)$$

Donors have [38, 53, 153]

$$\begin{aligned} B'(\text{P}) &= 4.7 \text{ meV}, \quad B'(\text{As}) = 5.4 \text{ meV}, \quad B'(\text{Sb}) = 5.0 \text{ meV}, \quad B'(\text{Bi}) = 7.7 \text{ meV}, \\ B'(\text{Li}) &= 3.6 \text{ meV}. \end{aligned} \quad (58)$$

The values are  $\sim 0.1$  of the binding energy of the electron/hole on the bare donor/acceptor, in accordance with Haynes' empirical rule [151].

At low excitation powers (using  $\leq 200 \text{ mW/mm}^2$  visible light to excite silicon at 4.2 K) the luminescence from all the donors has the same structure [154]. A zero-phonon line is accompanied by phonon sidebands with wavevector-conserving phonons of 18, 56 and 58 meV (features labelled  $a_1$  on fig. 33). Acceptor spectra are similar (features  $B_1$  on fig. 34) except for an additional splitting in the zero-phonon level of Al, Ga and In, as discussed below. The widths of the phonon sidebands increase with the exciton binding energy (i.e. with the extent of localisation on the donor/acceptor). The width is caused primarily by the spread in energy of the coupled phonons [155]. Consequently for each species of centre the order of increasing widths is TA, TO, LO, the order of the gradients  $dE/dk$  of the

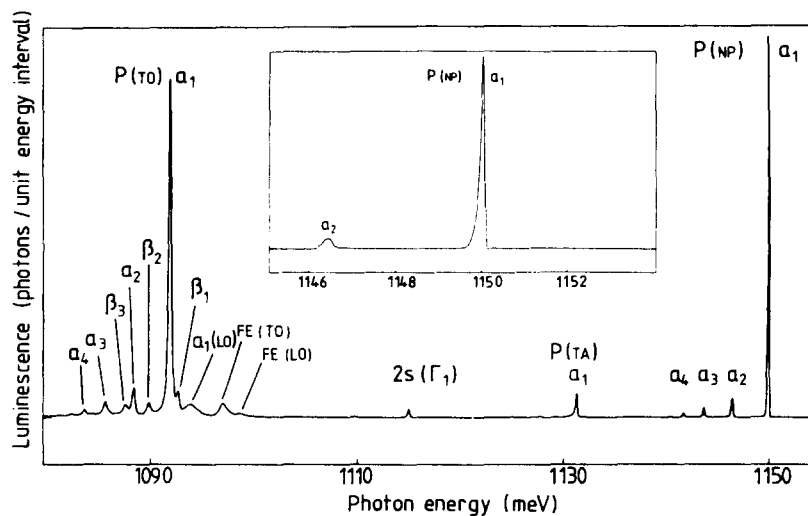


Fig. 33. Photoluminescence from float-zone silicon with  $[P] = 3.2 \times 10^{14} \text{ cm}^{-3}$ . The zero-phonon region is expanded in the inset [1].

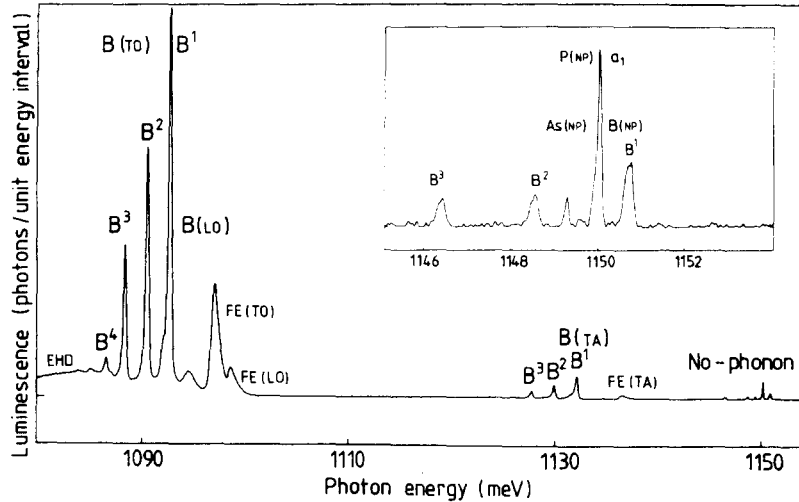


Fig. 34. Photoluminescence from float-zone silicon with  $[B] = 1.3 \times 10^{13} \text{ cm}^{-3}$ . The zero-phonon region (shown in the inset) reveals the presence also of  $1.8 \times 10^{12} \text{ cm}^{-3}$  P and  $3 \times 10^{11} \text{ cm}^{-3}$  As [1].

phonons whose wavevectors are  $\mathbf{k} = \langle 0.85, 0, 0 \rangle$  (fig. 4). The absolute widths ( $\leq 0.1 \text{ meV}$  for the TO line of P [155]) indicate lifetimes for these phonons of  $\gtrsim 10^{-11} \text{ s}$ .

The binding energies  $B'$  (eqs. 57, 58) of different donors and acceptors are sufficiently different that the photoluminescence emitted by the decay of the bound exciton is characteristic of the particular impurity, allowing the luminescence energies to be used for chemical analysis of the silicon [1, 156]. The only ambiguity likely is that the binding energies of Sb and P are similar: these elements are distinguishable by the different intensity ratios of their zero-phonon lines and the TO sidebands [53].

Quantitative analysis of the impurities is also possible from the intensities of the bound-exciton lines. To correct for experimental variables, the ratio of the intensities of the bound and free excitons is used. To provide a large luminescence signal the data are taken at the largest power that can be tolerated without excessively heating the sample (about 300 mW visible laser power incident on a  $1 \text{ mm}^2$  spot with the sample immersed in liquid helium [1]). Under these conditions luminescence from electron-hole drops (section 2.2) is seen at low impurity concentrations (fig. 34). The ratio of the luminescence emitted by the bound excitons and the free excitons is remarkably linear (e.g. ref. [157]), with a slope near unity in the concentration of the impurity (fig. 35), and allows concentration measurements in at least the range  $10^{12}$  to  $10^{16} \text{ cm}^{-3}$  when the sample is at 4.2 K. Higher concentrations (up to  $10^{18} \text{ cm}^{-3}$ ) can be measured by increasing the temperature when the difference between  $B'$  and the internal binding energy of the exciton (eq. 14) biases the luminescence towards the free excitons.

The importance of photoluminescence in measuring donor and acceptor concentrations is that during the measurement the sample is bathed in above-band-gap light, making all the donors and acceptors neutral. The photoluminescence signal measures simultaneously the concentrations of all donors and acceptors in the crystal, in contrast to an electrical method which looks at the uncompensated fraction of the major species. Hydrogen passivation, however, deactivates the shallow centres [158].

A substitutional donor with one bound exciton has two electrons and one hole. The two electrons spin-pair in the  $\Gamma_1$  state; this orbital singlet is then fully occupied. The hole is in one of the  $\Gamma$  states constructed from the valence band maxima. Recombination of the hole with either (equivalent) electron produces the  $a_1$  transitions on figs. 33 and 36. At an acceptor, a bound exciton produces a

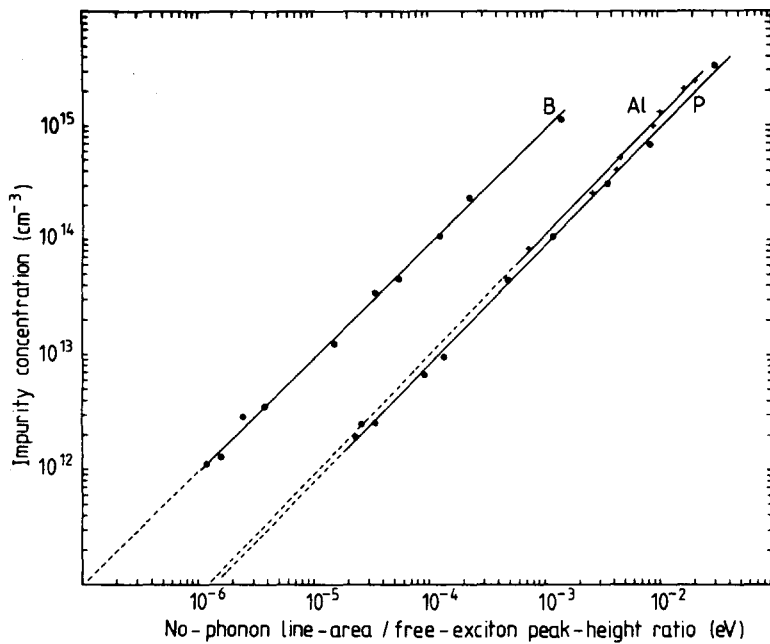


Fig. 35. Calibration for [B], [Al] and [P] using the ratio of the bound-exciton zero-phonon area and the free-exciton peak height [1].

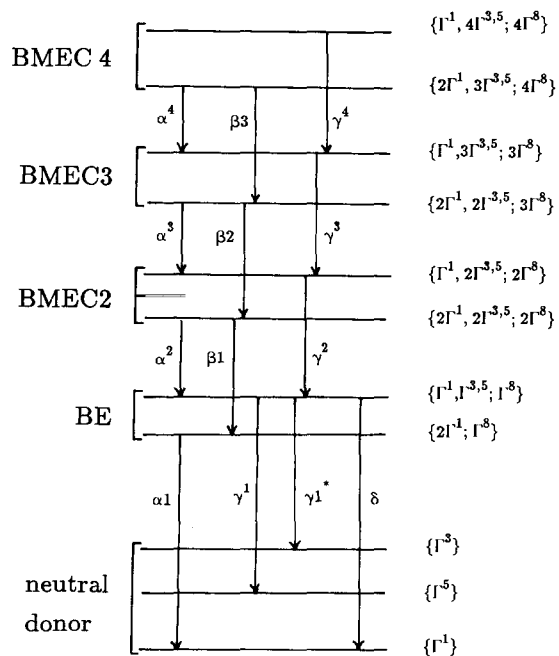


Fig. 36. Shell model for energy of a substitutional donor binding up to four excitons [8].

complex with one  $\Gamma_1$  electron and two  $\Gamma_8$  holes. Because the electron is repelled from the acceptor core the valley-orbit splitting of the conduction band minima is negligible and the  $\Gamma_1$ ,  $\Gamma_3$  and  $\Gamma_5$  states remain as a 12-fold degenerate level. The electron occupies one of these 12 states. Since the  $\Gamma_8$  hole states are four-fold degenerate there is freedom for the two  $j = 3/2$  holes to form  $J = 0$  and  $J = 2$  states (other states being forbidden by the requirement of an antisymmetric wavefunction). For B these hole states are degenerate, for the heavier acceptors their degeneracy is lifted (giving the lines starting at  $J = 0$  and  $J = 2$  states on fig. 37).

From fig. 35 there is  $\sim 10$  times less zero-phonon emission from the acceptor B than from an equal concentration of Al. This is the result of only  $\sim 1\%$  of the B luminescence being emitted in the zero-phonon line compared with  $\sim 20\%$  for Al, balanced partly by the much higher efficiency of the B centre. The luminescence efficiency of excitons bound to neutral centres is limited by the radiationless Auger decay process, in which the energy released by recombination of the exciton is used to excite the electron/hole remaining on the neutral donor/acceptor. The radiative decay times  $\tau_d$  measured at 4.2 K [159] tend to decrease with increasing binding energy, as the exciton becomes more localised on the centre. Values are

$$\begin{aligned} \tau_d(\text{B}) &= 1055 \text{ ns}, & \tau_d(\text{Al}) &= 76 \text{ ns}, & \tau_d(\text{Ga}) &= 77 \text{ ns}, & \tau_d(\text{In}) &= 2.7 \text{ ns}, & \tau_d(\text{Tl}) &= 0.27 \text{ ns}, \\ \tau_d(\text{P}) &= 272 \text{ ns}, & \tau_d(\text{As}) &= 183 \text{ ns}, & \tau_d(\text{Bi}) &= 8.6 \text{ ns}, & \tau_d(\text{Li}) &= 1150 \text{ ns}. \end{aligned} \quad (59)$$

Combined with eq. (56) these values are consistent with the very low quantum efficiencies of the centres. An additional de-excitation process occurs when recombination of the exciton emits a photon and excites the remaining bound particle to a higher excited state of the centre [160].

With increasing excitation power the bound exciton spectra become considerably richer in structure. For substitutional donors the a1 bound-exciton zero-phonon line is supplemented by lines a2, a3, a4 (fig. 33), with the higher-index lines strengthening relatively as the excitation density increases [161]. These zero-phonon lines are formed by recombination of a second, third and fourth exciton,

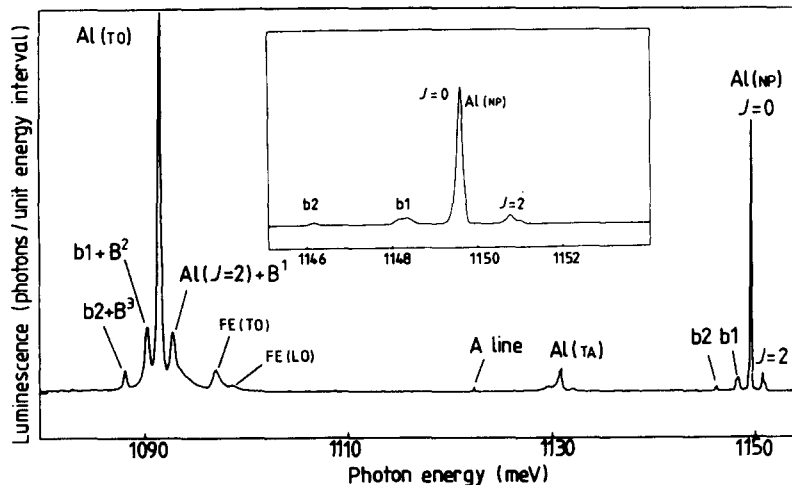


Fig. 37. Photoluminescence from float-zone silicon with  $[\text{Al}] = 2.7 \times 10^{14} \text{ cm}^{-3}$ , with the zero-phonon line expanded in the inset [1].

respectively, bound to the donor. Because the first exciton fills the  $\Gamma_1$  electron states, the electron of the second exciton is forced to occupy one of the  $\Gamma_3$  or  $\Gamma_5$  states. The hole occupies another of the four  $\Gamma_8$  states. The total complex is denoted  $\{2\Gamma_1, \Gamma_{35}; 2\Gamma_8\}$  on fig. 36. Recombination of one electron and one hole may proceed in two ways. Either a  $\Gamma_1$  electron may recombine with a hole (producing the  $\alpha$  lines on fig. 33) or the  $\Gamma_{35}$  electron may annihilate a hole (giving the  $\beta$  series of lines on fig. 33). Additionally at higher temperature one of the electrons may be excited from the  $\Gamma_1$  state to an empty  $\Gamma_{35}$  state producing the  $\gamma$  series (fig. 36).

The situation with the interstitial donor Li is interestingly different. Here the lowest energy electron state in the donor is one of the (essentially degenerate)  $\Gamma_3$  and  $\Gamma_5$  states. The total degeneracy here is 10 so that as the first 9 excitons are added their electrons fill these states. The holes progressively fill the four  $\Gamma_8$  states; with the addition of the fifth exciton the hole must go into another hole state (fig. 38). The Li spectrum of fig. 39 shows, in agreement, no great change in relative transition probabilities for the first four bound excitons, but with more bound excitons there is a fall in relative intensity. Note in contrast that the drop in luminescence intensity occurs for P at the second bound exciton, following closure of the first electron shell (fig. 33). The Auger process evidently does not increase substantially with the increasing number of bound particles.

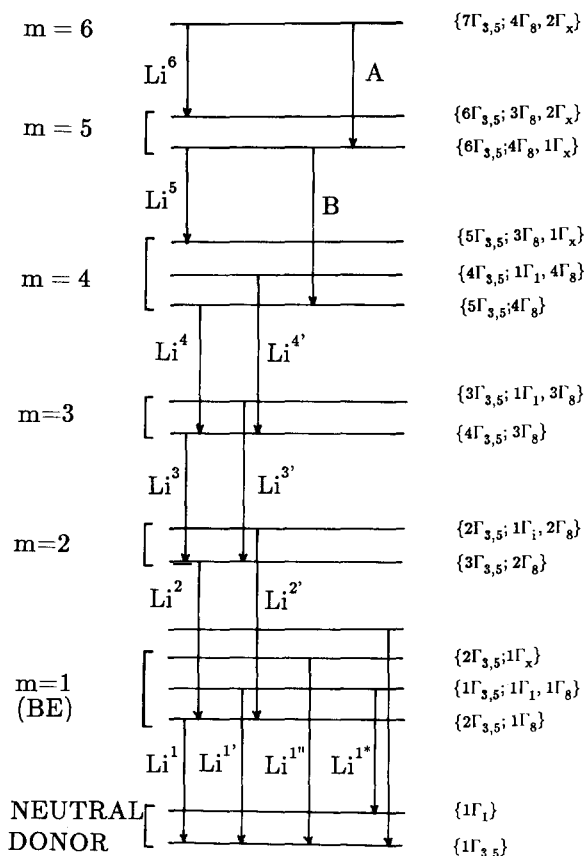


Fig. 38. Shell model for energy of the interstitial donor Li binding up to six excitons [8].

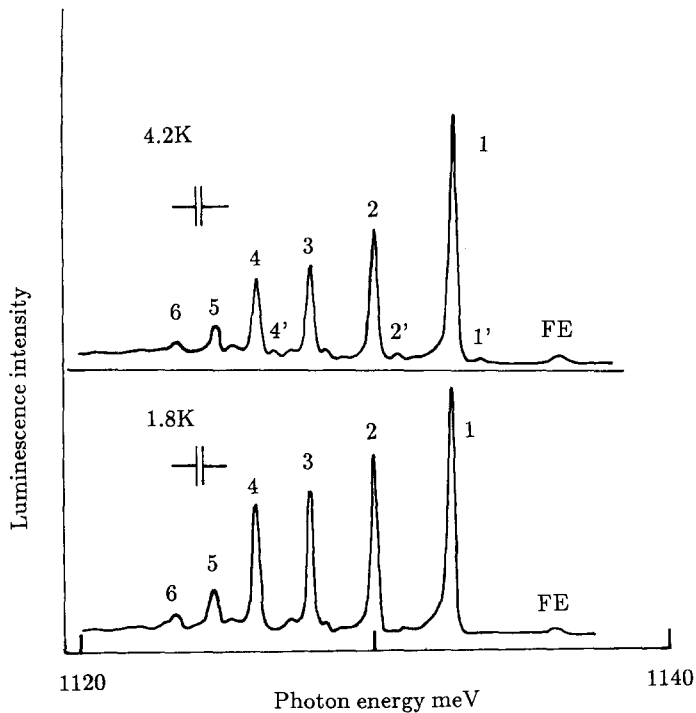


Fig. 39. Photoluminescence at 1.8 and 4.2 K from multi-excitons bound to Li donors [8].

This "shell model", developed by Kirczenow [162, 163], is discussed at length by Thewalt [8], including its successful application to acceptor spectra, and the effects of externally applied perturbations.

When both donors and acceptors are in the silicon, excitation with above-band-gap light allows both types of centre to become neutral. Recombination of a bound electron with a hole bound to an acceptor a distance  $r$  away results in zero-phonon luminescence at

$$h\nu = E_g - (E_d + E_a) + e^2/4\pi\epsilon r , \quad (60)$$

where  $E_g$  is the energy gap,  $E_d$  and  $E_a$  binding energies (of single particles) at the donor and acceptor and the final term is the Coulomb energy of the two centres. For low concentrations ( $\leq 10^{16} \text{ cm}^{-3}$ ) of donors and acceptors, large separations ( $r \gtrsim 50$  atomic spacings) are most probable. The range of  $r$  results in a spread in luminescence energies. Because the radiative recombination rate decreases exponentially as  $r$  increases, the bandshape shifts to longer wavelengths as the time increases after a pulse of excitation. The photoluminescence lineshapes for various combinations of donors and acceptors are discussed in ref. [164]. Direct observation of the transfer of electrons from P to B centres can be observed by the loss of paramagnetic resonance at the donors [165], verifying the non-exponential decay rate resulting from different separations.

With concentrations  $> 10^{17} \text{ cm}^{-3}$  the optical transitions broaden as the diffuse excited states interact with more than one centre [150]. At higher concentrations, for example if the donor concentration is  $\sim 2 \times 10^{18} \text{ cm}^{-3}$  and there are also residual acceptors at  $\sim 10^{16} \text{ cm}^{-3}$ , several donors may lie within the Bohr radius of each acceptor centre. Modified donor-acceptor spectra can then occur, characterised by

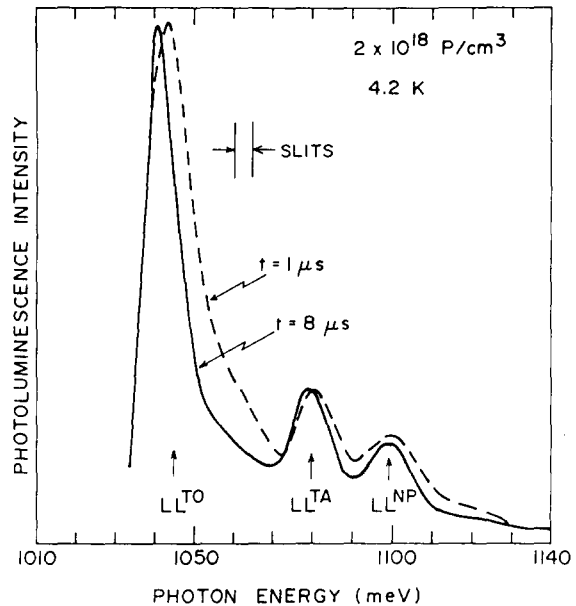


Fig. 40. Photoluminescence from electrons in the impurity band of donors at high concentration ( $2 \times 10^{18} \text{ cm}^{-3}$ ) recombining with holes in the discrete levels of a low concentration of acceptors [166].

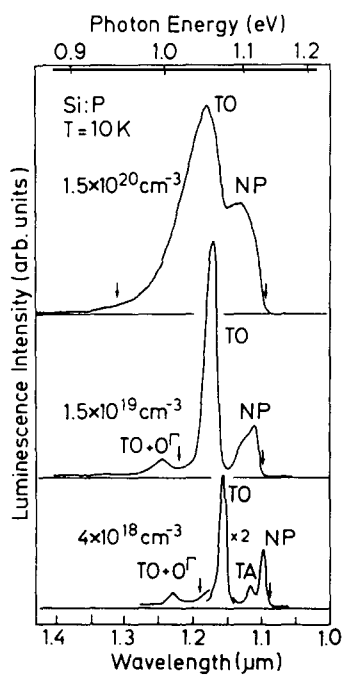


Fig. 41. Loss of photoluminescence structure in Si:P with increasing doping [89].

the luminescence shifting to lower energies with increasing time after excitation [166] (fig. 40). The radiative decay time for this luminescence ( $8.9 \mu\text{s}$  for the data of fig. 40) allows it to be saturated by excitation with  $\geq 100 \text{ mW cm}^{-2}$  visible light (for  $10^{16} \text{ cm}^{-3}$  acceptors).

Higher excitation creates an excess of holes which must occupy the valence band maximum. These free hole states are broadened into a Lifshitz tail by scattering from the donors. The loss of structure in this high concentration, high excitation regime is shown in fig. 41 for P doping up to  $10^{20} \text{ cm}^{-3}$  [89]. Data for heavy B doping are similar (but with the persistence of low zero-phonon intensity, as on fig. 34 for low concentrations). Photoluminescence excitation measurements on similar samples are reported in ref. [89]. The gross variations in the spectra resulting from recombination of free particles with particles in the impurity band in heavily doped silicon have been extensively described (e.g. ref. [167]).

## 5. Specific photoluminescence bands

### 5.1. 789 meV C-O band

The 789.4 meV band (fig. 42) is produced by room temperature radiation damage in carbon-doped Czochralski silicon [168]. Isotope substitution experiments show that the centre contains at least one carbon atom and at least one oxygen atom [169, 170]. The zero-phonon line is shifted on carbon isotope substitution (table 4). The local-mode phonon sidebands seen in photoluminescence with quanta

$$\hbar\omega_1 = 64.5 \text{ meV}, \quad \hbar\omega_2 = 72.6 \text{ meV}, \quad (61)$$

are reduced in energy by  $0.61 \pm 0.04 \text{ meV}$  and  $0.40 \pm 0.06 \text{ meV}$ , respectively, when  $^{16}\text{O}$  is replaced by  $^{18}\text{O}$  (fig. 43). No oxygen isotope effect has been detected at the zero-phonon line,\* and no C effect on the local modes: the local-mode vibrations evidently involve primarily the motion of the O atom and one Si atom whose isotope structure can also be seen in the 72.6 meV sideband (fig. 43). Quantitative details of the production of the 789 meV centre give strong evidence for only one C atom and one O atom per centre (see section 6.4). A suggestion that the zero-phonon line is broadened by the isotope effects of two Si atoms [171] is not consistent with later better resolved spectra [170].

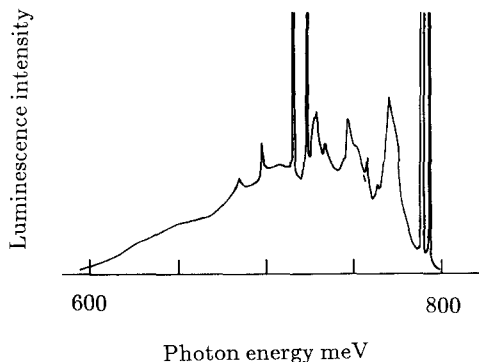


Fig. 42. Photoluminescence of the 789 meV vibronic band at 26 K [90].

\* See note added in proof.

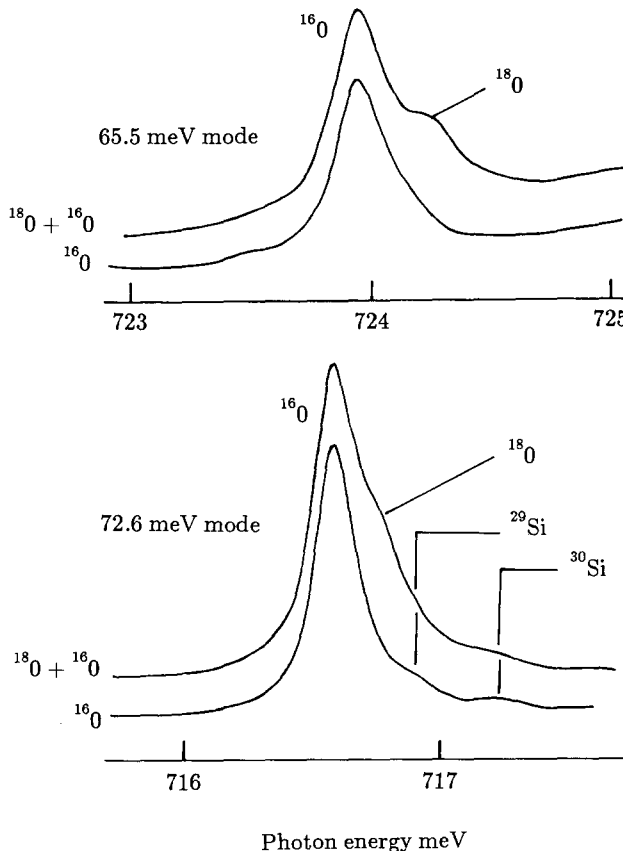


Fig. 43. Local-mode sidebands of the 789 meV photoluminescence line in samples containing either the oxygen isotope  $^{16}\text{O}$  only, or both  $^{16}\text{O} + ^{18}\text{O}$ . Note the Si isotope structure in the 72.6 meV mode [169].

The centre is formed as an interstitial carbon atom becomes mobile [172] and combines with an interstitial oxygen atom, O(i). That the O(i) atom is static has been confirmed by using uniaxial stresses to align the O(i) atoms: irradiation and annealing produces aligned 789 meV centres [173]. In silicon of high carbon and oxygen concentrations, second-neighbour pairs of C(s) and O(i) occur (section 4.1.1). Capture of a self-interstitial by the C(s)-O(i) pair is sufficient to generate some 789 meV centres [174].

Uniaxial stress perturbations [175-177] show that the centre has a monoclinic I symmetry ( $C_{1h}$  or  $C_2$  point group). However, the energy shifts produced by the stresses are dominated by stresses along the cube axes, suggesting that the 789 meV centre is almost tetragonal, weakly perturbed to monoclinic I. This is confirmed by the infra-red active modes of the centre, as discussed below.

A series of excited states can be observed in the photoluminescence spectrum [90, 175]. Using photoluminescence excitation spectroscopy at least nine clearly resolved excited states are seen (fig. 27 [177]), formed from a tightly bound hole and an effective mass-like electron [177]. The excited state structure is the Rydberg series of the effective mass electron orbiting in the Coulomb field of the hole. By comparing the energy spacings of the higher excited states with the ideal effective mass donor levels [178], Thonke et al. [177] obtained an electron binding energy of

$$E_d = 38.3 \text{ meV}. \quad (62)$$

The lower energy excited state structure (the 789 meV line itself and the first four lines to 18 meV higher energy, fig. 27) are interpreted as the 1s donor states split in the monoclinic I local symmetry of the centre (section 8).

Detailed measurements of the photoluminescence band show two local modes in addition to those of eq. (61), with quanta

$$\hbar\omega_3 = 138.1 \text{ meV}, \quad \hbar\omega_4 = 145.3 \text{ meV} \quad (63)$$

(i.e.,  $1114 \text{ cm}^{-1}$  and  $1172 \text{ cm}^{-1}$ ). Phonons observed in photoluminescence are modes in the ground electronic state of the centre, the same quanta as observed in the infra-red vibrational bands. The "C3" vibrational lines at 865.2 and  $1115.5 \text{ cm}^{-1}$  (at 77 K) and weaker vibrational lines at 529, 550 and  $742 \text{ cm}^{-1}$  all correlate in intensity with the 789 meV line (as measured in absorption) as functions of the C content, radiation dose and annealing treatment [179]. The  $1115.5 \text{ cm}^{-1}$  C3 line is apparently the  $\hbar\omega_3$  local mode and the  $529 \text{ cm}^{-1}$  line is the  $\hbar\omega_1$  local mode of eq. (61). The local-mode structure of the centre is summarised in table 2. The high degree of separation of the modes into those which are infra-red active and those which are seen in vibronic sidebands follows from the near tetragonal symmetry of the centre. Strong vibronic sidebands can only occur for modes which transform as the totally symmetric ( $A_1$ ) representation. Infra-red active modes must transform as Cartesian coordinates  $x$ ,  $y$  or  $z$ . In the  $S_4$  or  $D_{2d}$  tetragonal point groups, these coordinates transform as E and B irreducible representations. In the idealised tetragonal symmetry those modes which are allowed in the vibronic sideband are infra-red inactive and the infra-red active modes are forbidden as vibronic sidebands. Slight relaxations of these selection rules are expected if the centre is slightly distorted to a monoclinic I symmetry.

This is the first centre in silicon to be identified in both its infra-red active modes and its electronic transitions. It can also be observed [173] in paramagnetic resonance, as the "G15" or "K" transition, in the singly positive state [180] in contrast to the neutral charge state of the 789 meV centre, which is deduced from the lack of any perturbation of the line produced by magnetic fields (e.g. ref. [177]). (Suggestions [180] that the G15 centre is a carbon interstitial atom C(i) trapped at a vacancy–oxygen (VO, "A") centre disagree with all recent data.) Muller [181] has observed production of G15 centres through heat treatment at  $450^\circ\text{C}$ , when no vacancies were believed to be present. The model derived [173] recently from epr data (fig. 44) appears to satisfy all current data.

Table 2  
Local vibrational modes of the 789 meV centre

Mode energy		Observed in	
meV	$\text{cm}^{-1}$	photoluminescence	infra-red modes
64.5	520 <sup>a)</sup>	strong	weak
68	550	absent	weak
72.6	586 <sup>a)</sup>	strong	absent
92	742	absent	weak
107	865 <sup>b)</sup>	absent	strong
138.1	1114 <sup>b)</sup>	weak	strong
145.3	1172	weak	absent

<sup>a)</sup>For  $^{16}\text{O}$ . For  $^{18}\text{O}$ , 64.8 and 72.2 meV ( $523$  and  $582 \text{ cm}^{-1}$ ) [169, 170].

<sup>b)</sup>For  $^{12}\text{C}$ . For  $^{13}\text{C}$ , 104 and 134 meV ( $842$  and  $1078 \text{ cm}^{-1}$ ); for  $^{14}\text{C}$ , 102 and 130 meV ( $819$  and  $1047 \text{ cm}^{-1}$ ) [121].

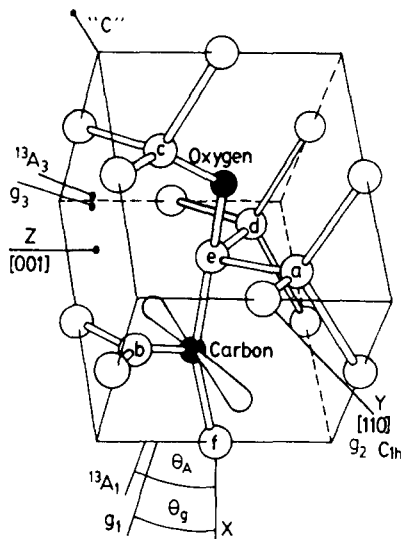


Fig. 44. Atomic model derived for the 789 meV centre from paramagnetic resonance data, and consistent with the optical data [173].

The radiative decay time of the 789 meV photoluminescence at 10 K is 200  $\mu$ s [177], decreasing through 95  $\mu$ s at 20 K [182] (fig. 21). At low temperature Thonke et al. report a very fast ( $\tau \sim 2 \mu$ s) decay process. It is possible that this is caused by the crystal not being in thermal equilibrium during a short time after pulsed laser excitation (section 3.1.2). The decay time of 200  $\mu$ s is consistent, through detailed balance arguments (section 3.2), with the observed strength of the 789 meV absorption and the concentrations of the 789 meV centres calculated using the method of section 6.4.

The 789 meV centre is thermally destroyed at temperatures  $\geq 350^\circ\text{C}$  for anneal times of about 20 minutes (e.g. ref. [179]), with an activation energy of  $1.99 \pm 0.1 \text{ eV}$  [179a]. This is consistent [173] with providing the increased strain energy of the separate C(i) and O atoms, plus the energy required to make C(i) migrate away (section 4.1.2). The 789 meV centres can also be destroyed by prolonged irradiation at room temperature. With increasing radiation dose the centres are first created and then destroyed as each 789 meV centre captures a self-interstitial to form the centre which produces the "C4" vibrational lines at  $1020 \text{ cm}^{-1}$ . The electronic transitions (if any) at this C4 centre are unknown. Further irradiation destroys the C4 centres as they capture more self-interstitials; the 789 meV centres thus act as nucleation points for self-interstitial precipitation. The destruction of the 789 meV centres is also observed for neutron irradiation [183] and for damage from ion implantation [184]. The dependence of 789 meV centres on radiation dose allows the carbon concentration to be measured (section 6.4).

## 5.2. 969 meV (two-carbon atom band)

The 969 meV optical band (fig. 45) is one of the most intensively studied bands in silicon. In brief, the centre consists of two carbon atoms and one unique silicon atom, it can be used as a sensitive tool for measuring the concentration of carbon in a sample, it is formed through a metastable configuration, the statistics of its formation and destruction are known, and its absorption has been accurately linked to its concentration.

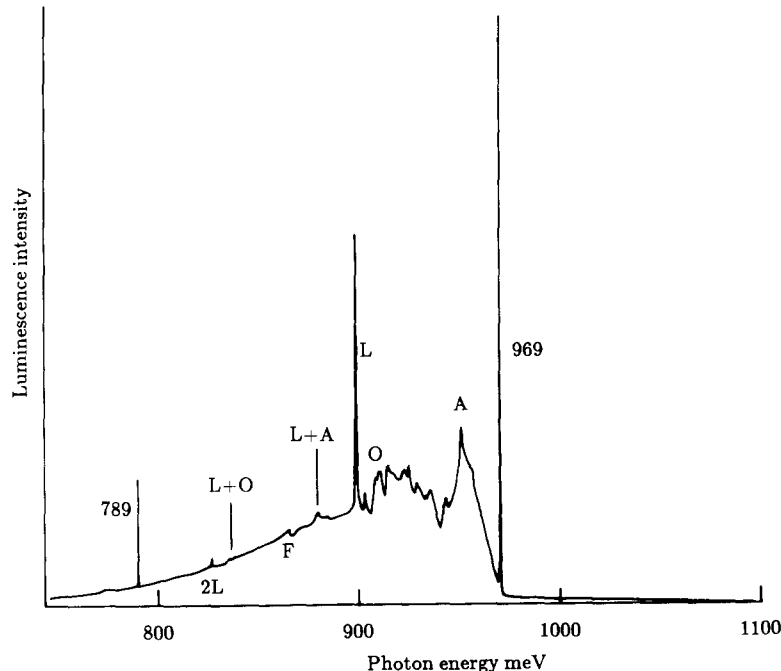


Fig. 45. Photoluminescence from float-zone silicon with  $[C] = 9.7 \times 10^{16} \text{ cm}^{-3}$  after irradiation at 200 K with  $2 \times 10^{17} \text{ cm}^{-2}$  2 MeV electrons and annealing at 325 K for 3 hours. Note the absence of the lines discussed in section 9.1. (E.C. Lightowlers, private communication 1988). Feature "A" is the transverse acoustic X point phonon, with quantum  $19.06 \pm 0.05 \text{ meV}$ .

### 5.2.1. Formation

The centre is produced by combining a mobile interstitial carbon atom C(i) with a static substitutional carbon atom C(s), section 6.4. The C(i) may originate from radiation damage, when a silicon interstitial displaces a C(s) atom (section 6.4); or by injection of a C(i) atom from outside the crystal, e.g. from a  $\text{CF}_4$  plasma [4]. Either way the C(i) atom is appreciably mobile at  $T \geq 300 \text{ K}$  (section 4.1.2) and may be captured by a C(s) atom. However, the 969 meV centre is *not* formed immediately upon capture. Figure 46 shows the decay of the C(i) atoms during annealing, and the "delayed growth" of the 969 meV band. Similar data are given in ref. [122]. The immediate product of trapping C(i) at C(s) is evidently an intermediate species denoted (CC) here which evolves to the 969 meV centre by an atomic rearrangement,



If the C(i) atoms are trapped predominantly by a large concentration of C(s) atoms, as can be arranged in lightly irradiated float-zone silicon in which the dominant impurity is carbon, the concentration  $[\text{C(i)}]$  of C(i) atoms decreases with anneal time  $t$  as

$$[\text{C(i)}] = [\text{C(i)}_0] \exp(-t/\tau_a), \quad (65)$$

where the decay time  $\tau_a$  has been shown to be inversely proportional to  $[\text{C(s)}]$  [129]. The growth of the 969 meV centres follows

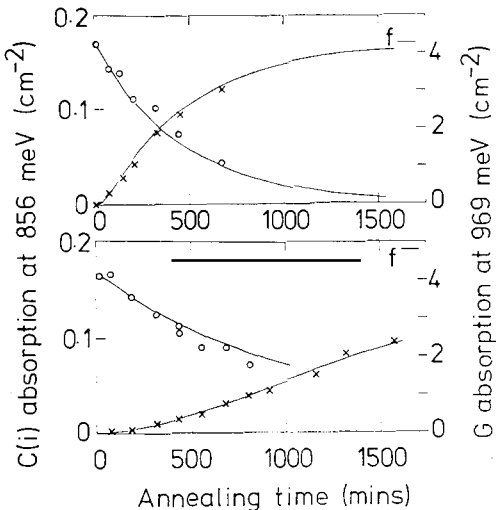


Fig. 46. Plots of the absorption in the C(i) centre (circles) and the 969 meV line (crosses) during annealing, after irradiation with  $5 \times 10^{16} \text{ cm}^{-2}$  2 MeV electrons. Top: sample with  $[C] = 5 \times 10^{16} \text{ cm}^{-3}$ , annealed at 20°C. Bottom: sample with  $[C] = 2 \times 10^{17} \text{ cm}^{-3}$ , annealed at 0°C. 'f' shows the final strength of the 969 meV line. Lines calculated with eqs. (65) and (67) [129].

$$[969] = [C(i)_0] \{ b[1 - \exp(-at)] - a[1 - \exp(-bt)] \} / (b - a), \quad (66)$$

where  $b = 1/\tau_b$  is the reciprocal of the mean time for converting a (CC) complex into a 969 meV centre, and  $a = 1/\tau_a$ .  $\tau_b$  varies exponentially with temperature  $T$  with parameters in the ranges

$$\tau_b = \tau_{b0} \exp(E_b/kT), \quad E_b = 925 \text{ to } 965 \text{ meV}, \quad \tau_{b0} = (26.3 \text{ to } 4.7) \times 10^{-13} \text{ s}. \quad (67)$$

If the (CC) complex makes a one-step rearrangement of its carbon atoms to form the 969 meV centre,  $\tau_{b0}$  should be of the order of the time period of C atom vibrations. For the isolated C(i) atom, vibrational quanta are observed at 921 and  $930 \text{ cm}^{-1}$  (section 4.1.2), giving  $\tau_{b0} = 3.6 \times 10^{-14} \text{ s}$ , close to eq. (67).

The maximum concentration of 969 meV centres that can be generated in a crystal depends on the irradiation temperature and on the presence of other impurities. In the simplest case of float-zone silicon irradiated at 100°C the C(i) atoms form 969 meV centres during the irradiation, which then act as traps for self-interstitials, limiting the concentration of 969 meV centres to  $\sim [C(s)]/10$ , where  $[C(s)]$  is the concentration of substitutional carbon present before the irradiation. If the irradiation is carried out at 200 K so that the C(i) atoms are not mobile during the irradiation, the C(i) atoms themselves act as nucleation centres for condensations of self-interstitials. Annealing the sample at 100°C produces a maximum concentration of 969 meV centres  $\sim [C(s)]/3$ .

As long as controlled conditions are used, the strength of the 969 meV absorption (or luminescence) can be used to measure the concentration  $[C(s)]$  of carbon initially present in the silicon, allowing measurement of  $[C(s)]$  down to  $\sim 10^{14} \text{ cm}^{-3}$ , an order of magnitude better than the standard methods (section 4.1.1). Weber et al. [4] have shown that if the C(i) atoms are introduced from outside the crystal, the 969 meV luminescence intensity saturates at a value proportional to  $[C(s)]$ .

### 5.2.2. Structure

A close pair of two C atoms can exist in the unknown metastable form (CC) of eq. (64) and in the structures described below which are observed in ODMR and EPR. These latter two forms also exhibit bistability [185].

The 969 meV centre is often said to occur at the C(s)-I-C(s) structure shown in fig. 47, left. This structure is observed in ODMR measurements [186] when the centre has been excited to a *triplet* spin state. In contrast the 969 meV optical transition involves spin *singlet* states [187]. A second relevant structure has been derived [188] from epr measurements on the positive charge state of the centre (figure 47, right). Here the split interstitial configuration of the C(i) atom is preserved.

Uniaxial stress perturbations show that the symmetry of the 969 meV centre is monoclinic I ( $C_{1h}$  point group) with the reflection plane perpendicular to a  $\langle 110 \rangle$  axis [187, 189, 190]. Evidence for one unique silicon atom comes from the silicon isotope structure in the zero-phonon line (fig. 48 [187, 191]). Carbon isotope substitution changes the quanta of the two local-mode sidebands seen in the 969 meV luminescence band with quanta in  $^{12}\text{C}$ -doped silicon of

$$\hbar\omega_s = 71.90 \text{ meV}, \quad \hbar\omega_w = 67.35 \text{ meV}. \quad (68)$$

In silicon doped with both  $^{12}\text{C}$  and  $^{13}\text{C}$  they become [254]

$$\hbar\omega_s = 71.82 \text{ and } 70.05 \text{ meV}, \quad \hbar\omega_w = 67.36 \text{ and } 66.04 \text{ meV}. \quad (69)$$

These data establish that in these modes one C atom is primarily involved in the motion with the second C atom producing a small effect [191]. For the strongly observed  $\hbar\omega_s$  mode the ratio of the frequencies in eq. (69) is  $71.82/70.05 = 1.025$ , close to the value of 1.028 which is expected for the ratio of the quanta produced by the reduced masses of a C-Si pair when  $^{12}\text{C}$  is replaced by  $^{13}\text{C}$ . The intensity of the  $\hbar\omega_s$  local mode relative to the zero-phonon line is [91]

$$S = I(\hbar\omega_s)/I(\text{zpl}) = 0.15 \pm 0.01. \quad (70)$$

The shift in equilibrium position  $Q_0$  of a harmonic mode is given by matching the relaxation energy to the potential energy (section 7.1),

$$S\hbar\omega_s = \frac{1}{2}m\omega^2 Q_0^2, \quad (71)$$

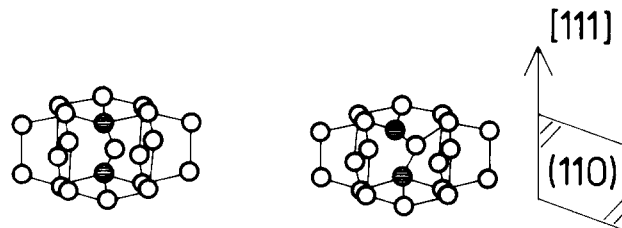


Fig. 47. Possible models for the di-carbon centre, with C atoms shown shaded. Left: model of the centre as deduced from ODMR data (for the centre in its triplet state) [186]; right: asymmetric structure proposed for the centre in its single positive charge state with one C and the unique Si atom in a (110) plane [188].

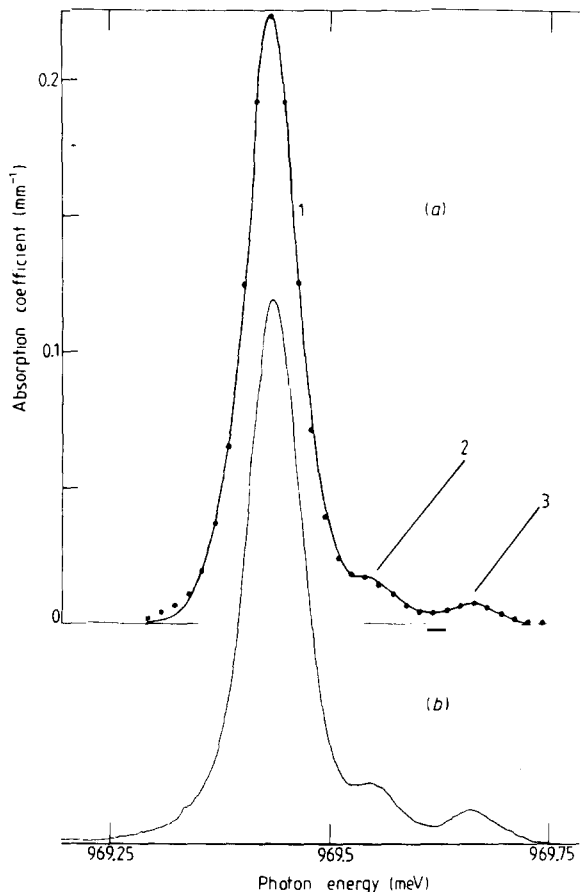


Fig. 48. (a) Absorption and (b) photoluminescence of the 969 meV zero-phonon line. Peaks 1, 2, 3 have relative intensities equal to the  $^{28}\text{Si}$ ,  $^{29}\text{Si}$ ,  $^{30}\text{Si}$  natural isotopes (eq. 1) as calculated (dotted curve) [191].

giving (when  $m$  equals the reduced mass of a C-Si "molecule")

$$Q_0 = 0.0046 \text{ nm}, \quad (72)$$

equivalent to 2% of the Si-Si bond length. There is no major difference in the atomic position of the C atom in the two electronic states of the 969 meV transition. Since the  $\hbar\omega_s$  mode must transform as the totally symmetric representation of the  $C_{1h}$  point group, this small motion  $Q_0$  is confined to lie in the reflection plane of the centre. The small structural difference between the electronic states is supported by the near mirror images of the 969 meV luminescence and absorption bands (figs. 45 and 49). Further, the total absorption in the vibronic band is constant over at least the range  $0 < T < 200$  K. No structural changes appear to occur in the electronic states involved in the optical transition, in contrast to the rotations seen in ODMR at  $T \geq 30$  K.

The evidence from the optical spectra favours an asymmetric structure like that observed in epr (fig 47, right) rather than the ODMR structure of fig 47, left.

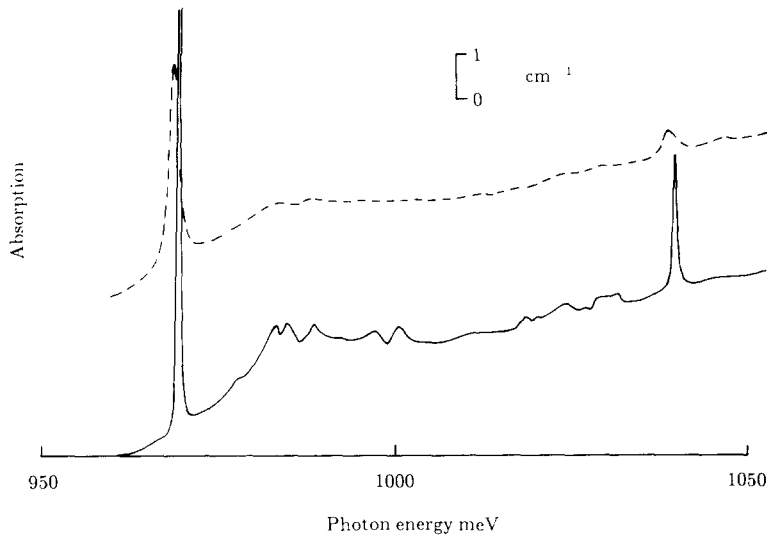


Fig. 49. Absorption at 2 K (solid line) and 77 K (broken line) in the 969 meV band measured in Czochralski silicon grown in a magnetic field, with  $[C] \sim 10^{18} \text{ cm}^{-3}$  after irradiation at  $100^\circ\text{C}$  with  $10^{18} \text{ cm}^{-2} 2 \text{ MeV}$  electrons [91].

### 5.2.3. Oscillator strength

One 969 meV centre is formed when one C(i) is trapped at a C(s) atom (eq. 64). Consequently if irradiated float-zone silicon is annealed so that each C(i) atom is converted to a 969 meV centre, the loss of C(i) atoms, which can be measured optically (section 4.2.1), gives the concentration [969] of 969 meV centres. The link between the absorption in the 969 meV line and [969] (in  $\text{cm}^{-3}$ ) is

$$\int d\nu A(\nu) = 7.0 \times 10^{-16} [\text{969}], \quad (73)$$

where  $A(\nu)$  is the absorption coefficient in  $\text{cm}^{-1}$  measured with the sample at 2 K and illuminated by white light, and the integral is over the extent of the zero-phonon line, the photon wavenumber  $\nu$  being in  $\text{cm}^{-1}$  [129]. The absorption per centre is relatively strong for silicon (table 1). Equation (73) is verified by models of the radiation-induced reactions (section 6.4). It is also consistent with detailed balance arguments (section 3.2) using the decay time of  $\sim 4 \mu\text{s}$ , as measured at the limit of the available equipment [182].

### 5.2.4. Destruction of the 969 meV centre by annealing

The centre is destroyed by annealing at  $T > 250^\circ\text{C}$  for 20 minutes. In samples which have been doped with lithium and then lightly irradiated, a Li–C complex is formed simultaneously with the annealing-out of the 969 meV centres, suggesting that the destruction occurs with one C atom being liberated from the centre (section 5.3). With increasing radiation dose the 969 meV centres capture self-interstitials I (section 5.2.1). These may break up on annealing, releasing I's into the lattice. If the silicon has been irradiated to produce less than the maximum possible 969 meV absorption, capture of I by substitutional C may lead to the formation of more 969 meV centres, as observed [194]. In more heavily irradiated samples, with fewer surviving substitutional C atoms, any I's released may be captured at the 969 meV

centres, destroying them. The details of the annealing have not been investigated. Available data (from heavily irradiated silicon) give the activation energy for thermal destruction as 1.34 eV [192] and  $1.25 \pm 0.01$  eV [193], but it is not clear what process is occurring.

### 5.2.5. Other aspects

The vibronic properties of the 969 meV centre are discussed in section 7; centres closely related to the 969 meV centre are discussed in section 9.1.

### 5.3. 1014 meV Cu band

Transition metal atoms have very high diffusion coefficients  $D$  through silicon [195]. For example, at  $900^\circ\text{C}$ ,  $D \sim 5 \times 10^{-5} \text{ cm}^2/\text{s}$  for copper, over seven orders of magnitude greater than for oxygen (eq. 54). The transition metals may occupy substitutional or interstitial sites [196]. The best established photoluminescence from a transition metal is that from copper (fig. 50). The vibronic sideband has phonons of quanta 7.0, 16.4 and 25.1 meV [197–200]; the step in the phonon sideband near 955 meV indicates TO lattice modes also. The band is frequently observed after silicon has been heated at  $\sim 700^\circ\text{C}$  in the presence of copper (e.g. in a furnace contaminated by the heating element). Rapid quenching of the sample enhances the band [199, 200], presumably by trapping the Cu atoms as single atoms or very small clusters. Implantation of  $^{63}\text{Cu}$  or  $^{65}\text{Cu}$  into silicon produces an isotope shift of the zero-phonon line, confirming that the centre involves copper [200]. The number of Cu atoms per centre is not certain. (Silicon has not been simultaneously implanted with both Cu isotopes.) The luminescence intensity is proportional to the square of the total Cu concentration at the heating temperature [200], but it is unlikely that all the copper is in the luminescent form.

Uniaxial stress data [200] show the 1014 meV transition to be between a ground orbital singlet and an excited orbital doublet state at a trigonal centre.

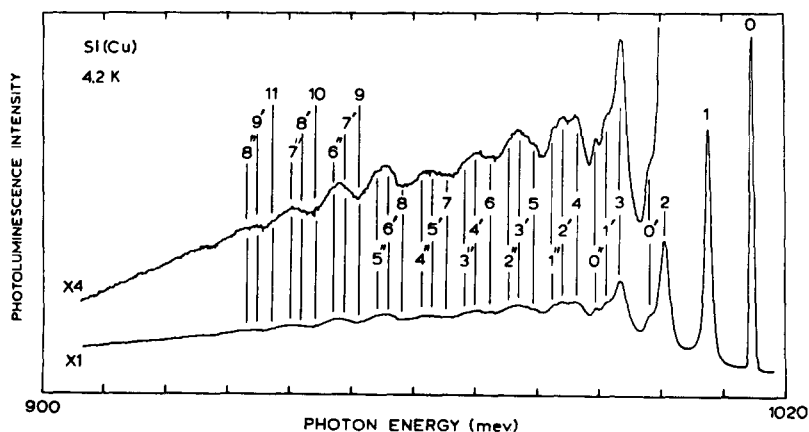


Fig. 50. Photoluminescence at 4.2 K of the 1014 meV Cu-related band. The individual phonon progressions are denoted  $0, 1, 2, \dots, 0', 1', 2', \dots$ , etc. [199]. In addition there is an optic-mode sideband at  $\sim 57$  meV.

### 5.4. 1018 meV W or I1 band

The 1018.2 meV band (fig. 51) is created by radiation damage, especially by bombardment with neutrons or ions. It is frequently observed in studies of the effects of radiation damage in silicon (e.g. ref. [192]), recombination radiation from ion-implanted silicon [184], neutron transmutation of silicon [201] and laser annealing of ion implantation damage [6]. However, the precise method of creating the 1018 meV centre is not known. It is not produced immediately after neutron irradiation if the samples are immersed in a water enclosure at less than 45°C during the irradiation [202]. Annealing at 525 K for 30 min is then necessary to maximise the intensity of the W line. This suggests that the defects forming the 1018 meV centre have migrated away from the immediate region of damage, consistent with the width of the zero-phonon line being independent of the irradiation dose (section 10.1). The W band is unaffected by changing the carbon isotope [203] and is not known to depend on the presence of any other impurity in the crystal. The one local mode frequency observed in luminescence shows isotope effects consistent with vibrations of only Si atoms (fig. 51). Modified versions of the 1018 meV band are created when the silicon is bombarded with He, Ne, Ar, Kr or Xe ions (section 9.2).

Magnetic field perturbations produce no detectable effect on the 1018 meV line, implying that it occurs between spinless states [202, 203]. Uniaxial stress perturbations establish it as an electric dipole

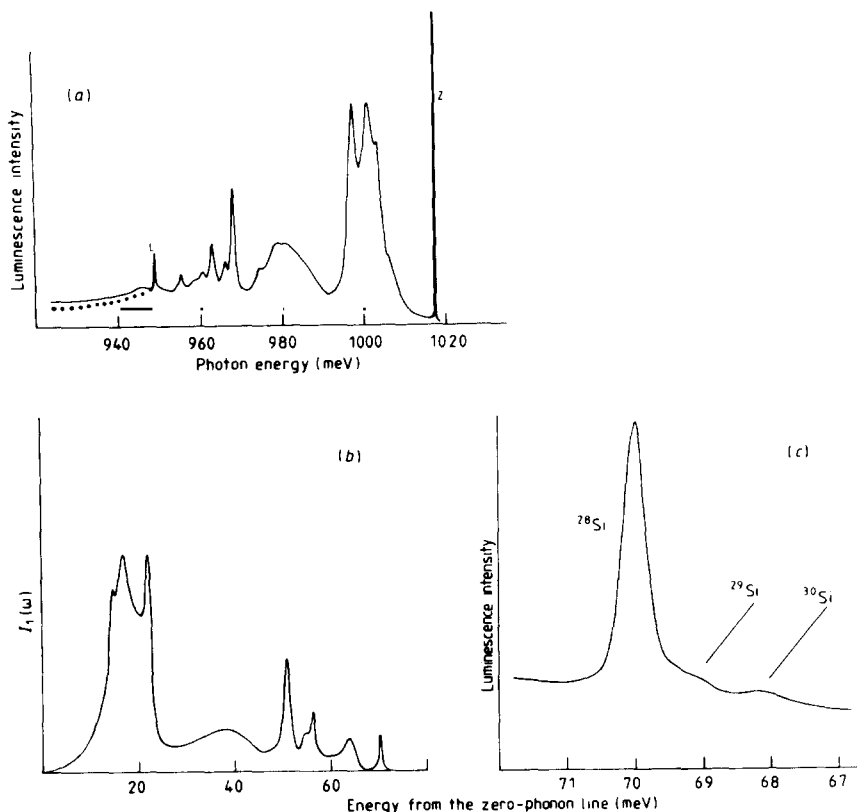


Fig. 51. (a) Measured photoluminescence of the 1018 meV band at 2 K, (b) the one-phonon contribution and (c) the 70 meV local mode labelled I on (a). This mode is composed of  $^{28}\text{Si}$ ,  $^{29}\text{Si}$  and  $^{30}\text{Si}$  peaks as shown [202]. In (a) the points show where the reconstruction, calculated as in section 7.1, deviates from the measured spectrum.

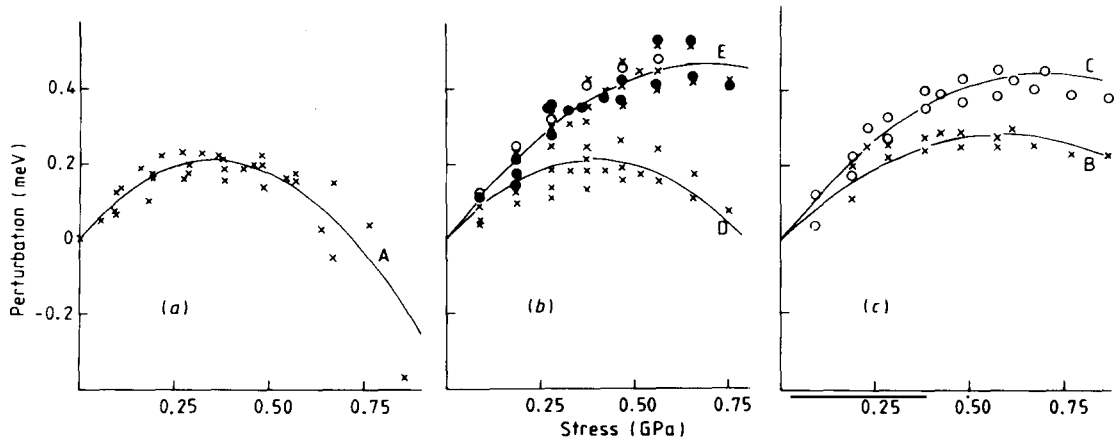


Fig. 52. Perturbations of the 1018 meV line under (a)  $\langle 001 \rangle$ , (b)  $\langle 110 \rangle$  and (c)  $\langle 111 \rangle$  uniaxial compressions. The lines are calculated for a transition between non-degenerate states at a trigonal centre when the excited state interacts with non-degenerate and doubly degenerate states  $\sim 30$  meV higher [202].

transition between two orbitally non-degenerate states at a trigonal centre [202–204] (and not a magnetic dipole transition [205]). Stress perturbations of the 1018 meV line produce *highly* non-linear shift rates (fig. 52) as the excited state of the transition interacts with higher lying non-degenerate *and* doubly degenerate orbital states [202]. There are no observable changes in the intensities of the lines arising from the interaction. Absorption into the higher states has not been detected, and so it is not possible to carry out a rigorous analysis of the interaction. To fit the curvature of the shift rates but produce no intensity changes, the higher lying states must be 30 to 40 meV above the excited state of the 1018 meV line.

The vibronic sideband has an intensity, relative to the zero-phonon line, corresponding to a Huang–Rhys factor (section 7.1) in the limit of low temperature of

$$S = 0.9 \pm 0.1 . \quad (74)$$

This value can be calculated from the uniaxial stress data if the 1018 meV centre is harder to compress than the bulk lattice (section 7.2), consistent with the high vibrational frequency of the silicon atom observed in the vibronic sideband (fig. 51). Because the stress response of the 1018 meV line is dominated by the interaction of the excited states, we might expect there to be a strong vibronic interaction leading to a “pseudo-Jahn–Teller effect”. This does not occur (section 7.4).

Annealing above 600 K produces a sharp drop in the W line’s intensity [184, 202, 203].

### 5.5. 1045 meV 4-Li atom complex

The 1045 meV (“Q” or “Li-saturated vacancy”) band is created when lithium has been diffused into silicon, and the crystal is subsequently subjected to room temperature radiation damage [206]. The zero-phonon region contains three lines ( $Q_L$ , Q and  $Q_H$  on fig. 53). Magnetic perturbations show that  $Q_L$  originates in a spin triplet state ( $S = 1$ ) [207]. Consequently  $Q_L$  has a small (spin forbidden) transition probability to the  $S = 0$  ground state of the centre and is best observed at low temperature ( $T \leq 4$  K) when its excited state, which has the lowest energy of the excited multiplet states, is

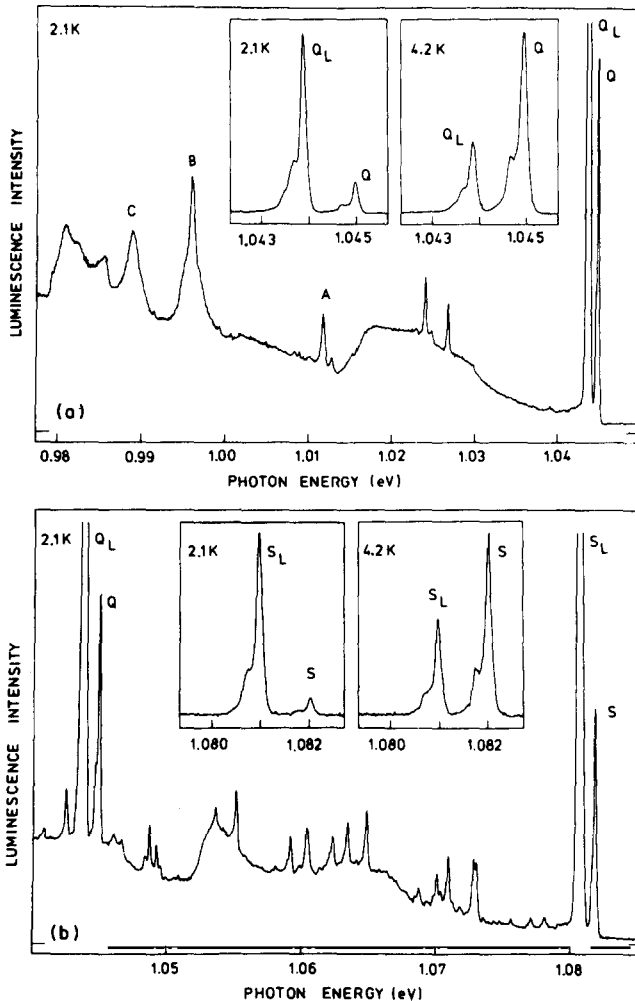


Fig. 53. Photoluminescence at 2.1 K from the 1045 meV 4-Li atom centre and the 1082 meV centre formed by adding one C atom. Insets show the temperature dependences in the zero-phonon region [211].

preferentially populated. Lines Q and  $Q_H$  (fig. 53) originate in  $S = 0$  excited states  $1.07 \pm 0.05$  meV and 4.2 meV, respectively, above  $Q_L$ . All the transitions terminate in the same electronic ground state. Consequently the ratios of the intensities of the three photoluminescence lines are given by Arrhenius plots with gradients determined by the energy separations [208]. For the Q and  $Q_L$  lines the extrapolation to infinite temperature gives

$$Q/Q_L = 45 \pm 5 \quad \text{as } T \rightarrow \infty. \quad (75)$$

This ratio and the multiplet states are explained in section 8.

Uniaxial stress perturbations [207] show that the Q and  $Q_H$  lines have excited orbital states with irreducible representations  $\Gamma_3$  and  $\Gamma_1$ , respectively, in the trigonal ( $C_{3v}$ ,  $D_{3d}$ ) point group of the centre. The ground state is also  $\Gamma_1$ . Similarly the  $Q_L$  line and a forbidden line near 1046.9 meV also have  $\Gamma_3$  and  $\Gamma_1$  excited states. Clear examples of forbidden crossings occur (fig. 54). In these forbidden

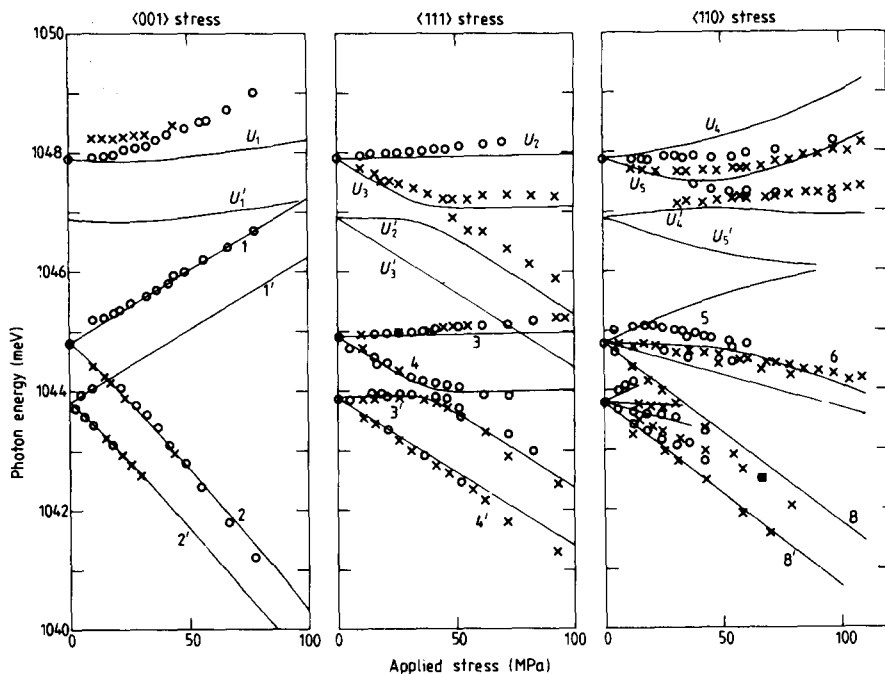


Fig. 54. Perturbations of the lines in the zero-phonon region for the 1045 meV centre under uniaxial compressions (as shown at top). The calculated lines are for transitions from a non-degenerate ground state to orbital doublets (for the 1044 and 1045 meV transitions) in a trigonal centre [207].

crossings the interacting states come close together in energy before they repel each other. Consequently there is a sudden transfer of intensity between the components, in contrast to the stress-induced interactions between states at the 1018 meV centre (section 5.4), which produce negligible transfer of intensity. The sudden onset of the interactions at the 1045 meV centre is caused by the relatively small mixing terms in the perturbation. This is partly because the spins of the interacting states are in each case different, and also because the interacting states occur at *different orientations* of the trigonal centres. Evidently the electronic states overlap between the different orientations of the centre. (A similar situation has been reported for other semiconductors [209].)

Detailed isotope doping experiments, with different ratios of the concentrations of <sup>6</sup>Li and <sup>7</sup>Li, unambiguously establish the presence of Li in the centre [210]. There are four Li atoms per centre—the largest number of impurity atoms observed to date in a defect in silicon. The isotope data are simpler for the Q<sub>L</sub> line than for Q (fig. 2). There are five ways of combining <sup>6</sup>Li and <sup>7</sup>Li atoms in a 4-Li atom centre, each combination having a relative probability given by the number of ways of randomly choosing <sup>6</sup>Li and <sup>7</sup>Li atoms. Ignoring the shoulders on the sides of the lines 2 and 3 on fig. 2, this distribution fits the relative intensities of the isotope peaks for the Q<sub>L</sub> line, the peaks 1 to 5 being produced by 0 to 4 Li atoms. The energy of the Q line is sensitive to the positions of the <sup>6</sup>Li and <sup>7</sup>Li atoms within the trigonal complex. A trigonal centre of 4 Li atoms can be formed from a tetrahedral complex by a radial displacement of one atom. If a <sup>6</sup>Li atom occupies this unique site, the energy of the resulting transition is evidently higher than if it is occupied by a <sup>7</sup>Li atom. For example, when there is one <sup>6</sup>Li atom per centre (lines 2 and 2' on fig. 2), there is a random probability of 1/4 for that <sup>6</sup>Li atom being in the unique site, and 3/4 for it to be in the basal triangle. The intensity of line 2 relative to that of 2' is therefore expected to be 1:3, as appears to be observed (fig. 2). The difference between the lines Q and Q<sub>L</sub> regarding this subsplitting is not known.

The ratios of the isotope substructure are different when measured in absorption and luminescence. The energy spacing of the substructure (e.g. for lines 2 and 2') is  $\sim 0.1$  meV, equivalent to 1 K. In luminescence the higher energy component (e.g. 2) is weaker, relative to the lower energy component (2'), than when measured in absorption. This is consistent with a re-orientation of the centre occurring in the excited state favouring the lower energy transitions.

The forbidden crossings in the stress data and the isotope substructure both show that the centre can re-orient easily, implying that the trigonal symmetry arises from the centre being slightly perturbed from a tetrahedral complex. The electronic structure of the centre is discussed further in section 8, the isotope structure in section 7.5 and the vibronic properties in section 7.1.

The radiative decay time of the 1045 meV Q line is  $9.5\ \mu\text{s}$  and that of  $Q_L$   $3600\ \mu\text{s}$  [211]. The measured decay time therefore contains two components arising from the relative populations of the excited states of Q and  $Q_L$ , and also the common fast decrease above  $\sim 30$  K (section 3.1.1). Using detailed balance arguments (section 3.2), only a few percent of the Li in the silicon is converted to 1045 meV centres, in float-zone samples irradiated to create a concentration of vacancies similar to the concentration of Li: the 1045 meV band cannot be used to measure quantitatively the Li concentration.

The 1045 meV centre is destroyed by thermal annealing at  $400^\circ\text{C}$ .

If the 1045 meV band is created by irradiating silicon which contains carbon as well as lithium, the 969 meV centre is also produced (section 5.2). The 969 meV centre is unstable at temperatures above  $\sim 300^\circ\text{C}$ , less than the breakup temperature ( $400^\circ\text{C}$ ) of the 1045 meV centre. As the silicon is heated, a new centre with its zero-phonon line at 1082 meV is created matching the destruction of the 969 meV line (fig. 53) [211]. It is apparently a 1045 meV band plus a carbon atom. This new band has properties very similar to those of the 1045 meV band [211]. For example, it shows triplet/singlet structure equivalent to  $Q_L$  and Q, a line  $S_H$  equivalent to  $Q_H$  (plus an extra line  $S^*$ ) and has a similar radiative decay time. It is also destroyed near  $400^\circ\text{C}$ .

## 6. Radiation-induced photoluminescence centres

Radiation damage processes are very important in creating photoluminescence centres. Irradiation with high energy electrons is understood in quantitative detail and so is emphasised here. The mechanism of producing damage by electrons is outlined in sections 6.1 and 6.2, the effects of carbon are discussed in detail in sections 6.3 to 6.5, “subthreshold damage” is discussed in section 6.6 and finally the effects of producing radiation damage by other particles are described in section 6.7.

### 6.1. Rate of primary atomic displacements by electrons

The radiation damage process may be broken into stages. First, enough energy must be given to an atom of silicon that it is displaced from its lattice site through a sufficient distance that the bonds pulling the atom back into its lattice site are broken. The second stage of producing “permanent” damage is that the displaced atom must not undergo correlated recombination with the vacancy (i.e., the atom should not simply “fall back” into its original site); this is discussed in section 6.2. We take the primary displacement process first.

The range  $R$  (in  $\text{mg}/\text{cm}^2$ ) of an electron of kinetic energy  $E$  (in MeV) can be approximated by the Katz and Penfold equation,

$$\ln(R) = (1.265 - 0.0954 \ln E) \ln E + \ln(412), \quad \text{valid for } E \leq 2.5 \text{ MeV}. \quad (76)$$

For example, for 2 MeV electrons  $R = 4.06$  mm. For electrons of higher energy Feather's rule gives

$$R = 530E - 106, \quad E > 2.5 \text{ MeV}. \quad (77)$$

Spectroscopic measurements on silicon are conveniently carried out on slices 2 mm thick. For comparison with the experimental data below we take the specific case of irradiation with 2 MeV electrons. From eq. (76) an electron which enters a 2 mm slice with 2 MeV will emerge at the back face with 1.13 MeV.

For electrons of these energies the rate of creation of damage is independent of the crystallographic direction of the irradiation, to within 20% [212, 213]. It is then adequate to assume that an atom is definitely displaced if it receives more than an isotropic displacement energy  $E_d$  and is not displaced otherwise.  $E_d$  defined in this way is a parameter used to estimate the rate of primary atomic displacements by electrons with kinetic energies in the MeV range; it need not have significance in terms of atomic bonding. Because the production of stable radiation damage requires the separation of the primary vacancy and interstitial, the rate of production of primary displacements is not measured directly.  $E_d$  is obtained by measuring the dependence of the rate of production of observed end products on the energy of the incident electrons, giving [214–216]

$$E_d = 20 \text{ to } 25 \text{ eV}, \quad \text{valid for electrons of } E \geq 1 \text{ MeV}, \quad (78)$$

which would correspond to irradiation with electrons of kinetic energy  $E_t = 340$  keV, below the range at which  $E_d$  is valid.

Photoluminescence has been used to measure directly the threshold energy  $E_t$  from the intensity of the radiation-induced 969 meV band (section 4.1.2), giving [217]

$$E_t = 145 \text{ keV}. \quad (79)$$

Above the threshold there is a very rapid increase of production of 969 meV centres with increasing electron energy, the most rapid part of the rise being centred on 300 keV. The threshold determined from changes in electrical conductivity is 200 keV, similar to eq. (79) [218].

An individual damage event may result in more than one vacancy-interstitial pair being produced if a displaced atom hits another atom and both depart from the locality with kinetic energies greater than their displacement energies. However, for 2 MeV electron irradiation, divacancy production is about an order of magnitude less than isolated vacancy production (e.g. ref. [213]). For typical electron energies (1 to 2 MeV) and using  $E_d = 25$  eV the cross-section for atomic displacement is given by the standard theory [219] as ( $\sim 33$  to  $41$ )  $\times 10^{-24}$  cm $^2$ . The rate of creating primary displacements is calculated to be

$$dn/d\phi = 2.05 \text{ cm}^{-1} \quad (80a)$$

at the front face of a silicon slice under 2 MeV bombardment, and

$$dn/d\phi = 1.75 \text{ cm}^{-1} \quad (80b)$$

at the back face of the slice when the electron energy is 1.13 MeV. The variation can be reduced to less than  $\pm 1\%$  from the mean by irradiating the sample equally from both sides. Note that at low radiation doses the individual damage events are well separated on the atomic scale.

## 6.2. Rate of production of observable damage

When an atom is given an energy  $E_r$  by impact from an electron, it leaves its site with a kinetic energy  $E_r - E_d$ . This energy is dissipated by collisions with lattice atoms. The details of the energy loss are dependent on the orientation of the crystal relative to the electron beam. Assuming an isotropic situation, and that each collision halves the energy of the moving atom, the remaining kinetic energy after  $n$  collisions is  $(E_r - E_d)/2^n$ . When this is less than the barrier  $E_c$  to migration, the interstitial atom will be trapped. Assuming  $E_c = 1\text{ eV}$ , the mean value of  $n$  is  $\langle n \rangle = 4.7$  for irradiation with 2 MeV electrons. If the vacancy and interstitial have opposite charge states (which is likely since their electronic energy levels are unlikely to be coincident), their Coulomb attraction is  $\sim 120\text{ meV}$  at  $\langle n \rangle$  interatomic separations. Correlated recombination (when the self-interstitial moves back to its original lattice site) is then highly likely for most of the primary displacements, and will increase as the temperature decreases.

The rate of production of vacancies (measured by epr) during irradiation with 1.5 MeV electrons at 20 K is a function of the Fermi energy [220] (fig. 55). In p-type silicon, self-interstitials created by the damage can migrate from the vacancies and are permanently removed by reaction with the p-type dopants [221]. The rate of producing vacancies at 20 K is  $0.03\text{ cm}^{-1}$  [221] in Al-doped silicon, not much less than at room temperature [ $\sim 0.13\text{ cm}^{-1}$ , eq. (81) below].

With increasing radiation dose the initial position of the Fermi energy is irrelevant. In Czochralski silicon mobile vacancies are captured at oxygen impurity atoms. Rearrangement of a metastable V-O pair leads to the formation of the "A centre" characterised optically by vibrational absorption lines at  $836$  and  $884\text{ cm}^{-1}$ . If there are no other traps (e.g. from P or Sn impurities) for the vacancies, the rate of production of A centres equals that of separated vacancy-interstitial pairs.

Figure 56 shows the temperature dependence of the production of  $836\text{ cm}^{-1}$  absorption in silicon which is initially n-type but is being irradiated with large enough doses that the damage centres will dominate [222]. Between 75 and 90 K there is a thermally activated rate of production of vacancy-oxygen pairs with an activation energy of 50 meV. At higher temperatures of irradiation the production

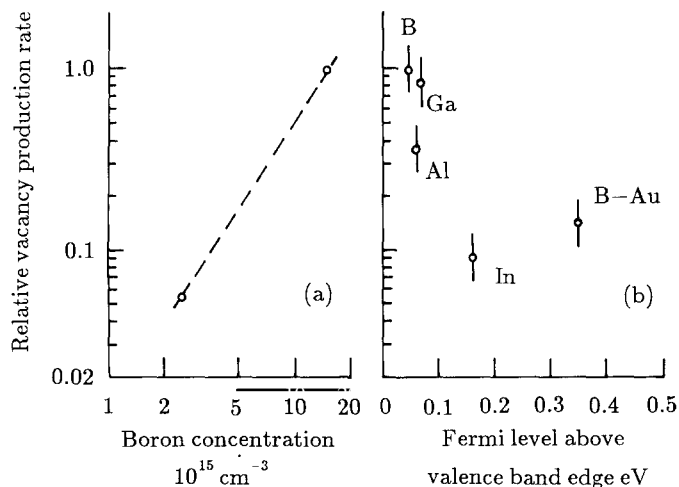


Fig. 55. Relative production rate of vacancies in p-type silicon as functions of (a) the boron concentration, and (b) the position of the Fermi energy [220].

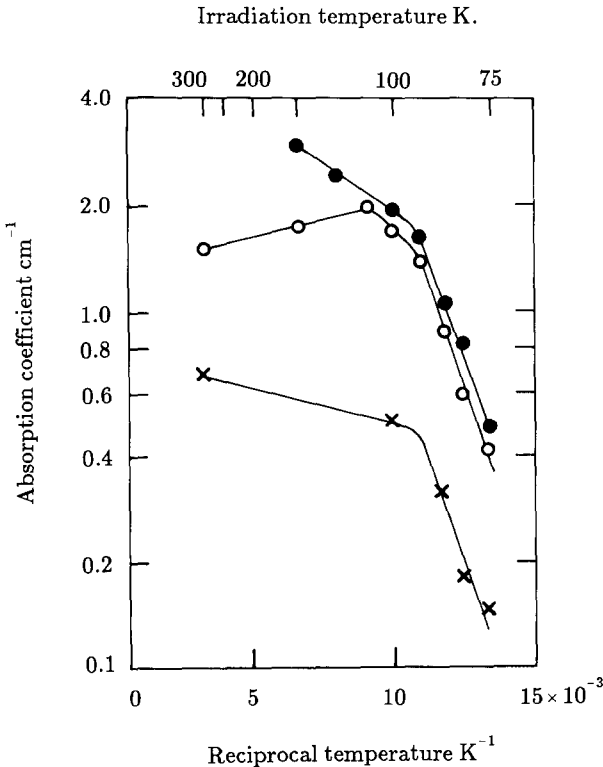


Fig. 56. Peak absorption coefficients of radiation-induced lines after irradiation with  $10^{18} \text{ cm}^{-2}$  2 MeV electrons as functions of irradiation temperature. The line at  $836 \text{ cm}^{-1}$  (filled and open circles) occurs at V-O, and the  $865 \text{ cm}^{-1}$  line (crosses) at the 789 meV C(i)-O centre [222] after annealing at 100°C. The data are only qualitative because of the high radiation doses, which will have produced self-interstitial clusters.

rate saturates, and is shown below to become constant above 220 K [223]. The activation energy is verified [222] by the behaviour of the  $922$  and  $932 \text{ cm}^{-1}$  lines, now known to occur at interstitial carbon C(i) (section 4.1.2). Again the production rate of the C(i) atoms is constant over 200 K [224]. The data of fig. 56 can be parameterised by the plot of fig. 57 showing the energy of the crystal as a function of the separation of the vacancy and self-interstitial. The activation energy (50 meV) is the difference  $E_b - E_a$ , so that the probabilities of correlated recombination and vacancy–interstitial separation are in the ratio  $\exp[(E_b - E_a)/kT]$ .

These temperature dependence studies should be repeated for two reasons. First, aggregates of self-interstitials occur on C(i) atoms as the radiation dose increases (section 6.3), reducing the concentration of isolated C(i) atoms able to absorb at  $922$  and  $932 \text{ cm}^{-1}$ . The samples in fig. 56 were given doses of  $10^{18} \text{ cm}^{-2}$  2 MeV electrons, a considerable dose. Second, we can now relate the measured absorption coefficients to the concentrations of the vacancy–oxygen A centre and the C(i) atoms, allowing the work to become more quantitative.

Above  $T \approx 200 \text{ K}$  the production rate of isolated vacancies and self-interstitials is essentially independent of  $T$  [223]. The introduction rates of the vacancy–oxygen A centre under 2 MeV electron irradiation at room temperature measured by a large variety of techniques are all in agreement (within a spread of  $\sim 50\%$ ) at [9, 225–227]

$$\frac{dn}{d\phi} = 0.133 \text{ cm}^{-1} \quad (81)$$

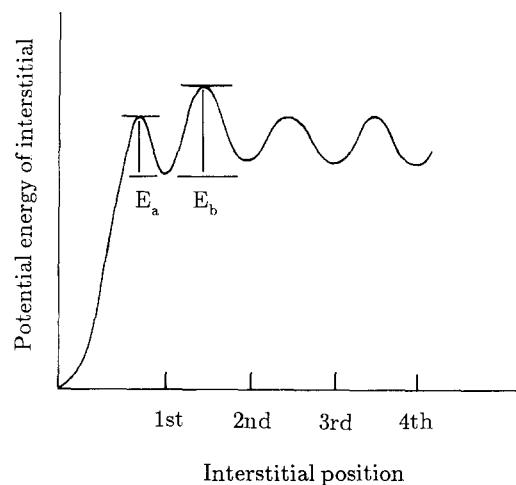


Fig. 57. Schematic plot of the potential energy of a self-interstitial as a function of distance from the vacancy. Local trapping at the "first" position produces the temperature dependence of fig. 56 [222].

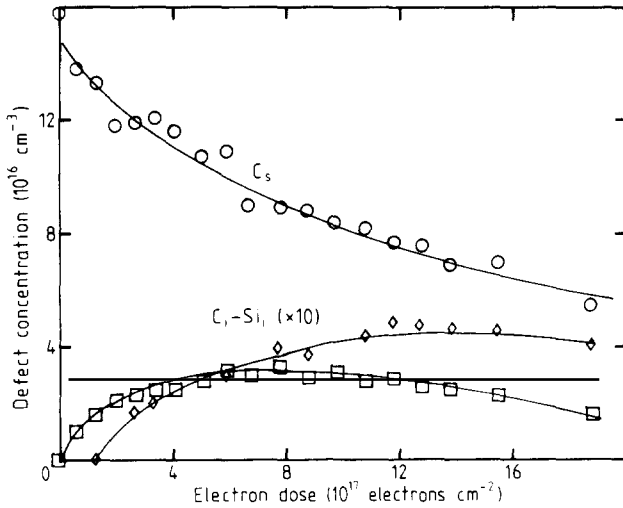


Fig. 58. Concentration of substitutional carbon C(s) in silicon irradiated at 150 K with 2 MeV electrons. Squares show the concentration of C(i), obtained by matching to the initial loss of C(s). Diamonds show concentration of C(i) + I centres, assuming the same oscillator strength as for C(i) [132].

(the value quoted being that of ref. [225]). Independent determinations of the damage rate have been made by measuring the initial rate of loss of carbon from substitutional sites as the self-interstitials displace C atoms [174]. For irradiation with 2 MeV electrons at 220 to 720 K (fig. 58)

$$dn/d\phi = 0.15 \pm 0.05 \text{ cm}^{-1}. \quad (82)$$

Comparison with eq. (80) suggests that  $\sim 90\%$  of the vacancies and interstitials created by the primary displacements are annihilated by correlated recombination before they can be observed.

### 6.3. Effects of carbon for irradiation below room temperature

The carbon interstitial C(i) becomes appreciably mobile close to room temperature (section 4.1.2). Its effect on the radiation processes depends critically on the conditions of the irradiation. For example, if a sample is irradiated to an electron dose of  $10^{17} \text{ cm}^{-2}$  at a flux of  $25 \mu\text{A cm}^{-2}$ , the time of the irradiation is 640 s. The mean capture time for a C(i) at a substitutional carbon atom C(s) when the concentration of carbon is  $5 \times 10^{16} \text{ cm}^{-2}$  is only 16 s if the sample is at  $100^\circ\text{C}$ , and is 26 000 s at  $20^\circ\text{C}$  [131]. At  $100^\circ\text{C}$  the C(i) atoms combine with the C(s) on a time scale short compared with the duration of the irradiation; the effects are discussed in section 6.4. At  $20^\circ\text{C}$  the C(i) atoms are immobile during the irradiation. Figure 58 [132] shows that during the "low temperature" irradiations the concentration of isolated C(i) atoms saturates at approximately 20% of the initial carbon concentration, and then decreases as the C(i) atoms trap mobile self-interstitials [131, 132]. The first product of the complexing



gives absorption at 959 and 966 cm<sup>-1</sup> [132]. The eventual decrease in these lines (fig. 58) shows that the IC(i) complex also traps I's, so that the C(i) atoms are probably nucleation points for precipitation of self-interstitials I.

If a sample is annealed (e.g. by simply storing it at room temperature) after irradiation at "low temperature", the C(i) atoms become mobile and complex with oxygen or substitutional carbon. In float-zone silicon with negligible oxygen the resulting 969 meV absorption is about a factor of two stronger than that obtained by irradiating at higher temperatures (e.g. 100°C), because the formation of complexes of 969 meV centres and self-interstitials is avoided (see section 6.4). The loss of C(i) atoms may be equated to the formation of 969 meV centres allowing the 969 meV absorption to be calibrated in terms of the concentration of 969 meV centres (eq. 73).

A small level of spontaneous production of 789 meV luminescence (produced by trapping a C(i) at an oxygen atom) is reported after irradiation at sample temperatures down to 100 K [172]; on annealing near room temperature the 789 meV band increases considerably and 969 meV luminescence also appears. The spontaneous production of 789 meV centres is ascribed to the presence of grown-in close pairs of carbon and oxygen, requiring little motion of some of the C(i) atoms to an oxygen atom [228].

#### 6.4. Effects of carbon during irradiation above room temperature

When the samples are irradiated at temperatures large enough for the C(i) atoms to be appreciably mobile *during* the irradiation (section 6.3), they complex with substitutional carbon and oxygen to form 969 meV and 789 meV photoluminescence centres, respectively (sections 5.2 and 5.3). The maximum 969 meV intensity occurs *in both float-zone and Czochralski silicon* at a radiation dose  $R_m$  in cm<sup>-2</sup> (for 2 MeV electrons) of

$$R_m = (2.5 \pm 0.5)[C], \quad (84)$$

where [C] is the initial concentration of carbon in cm<sup>-3</sup>. The maximum of the 789 meV line occurs at

$$R_m = (7.7 \pm 1)[C] \quad (85)$$

in samples where the oxygen content dominates the carbon [228].

At larger doses the concentrations of the centres decrease as they capture self-interstitials I. No luminescence is reported from the centre formed when I is trapped at a 789 meV centre, but its vibrational absorption is known (the "C(4)" line at 1020 cm<sup>-1</sup>). There are no identified spectra associated with the complexes of I at the 969 meV centre but a set of four photoluminescence transitions are produced, possibly caused by 969 meV centres with self-interstitials trapped nearby (section 10.1).

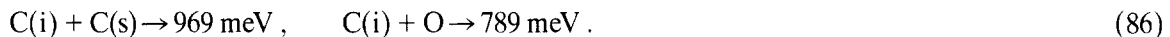
The fact that the 969 meV centres reach a maximum concentration at the same dose (for a given [C]) in both float-zone and Czochralski silicon (eq. 84) implies that at these temperatures of irradiation there is little trapping of self-interstitials at impurities (e.g. O) other than C.

#### 6.5. Quantitative aspects of room temperature irradiation

Radiation damage initiates reactions between the impurities, creating various photoluminescence centres. The sequence of the reactions depends on the temperature of the irradiation (sections 6.3 and 6.4), the impurity content and the type of damage. Attempts have been made to model the reactions by

estimating the diffusion rates of the migrating species and their capture radii at trapping points in the lattice (e.g. ref. [229]). This method fails because the temperature of the crystal may not be accurately known (e.g. during the irradiation), and the diffusion rates for some species (e.g. the self-interstitial) are not known in the conditions of interest.

A better approach is to use “branching reactions”, as follows [230, 231]. For the specific case of irradiation with 2 MeV electrons at 100°C, in silicon containing carbon and oxygen as the major impurities, a self-interstitial I displaces a substitutional C atom C(s) to give an interstitial C(i) (section 4.1.2). C(i) is mobile at 100°C, and is trapped at another C(s) or at an oxygen atom to form, respectively, the 969 meV and 789 meV centres (sections 5.2, 5.1),



If these are the only two traps for C(i) atoms, the probability of forming a 969 meV centre depends on the relative capture radii  $R$  of a C(i) atom at the two trapping points, and the relative concentrations of the traps,

$$P = R(C(i), C(s))[C(s)] / \{R(C(i), C(s))[C(s)] + R(C(i), O)[O]\}. \quad (87)$$

For a given increment of radiation dose, leading to a known increment of I's (eqs. 81, 82), the increase in concentration of 969 meV centres may be calculated, using the measured concentrations of C(s) and O, and with only one unknown variable, the ratio of the capture radii. This same parameter determines the increase in concentration of the 789 meV centres. As the radiation continues, I's are trapped at the 789 and 969 meV centres (section 6.3) in addition to being trapped at C(s) atoms. Again, equations similar to eq. (87) describe these branching reactions. The vacancy-induced processes can be described in an analogous way.

To fit the experimental data (which are the strengths of the absorption in the optical bands), the

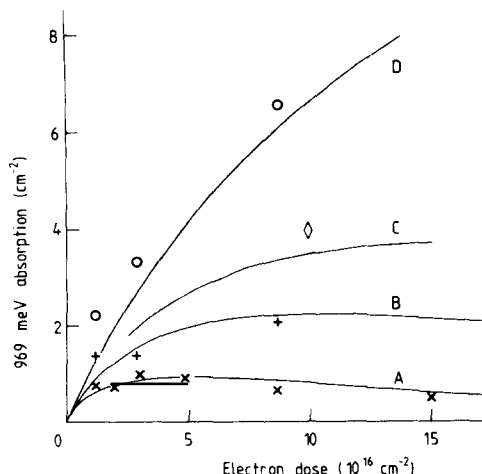


Fig. 59. Production of 969 meV zero-phonon absorption in float-zone silicon as functions of irradiation dose at 100°C with 2 MeV electrons. Samples A to D have  $[C] = 1.6 \times 10^{16}, 3.9 \times 10^{16}, 6.5 \times 10^{16}, 2 \times 10^{17} \text{ cm}^{-3}$ . Lines are calculated as in section 6.5 [211].

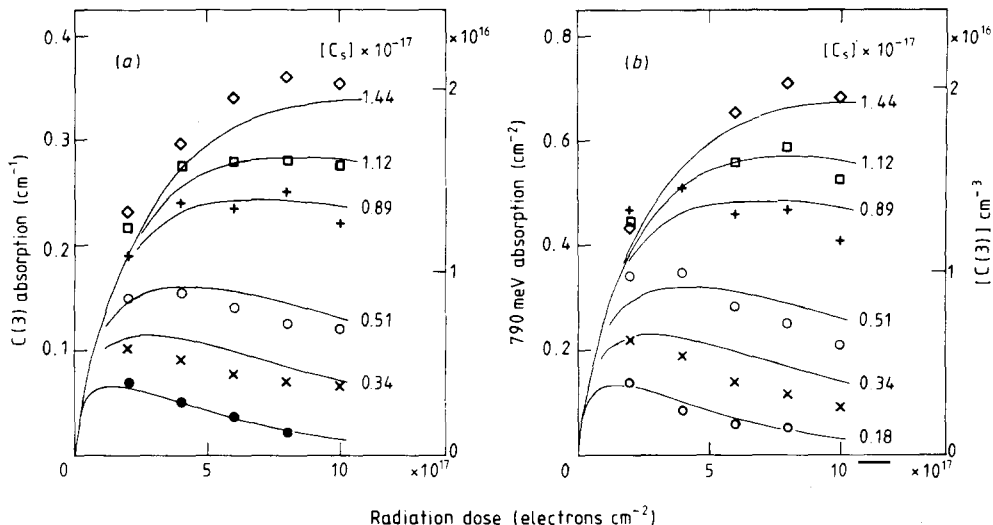


Fig. 60. Production of  $865\text{ cm}^{-1}$  "C(3)" and  $789\text{ meV}$  absorptions (at identical centres, section 5.1) in Czochralski silicon as functions of irradiation dose at  $100^\circ\text{C}$  with  $2\text{ MeV}$  electrons. Carbon concentrations are as shown. Lines are calculated as in section 6.5 [179].

calculated concentrations must be converted to absorption by introducing one further adjustable parameter for each band. Figures 59 and 60 show the calculated absorptions for the  $789$  and  $969\text{ meV}$  bands, as functions of the dose of  $2\text{ MeV}$  electrons compared with measured data [231]. Fits to many other bands, using the same parameters, are in refs. [179, 231].

This type of fitting appears to give accurate values for the factor relating the absorption to concentration of the centres. For the  $969\text{ meV}$  band the factor given by the fit [231] is within  $3\%$  of the directly measured value, eq. (73), which was obtained later. Similarly, the factor for the A centre is within  $30\%$  of the measured value [227]. The agreement implies that the assumptions of the model are essentially correct, particularly that the rate of creating radiation damage is as eq. (81), and that the many other reactions which could in principle occur are irrelevant at  $100^\circ\text{C}$ . For example, there are evidently negligible reactions of I's with O. Factors relating absorption and concentration are gathered in table 1. This type of modelling explains other data. For example, when  $[\text{O}] \gg [\text{C}(\text{s})]$ , the rate of removal of C(s) is half that of O during an irradiation (in the limit of low doses) [232]. This is because the rates of creation of single vacancies and self-interstitials are approximately equal (section 6.2); each I removes one C(s) atom which is then at one O atom, and a second O atom is removed when a V is trapped to form a V-O A centre.

This modelling approach is powerful, and needs to be extended to include other impurities. Preliminary data for trapping a V at an Sn atom or a C(i) at a P atom are [224, 233]

$$R(\text{V}, \text{Sn})/R(\text{V}, \text{O}) = 0.3, \quad R(\text{C}(\text{i}), \text{P})/R(\text{C}(\text{i}), \text{C}(\text{s})) = 10. \quad (88)$$

Boron is known to be a powerful trap for I's (at  $100^\circ\text{C}$ ) with values for  $R(\text{I}, \text{B})/R(\text{I}, \text{C}(\text{s}))$  estimated at 10 [234], 50 [224] and 1000 [230]. The large capture radius of I at Group III impurities implies that the radiation damage reactions may be sample dependent at small doses through the effects of residual impurities. Photoluminescence spectra may then contain many new features.

### 6.6. Subthreshold damage creation of photoluminescence centres

Irradiating silicon with electrons whose energies are only tens of keV, considerably less than that required for radiation damage (section 6.1), can produce photoluminescence at 789 and 969 meV [3]. Damage centres are also observed by other techniques after the silicon has been exposed to low energy electrons [235]. Consequently in a cathodoluminescence experiment (section 4.3) the electron beam used for excitation may modify the luminescence spectrum.

This "subthreshold radiation damage" originates in bombardment of the silicon by ions carried down the electron beam. The effect has been investigated [236] by irradiating silicon doped with  $^{13}\text{C}$ : The specific samples had a  $^{13}\text{C}$ : $^{12}\text{C}$  ratio of  $(4.5 \pm 0.5):1$  as measured by the local modes of substitutional carbon (section 4.1.1). Any carbon contamination in the irradiation chamber or on the surface of the sample would have the natural isotope ratio  $^{13}\text{C}$ : $^{12}\text{C} = 0.01:1$ . The effect of a 20 to 60 keV electron beam was to generate 969 meV centres, produced by C(i) atoms migrating to C(s) atoms (section 6.5). If the C(i) atoms are generated in the crystal they will also be 90%  $^{13}\text{C}$ , resulting in a ratio 4.5:1 for the relative intensities of the local-mode sidebands in the 969 meV band (since this local mode is primarily caused by the vibrations of one C atom, section 5.2). If the C(i) atoms are generated outside the crystal 99% of them will be  $^{12}\text{C}$ . Of the 969 meV centres 82% will contain one  $^{13}\text{C}$  and one  $^{12}\text{C}$ , and 18% will contain two  $^{12}\text{C}$  atoms. Consequently 41% of the local-mode intensity is caused by  $^{13}\text{C}$  atomic vibrations, and  $(41 + 18)\%$  by  $^{12}\text{C}$  atoms, giving a ratio of the  $^{13}\text{C}$  and  $^{12}\text{C}$  local modes of  $\sim 0.7:1$ .

Figure 61 shows that the observed ratio varies with the electron beam energy, but is always substantially less than 4.5, showing that most of the C(i) atoms originate outside the crystal. However, the ratio is always greater than 0.7, so that some C(i) atoms are generated inside the crystal, possibly because of damage caused by ionic bombardment.

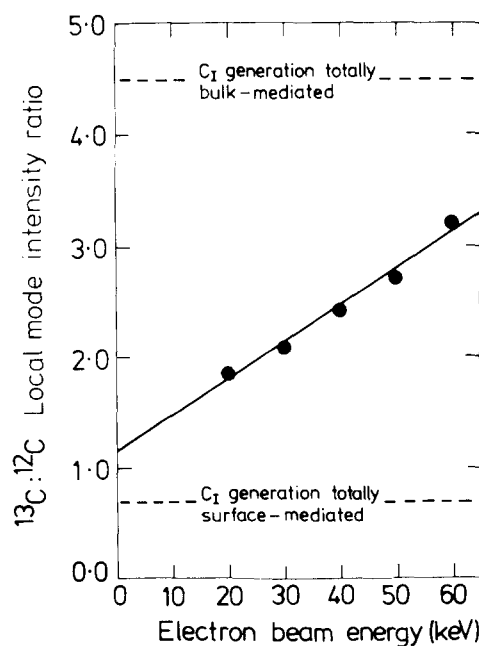


Fig. 61. Ratio of the local-mode absorption in the 969 meV photoluminescence band for subthreshold radiation damage by electrons of 20 to 60 keV in silicon doped with  $[^{13}\text{C}]/[^{12}\text{C}] = 4.5$  [236].

These data give structural information on the 969 meV centre. Suppose that when the C(i) atom attached to the C(s) atom they preserved their identities and that the C(i) atom was the one observed in the local-mode sideband. Then the local-mode ratio plotted in fig. 61 would be 0.01, from the natural abundance of  $^{13}\text{C}$ . Similarly if the C(s) atom vibrated the ratio would be 4.5:1 even when the C(i) atom came from outside the crystal. The data imply that there is no permanent preservation of one atom as the C(i) and one as the C(s) in a 969 meV centre. Relaxation of the centre through the symmetric structure observed in ODMR would randomise the  $^{13}\text{C}$  and  $^{12}\text{C}$  atoms in the two distinguishable sites of the asymmetric G11-like structure (section 5.2).

### 6.7. Heavy-particle damage

Irradiation with ions and neutrons allows regions of multiple damage to be created. Some vacancies and self-interstitials will escape from the heavily damaged regions to create the photoluminescence centres observed with electron damage. But in addition, new photoluminescence systems are created

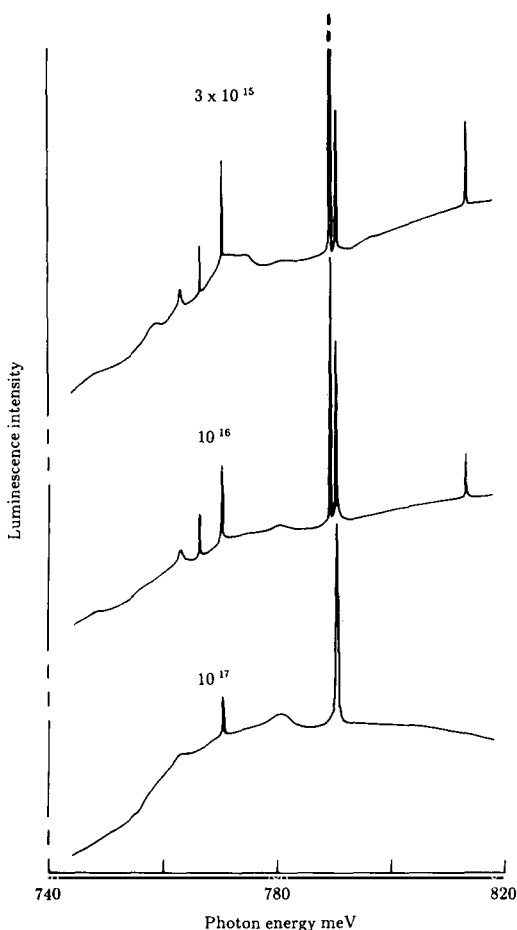


Fig. 62. Differences in photoluminescence generated in Czochralski silicon of  $[C] = 5 \times 10^{18} \text{ cm}^{-3}$  after irradiation at  $40^\circ\text{C}$  with fast neutrons to doses of  $3 \times 10^{15}$ ,  $10^{16}$  and  $10^{17} \text{ cm}^{-2}$ .

[237, 238]. Common systems produced by irradiation near room temperature and then annealing are the 1018 meV band (section 5.4) and the 1040 meV band (section 8). With heavy-ion bombardment it is easy to get into the high-dose regime [183], where the 789 and 969 meV bands decrease in intensity as the centres trap self-interstitials (section 6.4). However, there are also subtle progressions in the spectral form near 789 meV as the neutron dose increases (fig. 62), and these have not been investigated in any detail.

## 7. Vibronic properties

The molecular configuration of a photoluminescence centre is different depending on which of its electronic states is occupied. This dependence is responsible for the shape and temperature dependence of the luminescence band (sections 7.1–4), and for its isotope dependence (section 7.5).

### 7.1. Basic bandshapes

When a photoluminescence transition occurs at an optical centre, an electron moves from one orbital to another. This change in electron distribution produces a change in the chemical bonds at the centre. The equilibrium positions of the atoms forming the centre are likely to be different in the two electronic states, and the vibrational frequencies will also differ.

Consider first an optical centre with only one vibrational coordinate and with non-degenerate electronic states which are well separated in energy from all other electronic states. In the ground electronic state the vibrational potential is written

$$V_g = \frac{1}{2}m\omega^2 Q^2, \quad (89)$$

where  $m$  is the effective mass,  $\omega$  the vibrational frequency and  $Q$  the magnitude of the vibrational displacement. In the excited electronic state the centre has a larger electronic energy  $E$  (measured at  $Q=0$ ). However, because the bonding has changed, the centre is no longer stable at  $Q=0$  but “relaxes” through an energy  $E_r$  to a new equilibrium position at  $Q=Q_0$ . The new vibrational potential is

$$V_e = E + \frac{1}{2}m\Omega^2(Q - Q_0)^2 - E_r, \quad (90)$$

where  $\Omega$  is the new vibrational frequency. If  $\Omega = \omega$ , which is usually a good approximation in silicon, eq. (90) is usefully written as

$$V_g = E + \frac{1}{2}m\omega^2 Q^2 + aQ, \quad (91)$$

where

$$E_r = a^2/2m\omega^2, \quad Q_0 = -a/m\omega^2, \quad (92)$$

and  $a$  is the “linear electron–phonon coupling term”. It changes the electronic energy by an amount proportional to the deformation  $Q$  of the centre and so can be estimated from the effects of applied

stress (section 7.2). In order to affect the electronic energy of these non-degenerate states,  $Q$  must transform as the totally symmetric representation of the point group of the centre—i.e., during a vibration the symmetry of the centre must remain the same.

The relaxation energy  $E_r$  can be written dimensionlessly in terms of the phonon quantum  $\hbar\omega$  and the “Huang–Rhys factor”  $S$ ,

$$S = E_r/\hbar\omega = a^2/2m\hbar\omega^3. \quad (93)$$

The Born–Oppenheimer approximation for the  $n$ th harmonic oscillator state of the electronic states is

$$\psi_{gn}(r, Q) = \phi_g(r)\chi_n(Q), \quad \psi_{eN}(r, Q) = \phi_e(r)\chi_N(Q - Q_0), \quad (94)$$

where  $\phi_g$ ,  $\phi_e$  denote the ground and excited electronic states (coordinate  $r$ ) and  $\chi$  the vibrational state. The photoluminescence electric dipole operator  $d$  connects the electronic states but not the vibrational states, enabling the transition matrix element to be factorised,

$$T_{eN,gn} = \int dr dQ \psi_{eN}^* d\psi_{gn} = \int dr \phi_e^* d\phi_g^* \int dQ \chi_N^*(Q - Q_0) \chi_n(Q). \quad (95)$$

We let

$$P = \int dr \phi_e^* d\phi_g, \quad (96)$$

and concentrate on the vibrational part. When  $Q_0 \neq 0$ , the vibrational states are no longer orthonormalised and transitions are allowed from a zero-phonon level ( $N = 0$ ) to any phonon state  $n$  with a relative transition probability

$$I_n = \left| \int dQ \chi_0^* \chi_n \right|^2 = S^n \exp(-S)/n!, \quad (97)$$

where  $S$  is the dimensionless relaxation energy of eq. (97). In an experiment  $S$  is found from the fraction of the transition probability which lies in the zero-phonon line,

$$S = \ln(I_n) - \ln(I_0). \quad (98)$$

In a luminescence experiment the transition probability  $I(\nu)$  is proportional to the number  $L$  of photons emitted per second per unit frequency range divided by the cube of the frequency  $\nu$ ,

$$I \propto L/\nu^3. \quad (99)$$

For an absorption spectrum  $I$  is proportional to the absorption coefficient  $A(\nu)$  divided by the frequency,

$$I \propto A/\nu. \quad (100)$$

Photoluminescence bands with the shape expected from the single coordinate model are observed [239] at a lithium-related centre produced in silicon by irradiation at room temperature followed by annealing at  $\sim 450^\circ\text{C}$  (fig. 63). This band can be described with a Huang–Rhys factor  $S \sim 2$  and a well-defined phonon quantum of  $\sim 7$  meV.

Usually an optical centre has a very large number of vibrational modes (equal to  $3r - 6$ , where  $r$  is the number of atoms forming the centre). The generalisations of eqs. (89) and (90) are

$$\begin{aligned} V_g &= \frac{1}{2} \sum_i m_i \omega_i^2 Q_i^2, \\ V_e &= E + \frac{1}{2} \sum_i m_i \omega_i^2 Q_i^2 + \sum_i a_i Q_i \\ &= E + \frac{1}{2} \sum_i m_i \omega_i^2 (Q_i - Q_i^0)^2 - \sum_i S_i \hbar \omega_i, \end{aligned} \quad (101)$$

where  $Q_i^0$  is the change in equilibrium position of the  $i$ th vibrational mode and  $S_i$  is the Huang–Rhys factor for that mode,

$$S_i = a_i^2 / m_i \hbar \omega_i^3. \quad (102)$$

Because the vibrational modes are not mixed by the linear electron–phonon terms  $a_i Q_i$ , they are all independent of each other and the bandshape has properties similar to those of the single mode case. At low temperature ( $kT \ll \hbar \omega$ , where  $\omega$  is the frequency of the phonons which dominate the luminescence band), the sideband involving  $n$  phonons of any frequency has a relative intensity

$$I = S^n \exp(-S)/n!, \quad S = \sum_i S_i. \quad (103)$$

Because the phonons are independent of each other the probability of choosing  $n$  phonons is completely statistical. The  $n$ th phonon sideband  $P_n$  can be constructed from the  $(n-1)$ th sideband  $P_{n-1}$  and the one-phonon sideband  $P_1$  by taking all combinations of the two sidebands,

$$P_n(\omega) \sim \int dx P_{n-1}(\omega - x) P_1(x), \quad (104)$$

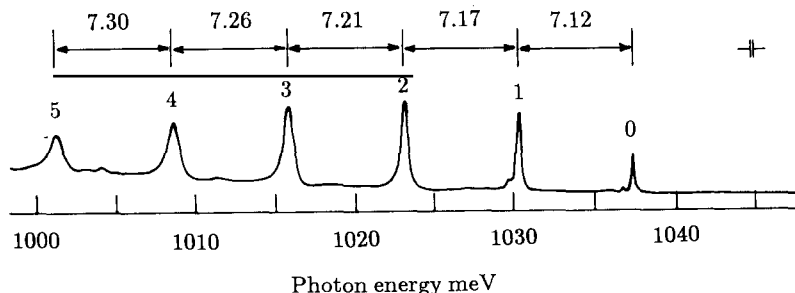


Fig. 63. Photoluminescence at 2.5 K from float-zone silicon with  $[\text{Li}] = 2 \times 10^{17}$  and  $[\text{C}] = 2 \times 10^{17} \text{ cm}^{-3}$  after irradiation with  $2 \times 10^{17} \text{ cm}^{-2}$  2 MeV electrons and 40 min annealing at  $450^\circ\text{C}$  [239]. The separations (in meV) of successive sidebands are shown.

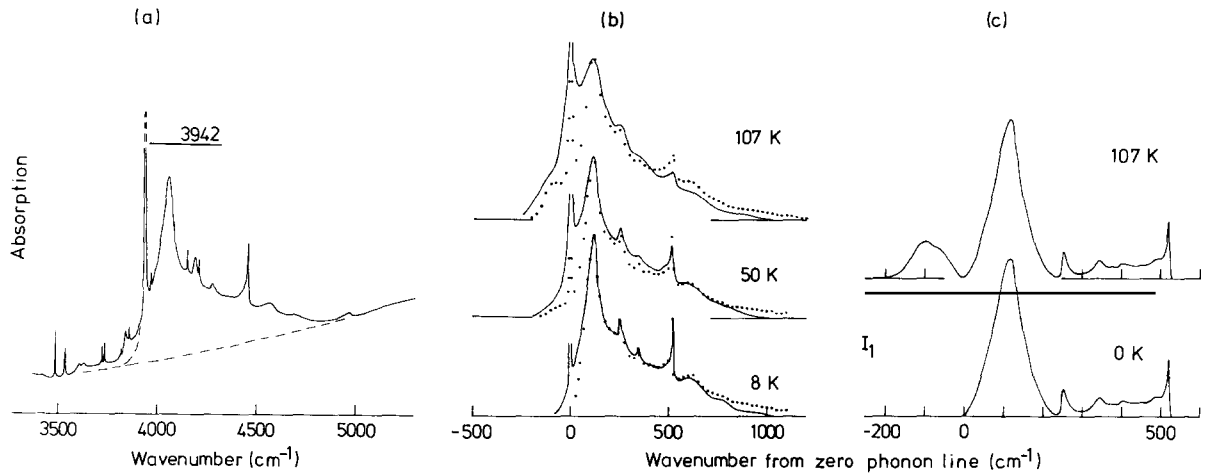


Fig. 64. (a) Absorption spectrum of the 488 meV band at 8 K, with an estimated baseline shown by the broken line. (b) Measured spectra at 8, 50 and 107 K (lines); dots show the fits using the theory of section 7.1. (c) The one-phonon sidebands. [240]

where  $\omega$  is the maximum frequency in the one-phonon sideband. (We do not need to distinguish between band modes and local modes at this stage.)

Figure 51 shows this theory applied to the 1018 meV luminescence band, and fig. 64 to the 488 meV absorption band [240]. In each case the Huang–Rhys factor is found by applying eq. (98) to the fraction of the intensity in the zero-phonon line, and the one-phonon bandshapes are those which give the best reconstruction of the total observed bandshapes.

With increasing temperature the zero-phonon line decreases in intensity as intensity is transferred to

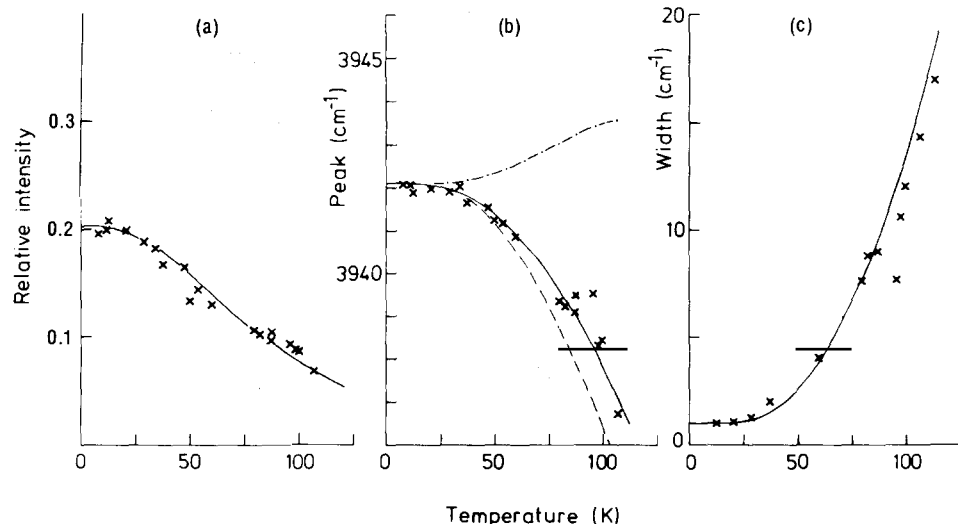


Fig. 65. Temperature dependence of the intensity, peak energy and full width at half height of the 488 meV zero-phonon absorption line. Solid lines are fits (sections 7.1 and 7.5). For the peak energy, the chain line shows the thermal expansion term, the broken line shows the quadratic electron–phonon term [240].

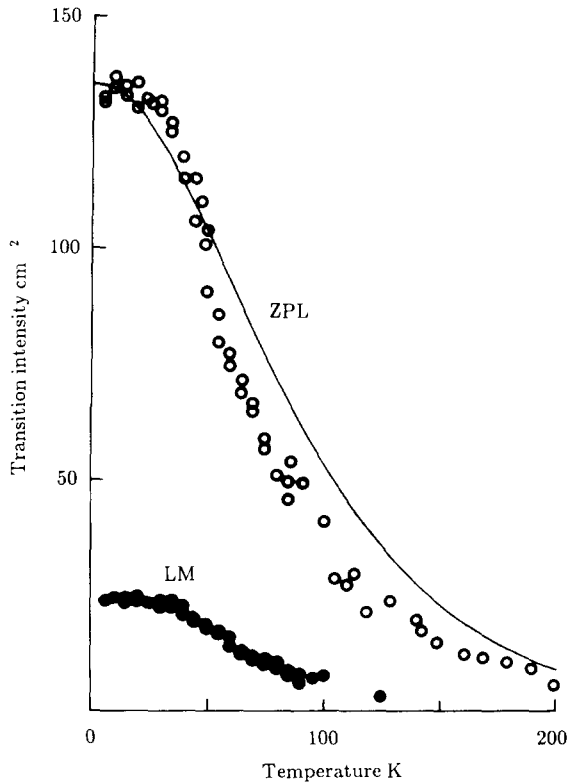


Fig. 66. Intensity of the 969 meV zero-phonon absorption line as measured (open circles) and calculated (eq. 105) using  $P_1$  determined from the photoluminescence spectrum [91]. Filled circles show data for the 72 meV local-mode sideband in the same silicon [91].

the phonon sideband. The decrease can be calculated *explicitly* from the one-phonon sideband's shape  $P_1(\omega)$  (which contains the information about the linear electron-phonon coupling). The zero-phonon intensity  $I_0$  is [255]

$$I_0(T) = \exp\left(-\int d\omega P_1(\omega)[1 + 2n(\omega)]\right). \quad (105)$$

Figures 65 and 66 show that the intensity of the 488 meV and 969 meV zero-phonon *absorption* lines can be described accurately using this theory. The rapid decreases in luminescence at  $T \geq 30$  K (section 3.1.1) are not caused by the vibronic coupling.

In linear electron-phonon coupling the absorption and luminescence processes are symmetrical, and the luminescence band is expected to be the same shape as the absorption band reflected in the frequency scale about the zero-phonon line. This is approximately obeyed (e.g. figs. 45 and 49 for the 969 meV band; fig. 64 and ref. [241] for the 488 meV band).

## 7.2. Link to uniaxial stress data

The linear electron-phonon term  $a_i$  (eq. 92) is the change in energy per unit extension in  $Q_i$ . If a static deformation  $Q'_i$  could be applied to the luminescence centre, the measured change in zero-

phonon energy  $h\nu = -a_i Q'_i$  would give  $a_i$ . However, there is a severe limit on the number of independent stresses which can be externally applied. For a monoclinic I centre (the symmetry class most commonly met in silicon) only four independent linear stress perturbations can be measured. In principle the strain  $e$  produced by a stress  $s$  is given as  $e = s/c$ , where  $c$  is the appropriate elastic constant. Hence the atoms move through  $Q' = el$ , where  $l$  is a suitable scaling length. The Huang-Rhys factor  $S_i$  is then given in terms of the effective mass  $m_i$  and the frequency  $\omega_i$  of the mode (eq. 102).

In practice we do not know the required parameters. For example, the elastic constants near the luminescence centre will differ from those of the bulk lattice because the chemical bonding is different near the centre, and  $m_i$  and  $\omega_i$  of particular modes are also unknown. The best that can be done empirically is to use a Si-Si bond length for  $l$ , and the frequency of the dominant phonon in the sideband for  $\omega$ . If the sidebands involve lattice modes, the appropriate mass is the Si atomic mass; otherwise the appropriate impurity has to be used. This process has been very successful in understanding the electron-phonon coupling in diamond [20].

For a specific example we take the 1018 meV transition which occurs between non-degenerate orbital states at a trigonal complex of silicon atoms (section 5.4). The transition is primarily perturbed to first order by hydrostatic stresses, giving an energy change  $A_1 = 1.5 \text{ meV/GPa}$  [202]. The electron-phonon coupling in this breathing mode is therefore

$$a = A_1 f(c_{11} + 2c_{12})/l, \quad (106)$$

where  $f$  is the correction which has to be applied to the sum of the elastic constants near the luminescence centre. Using  $\hbar\omega = 17 \text{ meV}$  (fig. 51) gives  $S = 0.55f^2$ . Agreement is obtained with experiment if the centre is harder to deform than the pure lattice ( $f \sim 1.3$ ), consistent with the occurrence of the Si local mode at this centre (section 5.4).

Most photoluminescence centres in silicon have monoclinic I symmetry (point groups  $C_2$  or  $C_{1h}$ ). A typical example of one of the 12 equivalent orientations of the centres is for the unique axis (defined as the  $Z$  axis) to lie on the [110] crystallographic direction. Two orthogonal axes  $X = [001]$  and  $Y = [1\bar{1}0]$  can be defined. (There is no symmetry restriction on the orientation of these  $X$  and  $Y$  directions in the plane whose perpendicular is the one uniquely defined axis of the centre.) Under stress, first-order perturbations of the non-degenerate states are produced by the terms in the Hamiltonian which are totally symmetric in the point group,

$$V = p_{XX}s_{XX} + p_{YY}s_{YY} + p_{ZZ}s_{ZZ} + p_{XY}s_{XY}, \quad (107)$$

where the  $s_{IJ}$  are stress tensor components defined in terms of the axes ( $X$ ,  $Y$ ,  $Z$ ) local to each centre. The effects of stress are conventionally defined by the four parameters  $A_1, \dots, A_4$  [242],

$$\begin{aligned} A_1 &= \langle e | p_{XX} | e \rangle - \langle g | p_{XX} | g \rangle, \\ A_2 &= (\langle e | p_{YY} + p_{ZZ} | e \rangle - \langle g | p_{YY} + p_{ZZ} | g \rangle)/2, \\ A_3 &= (\langle e | p_{ZZ} - p_{YY} | e \rangle - \langle g | p_{ZZ} - p_{YY} | g \rangle)/2, \\ A_4 &= (\langle e | p_{XY} | e \rangle - \langle g | p_{XY} | g \rangle)/2^{3/2}, \end{aligned} \quad (108)$$

where  $|e\rangle$  and  $|g\rangle$  denote the excited and ground states of the zero-phonon line. Assuming that the

elastic constants are unchanged near the optical centre the coupling terms  $a_{XX}, \dots, a_{XY}$  for modes producing each deformation are

$$\begin{aligned} a_{XX} &= (A_1 c_{11} + 2A_2 c_{12})/l, \\ a_{YY} &= [A_1 c_{12} + A_2(c_{11} + c_{12}) - A_3 c_{44}]/l, \\ a_{ZZ} &= [A_1 c_{12} + A_2(c_{11} + c_{12}) + A_3 c_{44}]/l, \\ a_{XY} &= A_4 c_{44}/l, \end{aligned} \quad (109)$$

and the Huang–Rhys factors for the corresponding modes of vibration are

$$S_{IJ} = a_{IJ}^2 / 2m\hbar\omega_{IJ}^3. \quad (110)$$

These expressions assume that only the atoms nearest to the middle of the optical centre vibrate, so that the change in charge distribution is localised within two neighbours of the middle, but in practice this is not over-restrictive (section 8). The monoclinic I 789 meV centre (section 5.1) is primarily perturbed by the  $A_1$  term, with  $A_1 = -13$  meV/GPa [176]. Equations (108)–(110) give  $S = 2.4$  when  $\hbar\omega = 30$  meV, the mean of the observed modes, close to the measured value  $S = 2$ .

Sometimes these expressions only give the observed values of  $S$  if the effective phonon frequency  $\omega_{IJ}$  is about a factor of two different from the dominant phonons observed in the phonon sideband. For example, for the 488 meV band a phonon frequency of  $260\text{ cm}^{-1}$  has to be used, twice the value observed in fig. 64. Because  $\omega$  enters the Huang–Rhys factor as  $\omega^3$  (eq. 110), considerable errors could result in an estimate of  $S$  from the uniaxial stress data. Recent very detailed work on the well-defined system MgO:Fe produces the same conclusion [243], and also shows that the *relative* Huang–Rhys factors in different modes may also be in error. Also, in contrast to the assumptions in eq. (109), the relaxations of atoms near the optical centres need not be a monotonic function of their distance from the optical centre. In their electronic ground states interstitial transition metals in silicon are predicted [244] to push the four nearest neighbours outwards (by 0.007 nm) and pull the six next-neighbours inwards (by 0.01 nm), as observed by EXAFS [245].

### 7.3. Local and resonant modes

In silicon a local mode has a phonon quantum greater than 65 meV, the lattice cutoff (section 2.1). Local modes are produced either by bonds which are stronger than usual, or by the effective mass of the vibrating system being small. An example of strong bonding is the local mode of the 1018 meV band with  $\hbar\omega = 70.0$  meV (fig. 51). The vibration is predominantly by one Si atom, as shown by the  $^{28}\text{Si}$ ,  $^{29}\text{Si}$  and  $^{30}\text{Si}$  isotope structure in the ratios of the natural isotopes of silicon, eq. (1). If one Si atom vibrated against the infinite mass of the remainder of the lattice, the frequencies of the modes with  $^{28}\text{Si}$  and  $^{30}\text{Si}$  would be in the ratio  $(30/28)^{1/2} = 1.035$ . The observed ratio,  $^{28}\omega/^{30}\omega = 1.028$ , could arise if one Si atom vibrates against a cluster of a few (literally four) other Si atoms. Isotope changes amongst these other atoms will not produce discrete structure but will contribute to the linewidth and will produce an asymmetric tail stretching to lower phonon energy. This slight asymmetry can be seen more clearly on the local-mode sidebands labelled  $^{16}\text{O}$  on fig. 43.

Most of the local modes in silicon are produced by the vibrating atom being an impurity (e.g. C, O)

of low mass. Isotope shifts in the local modes indicate unambiguously the presence of a particular impurity in the centre (e.g. sections 5.1 and 5.2.2). A light atom is not, however, a sufficient condition for a local mode: the four-lithium atom complex (section 5.5) has no local modes.

Because a local mode is spatially localised on the optical centre, it is sensitive to the electronic orbitals occupied at the centre. The vibrational quantum is different in the ground and excited electronic states of the optical centre. In an optical spectrum measured at low temperature the phonon sidebands have the vibrational quanta characteristic of the final electronic state of the transition. Consequently the phonons measured in photoluminescence and in absorption spectra are characteristic, respectively, of the electronic ground and excited states. Table 3 lists the changes in quanta in the few cases where these differences are known. The frequency changes are

$$(\hbar\omega_g - \hbar\omega_e)/\hbar\omega_e \sim 3\% \quad (111)$$

for the modes listed; these modes all have quanta just above the lattice cutoff of  $\hbar\omega_R = 65$  meV. In the two cases known in diamond [13] the changes vary between 5 and 17%.

A local mode which makes a contribution to the one-phonon sideband  $P_1$  will also appear, by eq. (104), in the multi-phonon sidebands. Because the local mode is sharp, a photoluminescence spectrum appears to contain sidebands of the zero-phonon line with a similar set of sidebands repeated from the local-mode line, as on fig. 45, where the combinations of the local mode L and the peaks of the acoustic

Table 3  
Isotope effects on local and resonant modes.

Line (meV)	Element	Light isotope	Heavy isotope	Phonon quanta (meV)		Ref.
				light	heavy	
745.6	N	14	15	122.9	119.7	[274]
	C	12	13	122.9	121.9	
789	O	16	18	65.5	64.8	[169]
	O	16	18	72.6	72.2	
	Si	28	30	72.6	71.3	
951	C	12	13	72.2	70.2	[254]
953	C	12	13	71.0	69.0	[254]
957	C	12	13	71.1	69.2	[254]
	C	12	13	66.7	65.3	
969	C	12	13	71.9	70.0	[254]
	C	12	13	67.35	66.0	
1014	Cu	63	65	7.05	6.93	[200]
1018	Si	28	30	70.0	68	[202]
1037.3	Li	6	7	7.2	7.12	[239]
1045	Li	6	7	34.2	32.2	[210]
	Li	6	7	50.7	47.9	
	Li	6	7	59.8	55.1	
1080	B	10	11	109.4	104.6	[78]

A and optic O modes are labelled. At low temperature ( $kT \ll \hbar\omega_L$ ) the local mode and the zero-phonon line have similar properties. For example, their response to stresses is the same (since anharmonicity in the local modes is small) [202], and their integrated transition probabilities both follow eq. (105) (fig. 66).

If the photoluminescence centre contains heavy atoms (e.g. Fe), the vibrations have frequencies which lie in the continuum of the host lattice, but in regions of low densities of phonon states. The “resonant” mode produced may be only  $\sim 1$  meV wide (fig. 67). Resonances may also be produced by light impurities in a “molecular” centre, e.g. the four-Li atom centre (section 5.5). (The spectrum of fig. 63 occurs at a centre which also definitely involves Li, but the phonon energy observed in the sideband is independent of the Li isotope [239], implying that in this centre the resonant phonons do not involve this light atom.)

The 1045 meV band shows three resonances, A, B, C on fig. 68, two of which (A and B) are clear of other structure in the band. The 1045 meV transition occurs between non-degenerate and doubly degenerate electronic orbitals at a trigonal centre which to a first approximation is a slightly deformed tetrahedral centre (section 5.5). Linear electron–phonon coupling (section 7.1) is allowed with both totally symmetric and doubly degenerate (e-mode) vibrations. In the totally symmetric breathing mode all the Li atoms move approximately equal amounts (exactly equal in the  $T_d$  symmetry). With mixed Li isotopes, containing a fraction  $p$  of  $^{6}\text{Li}$  and  $q$  of  $^{7}\text{Li}$  atoms, this mode will consist of a set of five lines, corresponding in intensity to the five terms in the expansion of  $(p + q)^4$ . This behaviour is shown by the “B” resonance on fig. 68. In an e-mode of vibration a pair of Li atoms can move, the others being

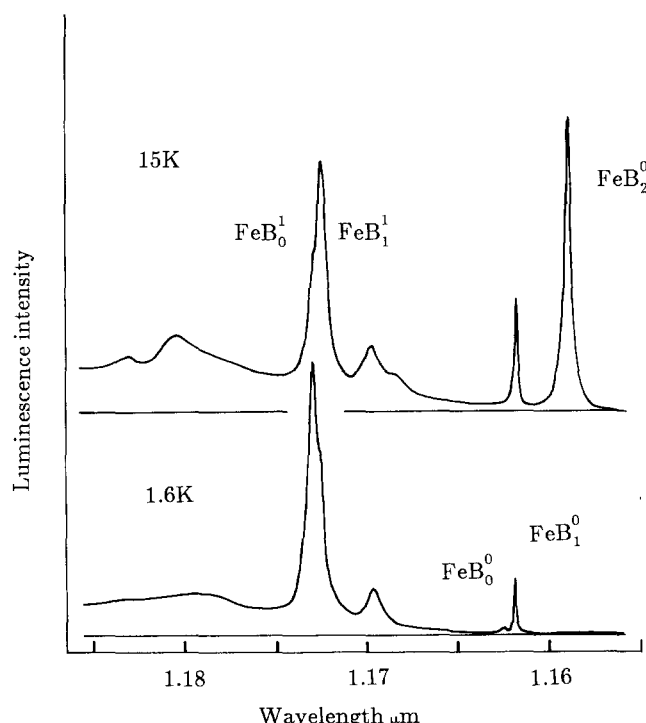


Fig. 67. Photoluminescence from silicon diffused with Fe [247]. The zero-phonon lines are labelled  $\text{FeB}_0^0$ ,  $\text{FeB}_1^0$ ,  $\text{FeB}_2^0$ . Sidebands labelled  $\text{FeB}_0^1$  and  $\text{FeB}_1^1$  are suggested to be transitions from  $\text{FeB}_0^0$  and  $\text{FeB}_1^0$  which are vibronically induced through mixing with  $\text{FeB}_2^0$ ; see fig. 70.

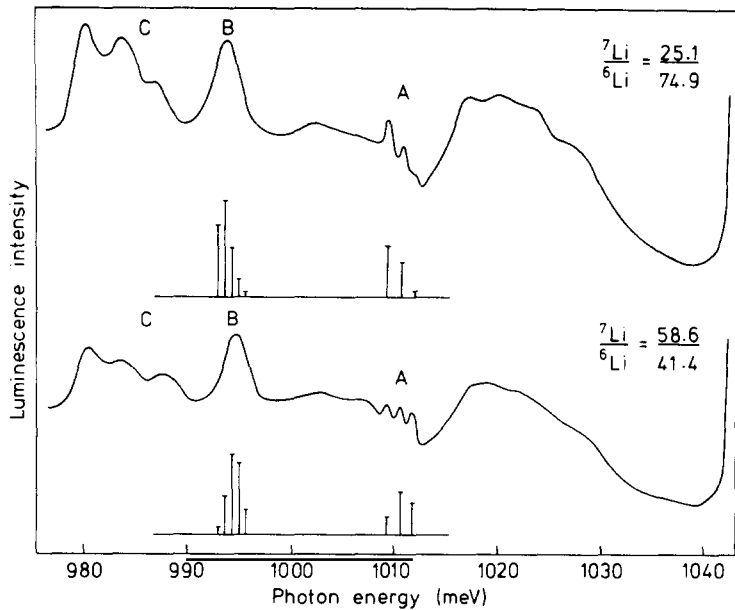


Fig. 68. Photoluminescence in the vibronic sideband of the 1045 meV 4-Li atom complex, showing the effects on the resonant modes "A" and "B" of isotope doping ratios shown on the right [11].

stationary. Then we expect the mode to show three different frequencies corresponding in intensity to the expansion of  $(p + q)^2$ , as shown by resonance A (fig. 68).

Isotope shifts in resonant modes are also seen in the 1014 meV Cu band (section 5.3), where the mode changes from 7.05 to 6.93 meV on changing  $^{63}\text{Cu}$  to  $^{65}\text{Cu}$  [200]. This is similar to the effect on the 9 meV resonant mode of interstitial Fe, which is predicted to be changed by 0.17 meV on changing from  $^{54}\text{Fe}$  to  $^{56}\text{Fe}$  [246].

#### 7.4. Nearly degenerate excited states

Most of the photoluminescence centres in silicon have multiple excited states which interact strongly under stress (section 8). Interactions may therefore be induced between the states by vibrations of the centres. Even in the zero-point vibrational state, the root mean square amplitude  $r$  of vibrations with quanta  $\hbar\omega = 30 \text{ meV}$  and mass  $m$  equal to one Si atom is

$$r = (\hbar/2m\omega)^{1/2} = 5\% \text{ of a bond length ,} \quad (112)$$

and is large compared with the strains ( $< 0.2\%$ ) produced in uniaxial stress experiments.

Again we take first the single mode case. Suppose an optical centre has two non-degenerate excited states  $\phi_1$  and  $\phi_2$ , and that it has the same atomic configuration in each. The Born–Oppenheimer states are

$$\psi_{1n}(r, Q) = \phi_1(r)\chi_n(Q) , \quad \psi_{2N}(r, Q) = \phi_2(r)\chi_N(Q) . \quad (113)$$

A linear electron-phonon term  $aQ$  is assumed to mix  $\phi_1$  and  $\phi_2$  but not to produce any further first-order relaxation. Then

$$\int dr \phi_1^* a \phi_2 = A, \quad \int dr \phi_1^* a \phi_1 = \int dr \phi_2^* a \phi_2 = 0. \quad (114)$$

Because the coupling is linear in  $Q$  it can only mix vibrational states which differ by  $\pm 1$  in the vibrational quantum number. The Born-Oppenheimer states (eq. 113) interact through

$$\int dr dQ \psi_{1,n}^* a Q \psi_{2,n+1} = A[(\hbar/m\omega)(1+n)]^{1/2}, \quad \int dr dQ \psi_{1,n}^* a Q \psi_{2,n-1} = A[(\hbar/m\omega)(n)]^{1/2}, \quad (115)$$

with all other matrix elements zero.

The coupling has particularly large effects on the luminescence spectrum if transitions are forbidden from the lower excited state (say  $\phi_1$ ) to the ground electronic state  $\phi_g$ , but are allowed from  $\phi_2$  to  $\phi_g$ . The coupling (eq. 115) mixes the one-phonon level  $\phi_2\chi_1$  into  $\phi_1\chi_0$ . Optical transitions which were completely forbidden from  $\phi_1\chi_0$  are now allowed, even at 0 K.

The effect is shown in figs. 67 and 69. Both these bands are enhanced by the diffusion of iron into silicon [247-249], but neither shows isotope shifts from Fe [250, 246]. They have similar zero-phonon structure: a doublet (lines "0" and "1" of splitting 0.4 or 0.5 meV in the two cases) with a line "2"  $\sim 3$  meV to higher energy. From the limiting behaviour at high temperature the transition probability of line 2 is much larger ( $\sim 20$  and  $\sim 8$  times) than that of line 1. The  $1.7 \mu\text{m}$  band has the form expected

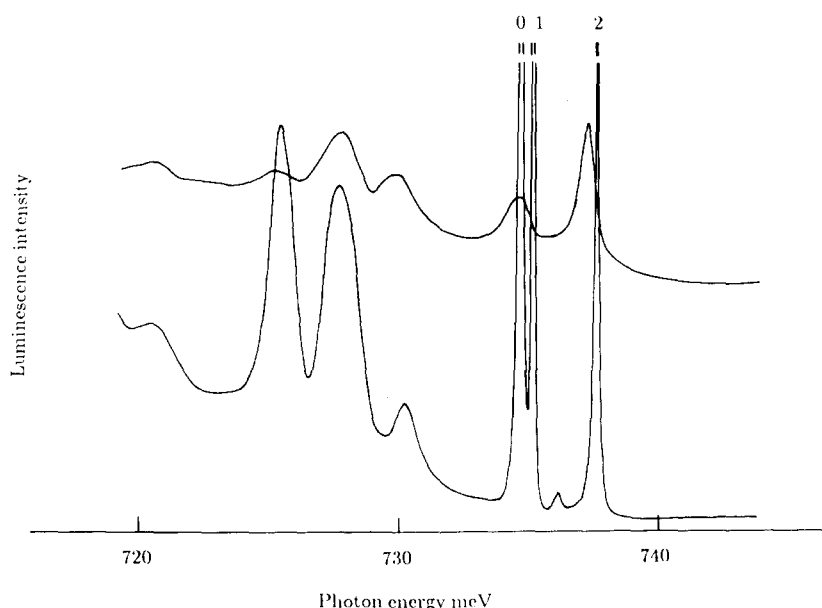


Fig. 69. Zero-phonon region measured at 9 and 40 K of a photoluminescence band resulting from Fe diffusion (cf. fig. 67) [271].

from section 7.1, with phonon sidebands at  $\hbar\omega_1 \sim 7.5$  meV and  $\hbar\omega_2 \sim 10$  meV below the respective zero-phonon lines, and with Huang–Rhys factors for these modes of

$$S_1 \sim S_2 \sim 1.5. \quad (116)$$

In contrast, at low temperature the 1.16  $\mu\text{m}$  band consists to a good approximation of the very weak zero-phonon lines 0 and 1, with the far stronger  $\hbar\omega_1$  and  $\hbar\omega_2$  phonon sidebands (fig. 67). From the ratio of the areas of the 10 meV phonon and the 0 and 1 zero-phonon lines, the Huang–Rhys factor is apparently “ $S_2$ ”  $\sim 15$ , but succeeding phonon sidebands are weak: the vibronic sidebands are not produced by the simple mechanism of section 7.1. To simplify the problem, assume that in the 1.16  $\mu\text{m}$  band lines 0 and 1 are totally forbidden and condense them into one state “1”. At high temperature there is little evidence of one-phonon sidebands of the strongly allowed line 2, implying that the equilibrium positions of the centre are the same in the ground and excited states [i.e.,  $Q_0 = 0$ , eq. (92)]. The effect on the Born–Oppenheimer states (eq. 113), whose electronic states  $\phi_1$  and  $\phi_2$  are separated by energy  $E_0$  (at  $Q = 0$ ), can be calculated from the secular matrix whose off-diagonal elements are in eq. (115). The calculated bandshape is shown in fig. 70 when the energy separation  $E_0$  and the electron–phonon coupling  $A$  are

$$E_0 = 4 \text{ meV}, \quad A \sim 10^{12} \text{ meV/m}. \quad (117)$$

The value of  $A \sim 0.2$  eV per unit strain is typical for silicon. This calculation reproduces the observed optical properties within the simplifying limitations used (figs. 67, 70). The resulting configurational coordinate diagram is in fig. 71. The two minima are exactly equivalent since the uncoupled states were assumed to have their minimum potential energies at the same value of  $Q$ . Lifting this restriction produces potential curves with minima at different energies, with the qualitative appearance of the surfaces encountered in bistability problems [251].

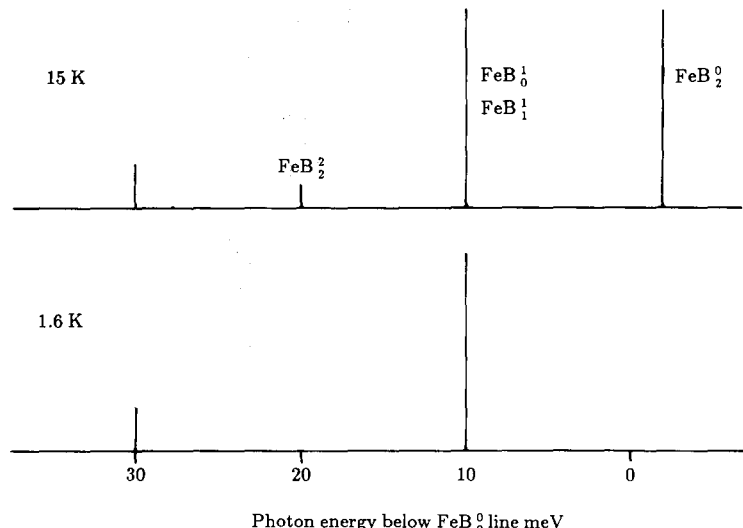


Fig. 70. Simple construction at 1.6 K and 15 K of the bandshape of fig. 67 assuming  $\text{FeB}_0^0$  and  $\text{FeB}_1^1$  are forbidden transitions, and using one vibrational mode to mix in the allowed  $\text{FeB}_2^2$  transition.

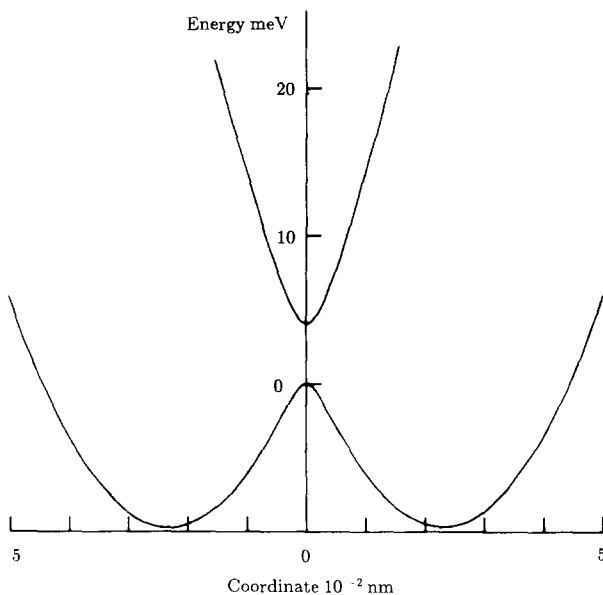


Fig. 71. Vibrational potential energy curves for the excited states of the  $(\text{FeB}_0^0 + \text{FeB}_1^0)$  and the  $\text{FeB}_2^0$  transitions, using the pseudo-Jahn-Teller coupling as for fig. 70.

A similar case of vibronic coupling is seen at the 1076 meV band. At low temperature the lowest excited electronic state is preferentially populated. Transitions to the ground state are weak, but are enhanced by optic-mode coupling to the higher excited states (see fig. 2 of ref. [252]). Otherwise vibronic interactions between different electronic states are surprisingly rare, given the large number of excited states in many centres. At the 1018 meV band (section 5.4), uniaxial stresses produce very small first-order perturbations of the zero-phonon line, but these are adequate to explain the observed strength of the Huang-Rhys factor (section 7.2). There is a stronger interaction between the excited state of the 1018 meV line and other excited states about  $W \sim 40$  meV to higher energy (fig. 52). However, there is no evidence for vibronic interactions between these excited states. The reason is probably that in the 1018 meV band the vibronic coupling is primarily to a continuum of phonon states (fig. 51), in contrast to the discrete modes of the 1.16  $\mu\text{m}$  band. In perturbation theory, the first-order change in energy of one state is proportional to the size of a small perturbation; the interaction of two states of different energy, however, depends on the square of the perturbation relative to the energy separation. Sharing the available perturbation between many modes has no effect on the total sideband strength for an isolated electronic state, but rapidly diminishes the sidebands of states interacting vibronically. Where the vibronic coupling occurs through a continuum of phonon states its effects will be minimal.

There are no photoluminescence centres in silicon which are known to show dynamic Jahn-Teller effects. In contrast, in diamond, dynamic Jahn-Teller effects are observed at optical centres with degenerate orbital ground states (e.g. the neutral vacancy [20]). Strong vibronic interactions are observed between the nearly degenerate states of the photoluminescence centres with zero-phonon lines at 2463, 2499 and 2985 meV [20], the first two at least being caused by resonant modes.

Vibronic coupling has been suggested to be responsible for the off-site distortions of O, S and N in silicon [253].

### 7.5. Quadratic electron-phonon coupling and isotope effects

The change in chemical bonding when the photoluminescence transition occurs changes the frequencies of the modes as well as their equilibrium positions. The frequency changes are small (eq. 111). However, very useful effects are produced.

In the limit of low temperature the zero-phonon energy is (eq. 101)

$$\hbar\nu = (E - E_r) + \frac{1}{2} \sum_i (\hbar\omega_i^e - \hbar\omega_i^g), \quad (118)$$

where  $E - E_r$  is the zero-phonon energy when there are no frequency changes. The sum in eq. (118) is over *all* modes at the optical centre; only some of these modes are observed in the phonon sidebands. There is no direct relation between the observed strength of a mode in a sideband and the size of the frequency change. In the single mode case the vibrational potential in the ground and excited states can be written (cf. section 7.1)

$$V_g = \frac{1}{2}m\omega^2 Q^2, \quad V_e = E + \frac{1}{2}m\omega^2 Q^2 + aQ + bQ^2, \quad (119)$$

where the frequency  $\Omega$  in the excited state is given by

$$\frac{1}{2}m\Omega^2 = \frac{1}{2}m\omega^2 + b. \quad (120)$$

Because the quadratic electron-phonon term  $bQ^2$  depends on  $Q^2$  there is no restriction on which modes can have their frequencies changed. In the many-mode case  $bQ^2$  is replaced by a sum over all pairs of modes,  $\sum_{ij} b_{ij}Q_iQ_j$ , and we lose the great simplification of section 7.1 that the modes are independent of each other. One effect of the frequency changes is to make the energy of the zero-phonon line depend on the mass of the isotopes at the centre. The energy change between isotopes I and II is

$$\begin{aligned} \hbar\nu_I - \hbar\nu_{II} &= \frac{1}{2} \sum_i [(\hbar\omega_i^e - \hbar\omega_i^g)^I - (\hbar\omega_i^e - \hbar\omega_i^g)^{II}] \\ &= \frac{1}{2} \sum_i (\hbar\omega_i^e - \hbar\omega_i^g)^I [1 - (m_{iI}/m_{iII})^{1/2}]. \end{aligned} \quad (121)$$

As an example the 969 meV zero-phonon line shifts by +0.08 meV on replacing  $^{12}\text{C}$  by  $^{13}\text{C}$  [254]. With mixed  $^{12}\text{C}$  and  $^{13}\text{C}$  there are only two zero-phonon lines, indicating that these isotope effects arise from one carbon atom in the centre. The three degrees of freedom of that atom imply that there are only three terms of relevance in eq. (121). The local-mode sidebands also show carbon isotope shifts, indicating that mainly one C atom is vibrating in them. Assuming that all three modes have the same frequency shift (eq. 111) as the one known value, and with an effective mass change in the ratio  $(13/12)^{1/2}$ , eq. (121) predicts an isotope shift of 0.10 meV on replacing  $^{12}\text{C}$  by  $^{13}\text{C}$ , of the order observed.

Silicon isotope effects are also observed in the 969 meV zero-phonon line (fig. 48). From the relative intensities the isotope structure is characteristic of one Si atom. Again the sum in eq. (121) has a maximum of three terms relevant to this isotope effect. The change in effective mass on replacing  $^{28}\text{Si}$

by  $^{30}\text{Si}$  is at most  $(30/28)^{1/2} = 1.071$ . If we assign a “typical” phonon quantum of 30 meV to these modes, the mean frequency change between the ground and excited states for the three modes necessary to produce the observed isotope shift of 0.234 meV between  $^{30}\text{Si}$  and  $^{28}\text{Si}$  is (from eq. 121)

$$\hbar\omega_g - \hbar\omega_e \sim 4.6 \text{ meV}. \quad (122)$$

Since the Si atom does not vibrate in isolation, the frequency change is larger than this value. The magnitude is already larger than those in table 3, but the sign is the same. In the monoclinic I symmetry of the centre (point group  $C_{1h}$ ) atomic motion parallel to the principal axis cannot produce a sideband since the motion transforms as  $\Gamma 2$  (section 7.1). However, its frequency may differ in the two electronic states. The frequency of this mode is likely to be sensitive to the extent that the unique Si atom lies in the  $T_d$  interstitial position (fig. 47), when rotation about the [111] C–C axis becomes easy. It is possible that the frequency of the  $\Gamma 2$  mode is very sensitive to the electronic state, and it alone may account for the total zero-phonon Si isotope effect.

Quadratic electron–phonon coupling makes the peak energy and the width of the zero-phonon line vary with temperature. The mean energy in a mode of frequency  $\omega$  is, from eq. (5),  $[n(\omega) + \frac{1}{2}]\hbar\omega$ . The zero-phonon energy varies with temperature  $T$  as

$$h\nu(T) - h\nu(0) = \sum_i n(\omega)(\hbar\omega_i^e - \hbar\omega_i^g), \quad (123)$$

the sum being over all the modes of the optical centre. In addition, as  $T$  increases from zero the lattice first contracts and then expands (section 2.1). If the change in energy per unit hydrostatic compressive stress is  $A$ , the lattice expansion  $D(T)$  gives a shift

$$\Delta h\nu(T) = -A(c_{11} + 2c_{12})D(T). \quad (124)$$

The total shift is the sum of eqs. (123) and (124). Because  $A$  is the energy change per unit stress applied externally on the crystal,  $c_{11}$  and  $c_{12}$  are the known elastic constants of the *bulk* crystal (eq. 2), not the unknown constants near the centre as in eq. (106). It is useful to define a function

$$g(\omega) = \sum_i (\hbar\omega_i^e - \hbar\omega_i^g)\delta(\omega - \omega_i), \quad (125)$$

so that  $g(\omega)d\omega$  is the total change in quanta for all the modes with frequencies  $\omega$  to  $\omega + d\omega$  in the ground electronic state. Equation (123) is then

$$h\nu(T) - h\nu(0) = \int d\omega g(\omega)n(\omega). \quad (126)$$

There is no direct connection of  $g(\omega)$  to the one-phonon sideband  $P_1(\omega)$ , eq. (104). However, for long wavelength modes [255]

$$g(\omega) = c\omega^n P_1(\omega), \quad (127)$$

where  $n \sim 2$  and  $c$  is independent of  $\omega$ . We extend this form to all frequencies. The magnitudes of the

phonon-induced shifts are similar at all centres in silicon, e.g. 789 and 969 meV [90], 1018 meV [202] and the 488 meV zero-phonon line, fig. 65b. From the fit, eqs. (121) and (125) imply that if all the Si atoms in the lattice were changed from  $^{28}\text{Si}$  to  $^{29}\text{Si}$  so that  $m_{ii'}/m_{ii} = 29/28$  for all modes, the 488 meV zero-phonon line would shift by +0.12 meV, with a variation by a factor of 3 either way as  $n = 1, 2$  or 3, excluding the effect of the change in lattice parameter resulting from the isotope change [256]. (Similar estimates agree with the shifts in zero-phonon lines measured in  $^{13}\text{C}$  and  $^{12}\text{C}$  diamonds [13]). This produces a lower limit to the width of the zero-phonon lines (section 10.2).

As  $T$  increases the quadratic electron–phonon coupling increases the width of the zero-phonon lines. (Throughout, width means the total width at half the peak intensity.) The broadening  $\Gamma$  is caused by simultaneous absorption and emission of phonons, and has been given as [255]

$$\Gamma(T) \sim \int d\omega g^2(\omega)n(\omega)[n(\omega) + 1]. \quad (128)$$

This expression is not very successful (e.g. refs. [20, 257]). One problem is the very strong dependence of the integrand on  $\omega$  at high  $T$ . Small variations of  $g(\omega)$  can therefore result in substantial changes to the temperature dependence of  $\Gamma(T)$  and the fit in fig. 65c is particularly good. At low  $T$  a residual linewidth is always measured ( $\sim 0.1$  meV on fig. 65c). This is composed of instrumental broadening ( $\sim 0.03$  meV here), broadening by random strains ( $\sim 0.02$  meV produced by impurity oxygen plus an unknown component from the radiation damage, section 10.1), and intrinsic isotope effects ( $\sim 0.016$  meV, section 10.2). The broadening processes are all independent of each other. The total lineshape is therefore the convolution of all these effects. In practice the width is usually taken to be the arithmetic sum of the widths of each component, although this would be strictly accurate only if each lineshape was Lorentzian.

## 8. Electronic states

Many photoluminescence centres in silicon have excited states whose properties can be related to the valence and conduction band extrema; this is demonstrated here by three examples.

First, the 789 meV centre has excited states which are derived from the donor-like states of an electron orbiting the positively charged core of the centre. This core is composed of the neutral C + O complex (section 5.1) plus a tightly bound hole, and the luminescence is produced by annihilation of the electron and hole. Figure 72 shows the effect of uniaxial compressions on the 789 meV line [177]. Stresses parallel to  $\langle 111 \rangle$  do not appreciably split the line, because the  $\langle 001 \rangle$  conduction band minima remain equivalent under this stress. The local (nearly tetragonal) symmetry of the 789 meV centre mixes the conduction band minima; the lines on fig. 72 are the calculated effects of stress on these mixed states [177]. The deformation potentials for the conduction bands must be reduced by 24% from their values for the perfect crystal (eq. 27) to fit the data.

A second example, with trigonal symmetry, is the 1045 meV centre (section 5.5). The  $\Gamma_3$  excited states are obtained by mixing the  $x, y, z$  conduction band minima in the form  $(2z - x - y)/\sqrt{6}$ , quenching the splitting under  $[001]$  stress to  $\frac{2}{3}$  the splitting of the conduction band minima. This is as observed on fig. 54:  $[001]$  stresses split the bound states by  $60 \pm 12$  meV/GPa,  $\frac{2}{3}$  that of eq. (27).

A final example is the 1040 meV line [258]. Here  $\langle 001 \rangle$  stresses produce a large splitting (117 meV/GPa) into two states which cannot come into thermal equilibrium until their separation exceeds

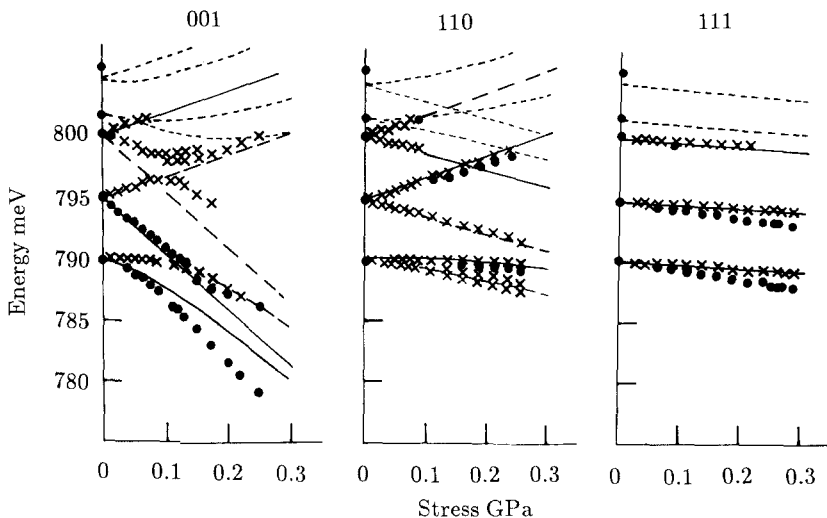


Fig. 72. Perturbations of the 789 meV zero-phonon line (and its nearby excited states) by uniaxial compressions applied along the 001, 110 and 111 axes. Points show the measured data [176], and the lines are calculated by the shallow donor model for the excited states [177].

$\sim 15$  meV. This is characteristic of conduction band splitting, as shown on fig. 18—simultaneous conservation of energy and wavevector implies that an electron in a “hot” conduction band minimum cannot de-excite to a “cold” minimum until it can emit a (17 meV) inter-valley scattering phonon (section 2.1).

In these three examples, the magnitudes of the splittings under stress of the conduction and valence bands (CB and VB) differ from the perfect crystal values (eqs. 25, 27) by a factor  $x$ :

$$\begin{aligned} &\text{for the } 789 \text{ meV line, CB states, } x = 0.76, \\ &\text{for the } 1040 \text{ meV line, CB states, } x = 1.25 \pm 0.06, \\ &\text{for the } 1045 \text{ meV line, CB and VB states, } x = 1.0 \pm 0.05. \end{aligned} \quad (129)$$

The 789 meV centre contains two interstitial atoms (section 5.1), making it harder to deform than the pure lattice ( $x < 1$ ). The 1040 meV line is produced by bombardment with neutrons or ions and possibly occurs at a vacancy cluster, consistent with  $x > 1$  (a “soft” local environment) [258].

The states here are evidently very similar to band extrema states, but they are sufficiently localised on the optical centres that they are affected by them. The Huang–Rhys factors  $S$  are also explicable in terms of localised centres (section 7.2);  $S$  for delocalised states with the same stress response, e.g. bound excitons, are considerably smaller. For an electron localised within a Bohr radius equal to one atomic spacing, the uncertainty in wavevector is  $\sim 35\%$  of the distance in  $k$  space from  $\Gamma$  to a  $\langle 001 \rangle$  zone boundary. Evidently the delocalisation is sufficient that a useful model of many centres is to represent the excited states by excitons bound to the centre by a local attractive potential.

The simplest representation of the attractive potential is by uniaxial strain. At some relatively shallow centres this strain has a physical justification in the strength of the phonon sideband. For example, at the 1045 meV band (fig. 53), the energy relaxation  $E_r = 100$  meV (eqs. 93, 102). In the single coordinate model, with a mean quantum  $\hbar\omega = 30$  meV and using the Si mass, this corresponds to an atomic relaxation  $Q_0 = 0.018$  nm, a strain of 0.077 along the trigonal axis of the centre (section 5.5).

This strain corresponds to a  $\langle 111 \rangle$  uniaxial stress of

$$S(\text{Li}) = 4.9 \text{ GPa} . \quad (130)$$

Thus the relaxation of the centre *observed* in the vibronic sideband is equivalent qualitatively to a considerable local deformation; eq. (130) is also justifiable quantitatively (eq. 131).

At an iso-electronic centre the excited state is regarded as containing one electron in an orbital singlet state constructed from the conduction band minima, and one hole in a state constructed from the valence band maxima. All other electrons and holes at the centre are assumed to be tightly bound and so can be ignored, in contrast to the shell model (section 4.3). The electron and hole can couple through their exchange energy, which is shown below to be  $\sim 1$  meV at relevant photoluminescence centres in silicon. Figure 73 shows the effect of a  $\langle 111 \rangle$  stress on these states calculated using the known stress response of the band extrema [67]; only the lowest exciton states are shown but the split-off valence band states were included in the calculation [259]. Because the valence band is orbitally degenerate, the distortion always allows an exciton to lower its energy, as long as the splitting exceeds any hydrostatic shift. The distortion is therefore driven by the decreased exciton energy, once the exciton has been weakly bound near the optical centre. Two cases occur:

(a) A compressive stress exerted by the optical centre on the lattice ( $S$  negative on fig. 73). At large stress the valence band's  $p_x$ ,  $p_y$ ,  $p_z$  states are split into a lower energy singlet (e.g.  $p_z$  for stress on  $\langle 001 \rangle$ ). The hole in this state has an angular momentum  $j = 1/2$  (from its spin) and couples with the  $s = 1/2$  electron to produce a lower energy  $S = 1$  triplet and a higher energy  $S = 0$  singlet, the  $Q_L$  and  $Q$  lines of the 1045 meV centre. Optical transitions from the  $S = 1$  state to the ground state (which contains no particles and hence has  $S = 0$ ) are forbidden in the limit of large  $S$ . The intensity ratio of the  $Q_L$  and  $Q$  lines therefore tends to zero as  $S_i \rightarrow -\infty$ , and the value of  $S_i$  for any centre can be estimated from the measured ratio. For the 1045 meV centre (fig. 74)

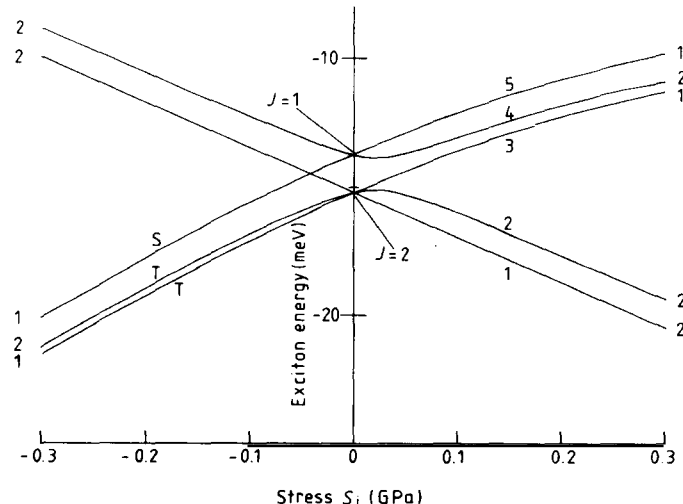


Fig. 73. The lower-energy states of an exciton bound to an iso-electronic centre, where the binding is represented by an equivalent  $\langle 111 \rangle$  stress  $S_i$ . For  $S_i < 0$  (compression of the lattice) the lowest states form a singlet-triplet pair (labelled S and T). For  $S_i > 0$  the degeneracy of the states is shown [259].

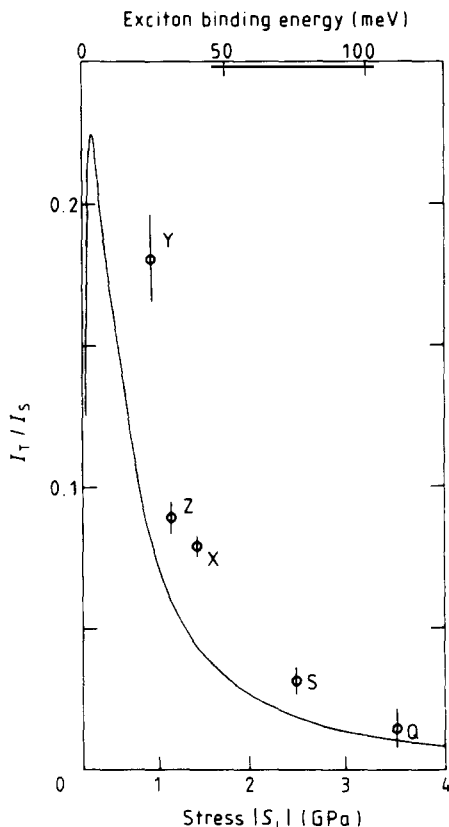


Fig. 74. Ratio of the transition probabilities of transitions from the singlet and triplet states of fig. 73, as a function of  $-S_i$ . The calculated binding energy is shown at the top. Data for five bands are shown, using the measured spectroscopic binding energies [259].

$$S_i = -3.5 \text{ GPa} , \quad (131)$$

in close agreement with the electron-phonon relaxation (eq. 130). The localisation energy of the exciton on the 1045 meV centre (100 meV, top scale, fig. 74) also therefore coincides with  $E_r$  for the centre. Consequently, the observed trigonal symmetry appears to be derived from the distortion of the centre which lowers the exciton energy. The exchange splitting between these states is the 1 meV spacing of the  $Q_L$  and  $Q$  lines (fig. 53). The splitting of the states in a magnetic field is predicted to be isotropic, as observed (fig. 75a). The effect of externally applied uniaxial stresses can be calculated explicitly (since the responses of the valence and conduction bands are known, section 2.1), and fits equivalent to fig. 54 result [259].

(b) An extension of the lattice created by a small optical centre (positive  $S_i$  on fig. 73). The low energy  $J=2$  exciton (created from the electron of spin 1/2 and the hole of  $j=3/2$ ) is split by the stress  $S_i$ , but the lowest energy state ("1" on fig. 73) always has parallel electron and hole spins. Consequently the Zeeman splitting of state "2" is large (fig. 75b) and transitions to the ground (spinless) state are forbidden (in the absence of an external perturbation). Transitions from state "2" are similarly forbidden when  $S_i = 0$  but increase in intensity at the expense of transitions from "3" and "4" with increasing  $S_i$ . For the 1122 meV "ABC" band the observed intensity ratios and energy spacings

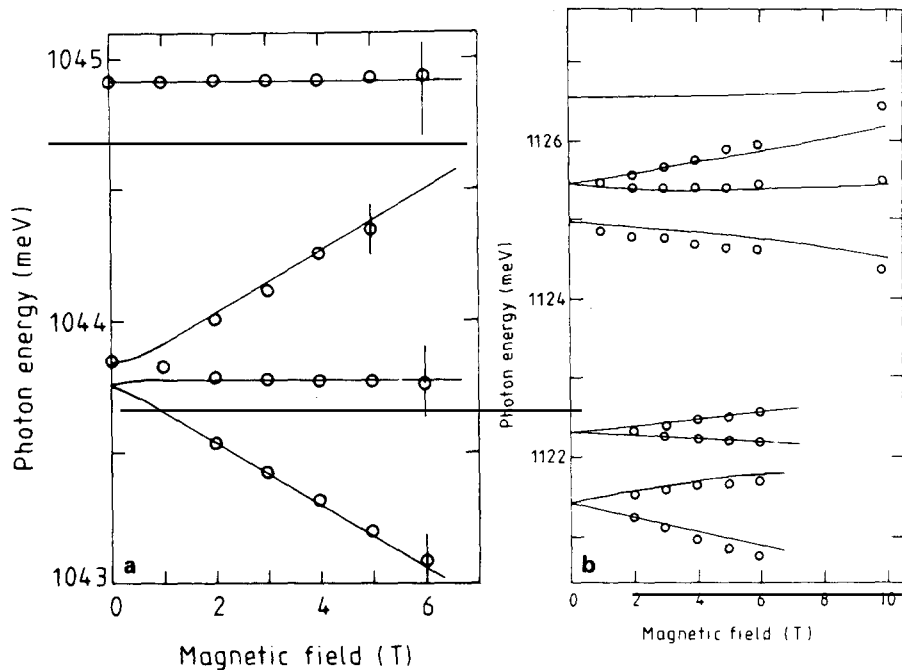


Fig. 75. Perturbations by  $\langle 001 \rangle$  magnetic fields of (a) the 1044, 1045 meV lines of the 4-Li atom complex, and (b) the 1122 meV lines of the Al-N complex. The lines are calculated as in section 8 [259].

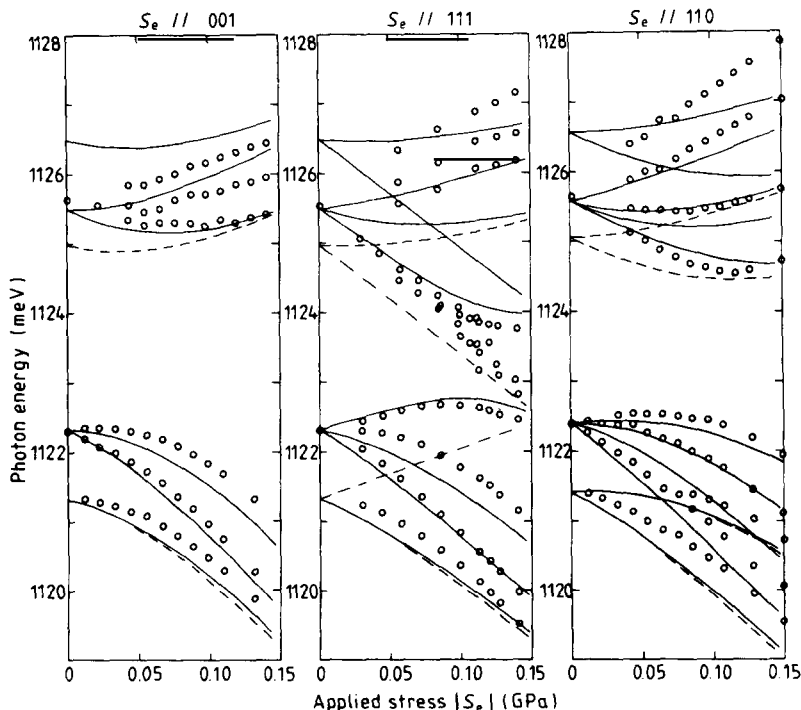


Fig. 76. Perturbations by externally applied uniaxial compressions  $S_e$ , as measured (points) and calculated using the model of section 8 [259].

of the lowest energy lines correspond to  $S_i \sim 0.1$  GPa. This is comparable with the magnitudes of stresses that can be applied externally, and so substantial mixing of the states occurs. The energies of the lines predicted from the model agree closely with experiment (fig. 76) when the deformation potentials are about 2/3 the perfect lattice values [259].

Some isoelectronic centres are capable of showing properties of both types of centre (with  $S_i > 0$  and  $S_i < 0$ ) in different electronic states. A Tl-related centre shows luminescence with a zero-phonon line "A" at 1088 meV at temperatures less than  $\sim 15$  K. Uniaxial stress and magnetic field perturbations are consistent with the centre having  $C_{3v}$  symmetry with  $S_i > 0$  [260]. Above  $\sim 15$  K this spectrum is replaced by the "P" line at 1050 meV from a spin-triplet state characteristic of  $S_i < 0$  at a centre whose symmetry is lower than  $C_{3v}$  [260]. Time-resolved data show that the A line decreases exponentially with time (with a low temperature value of 53  $\mu$ s) after pulsed excitation. In contrast the intensity of the P line first increases and then decreases after sudden excitation [261]. These data suggest that the exciton is captured in the A configuration, and the centre can subsequently restructure into the P form. The barrier to be overcome between the configurations is 20 meV; the prefactor of the motion ( $\sim 10^{-12}$  s) is consistent with atomic vibrational motion. An In-related centre shows very similar behaviour [260].

For those photoluminescence centres where it is valid to construct the excited states from the band extrema, a considerable amount of data can be described in terms of a few parameters, whose magnitudes are approximately predetermined by the measured properties of the extrema. When a photoluminescence centre has a phonon sideband indicating an energy relaxation  $E_r$ , and the energy of the zero-phonon line is less than  $E_r$  below the free exciton energy (1156 meV as  $T \rightarrow 0$  K, section 2.2), the excited state is stabilised by the electron-phonon relaxation. We can picture the exciton as trapped at the optical centre in a strain field which is caused by the centre deforming so as to lower the exciton's energy.

## 9. Closely related photoluminescent centres

Some photoluminescence centres (e.g. the 767 and 789 meV centres) have very similar properties for reasons not yet investigated; others (e.g. the 1045 meV (section 5.5) and 1082 meV [211] centres) are similar because the basic (1045 meV) centre has an extra carbon atom attached. In sections 9.1 and 9.2 two larger "families" of photoluminescence centres are discussed.

### 9.1. Centres like the 969 meV centre

Radiation damage created with the silicon between 0 and 200°C produces the 969 meV band. Each 969 meV centre is formed when one interstitial carbon atom is trapped at a substitutional carbon atom (section 5.2). Beyond a particular dose, a further increase of the dose decreases the concentration of 969 meV centres (section 5.2.1). In this dose regime four zero-phonon lines appear at 951.2, 953.0, 954.0 and 959.6 meV. The responses of these lines and the 969 meV line to uniaxial stresses are all very similar [254] (and these responses are not characteristic of band states). Additional similarities between the lines are their silicon isotope structure (table 4) and their local-mode sidebands, which all have similar energies and isotope dependences (table 3). With increasing radiation dose these four lines all eventually decrease (fig. 77).

Since the 969 meV centres are destroyed with increasing dose by capture of a self-interstitial I, one possible explanation of the four related lines is that they occur at the new complexes of 969 meV plus

Table 4

Isotope shifts of zero-phonon lines. The table lists the difference in the energies of zero-phonon lines between silicon doped with a heavy isotope and a light isotope.

Line (meV)	Name	Element	Heavy isotope	Light isotope	Shift (meV) heavy – light	Ref.
488		C	13	12	-0.09 ± 0.01	[240]
488		O	18	16	-0.12 ± 0.01	[240]
746	N1	C	13	12	-0.043 ± 0.007	[274]
746	N1	N	15	14	0.021 ± 0.003	[274]
758	N2	C	13	12	-0.067 ± 0.007	[274]
758	N2	N	15	14	0.015 ± 0.003	[274]
760.6	M	C	13	12	-0.05	[78]
762	N3	C	13	12	-0.064 ± 0.007	[274]
767	N4	C	13	12	-0.059 ± 0.003	[274]
767	P	C	14	12	0.17 ± 0.05	[169]
769		C	14	12	0.20 ± 0.02	[169]
772	N5	C	13	12	-0.051 ± 0.007	[274]
789		C	14	12	0.17 ± 0.01	[169]
875		C	13	12	0.15	[271]
916		O	18	16	0.05 ± 0.01	[272]
920		C	14	12	0.25 ± 0.02	[169]
924		O	18	16	0.18 ± 0.03	[272]
925.5	H	C	14	12	0.235 ± 0.015	[169]
928.6		C	14	12	0.21 ± 0.02	[169]
929		C	14	12	0.23 ± 0.02	[169]
935.1	T	C	13	12	0.07	[78]
950		C	14	12	0.22 ± 0.02	[169]
951		C	13	12	-0.1	[254]
951		Si	30	28	0.21	[254]
953		C	13	12	-0.04	[254]
953		Si	30	28	0.31	[254]
954		C	13	12	0	[254]
954		Si	30	28	0.27	[254]
957		C	13	12	0	[254]
957		Si	30	28	0.27	[254]
969	G	C	13	12	0.08	[254]
969	G	Si	30	28	0.23	[254]
1018	Cu	Cu	65	63	0.06	[200]
1037		Li	7	6	-0.5 ± 0.1	[239]
1045	Li	Li	7	6	0.98 ± 0.03	[11]
1082	LiC	Li	7	6	1.0	[211]
1116.9	NL1	B	11	10	0.15	[277]
1117	X	Li	7	6	0.25 ± 0.02	[273]
1126	Z	Li	7	6	0.24 ± 0.02	[273]
1131	Y	Li	7	6	0.22 ± 0.02	[273]

one or more I's. Using the radiation damage model of section 6.5 the concentration of 969 meV centres plus one I may be calculated. Since the four new centres are so similar to the 969 meV centre, we must assume that they all have the same oscillator strengths. The predicted absorption in the four lines is then an order of magnitude larger than observed [231]. However, a similar form is predicted for the absorption in the lines as a function of dose (fig. 77). With increasing dose the absorption in the 969 meV plus I complex would increase at a rate determined by the carbon concentration, reaching a

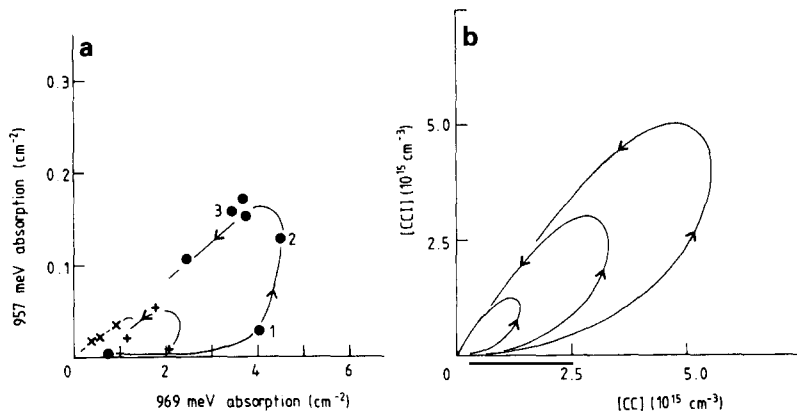


Fig. 77. Data in float-zone silicon for the 957 and 969 meV lines produced by irradiation at 100°C with 2 MeV electrons. (a) Measured data in three samples with increasing carbon content (in the order  $\times$ ,  $+$ ,  $\bullet$ ) as the radiation doses increase (sequence following the arrows). (b) The similar shape of curves calculated with the model of section 6.5 for the concentrations of 969 meV ("CC" centres and (CC) + one self-interstitial [211].

maximum and then decreasing down the same line for all carbon concentrations (fig. 77). This is the form of the dose dependence observed for the four lines, but we have seen that the data are quantitatively in disagreement.

The inconsistency is removed if we postulate that the four new centres are 969 meV centres with a self-interstitial trapped "near" (but not "at") the 969 meV centre. This model is confirmed by fig. 45, which shows a silicon sample irradiated below room temperature, so that all the self-interstitials have been converted to carbon interstitials (section 6.3). Annealing at 50°C then generates the 969 meV centres, but there are no free self-interstitials to form the four related centres, despite the relatively large radiation dose given to this sample.

There appears to be no sharp-line photoluminescence from 969 meV (or 789 meV) centres when they have captured self-interstitials. The disappearance of a luminescence signal is one limitation of photoluminescence spectroscopy.

### 9.2. Centres like the 1018 meV centre

Fast neutron damage, followed by annealing at 150°C, produces the 1018 meV "W" centre (section 5.4). Bombardment with the inert gas ions He, Ne, Ar and Kr produces vibronic bands of very similar shape, and with similar zero-phonon energies (1012 meV for He, 1014 meV for Ne, 1009 meV for Ar and 1004 meV for Kr [203]). They also have similar responses to uniaxial stresses, and all the centres have trigonal symmetry [262–264]. Bombardment with Xe produces an apparently different type of centre with tetragonal symmetry [264].

We take the cases of He, Ne, Ar and Kr first. Evidently they produce W centres which are perturbed by the presence of the inert gas atom. Inert gas atoms are chemically inert, so that the perturbation will not arise from chemical bonding (as suggested in ref. [263]). A more probable cause is the strain field created by an inert atom trapped near a W centre. Suppose that the inert atom replaces one substitutional Si atom located along the trigonal axis of the centre (to maintain the same symmetry, as observed in uniaxial stress measurements). The W centre is then perturbed by (a) the removal of the Si atom, which is assumed to introduce a shift  $E_s$ , and (b) the stress  $S$  exerted on the W centre by the

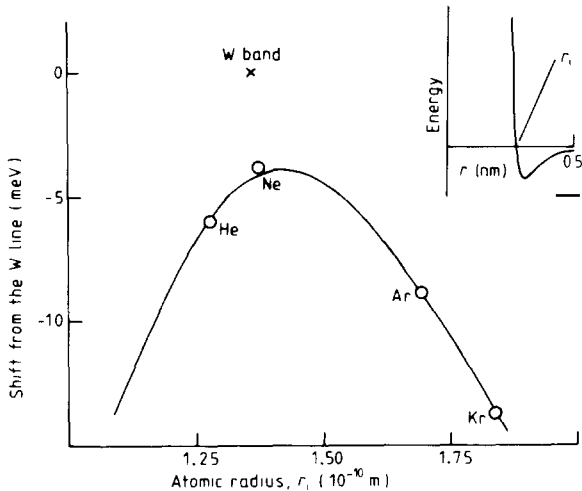


Fig. 78. Points show energies of the W-like zero-phonon lines plotted as a function of the radii  $r_i$  of the inert gas atoms ( $r_i$  defined in the inset). The line is the calculated shift stress-induced by the atoms [202].

vacancy plus the trapped inert atom.  $S$  is proportional to the misfit between the inert atom (radius  $r_i$ ) and the Si atomic radius ( $r_s$ ),

$$S = c(r_i - r_s). \quad (132)$$

The inset on fig. 78 defines the radius of the inert atom as half the distance between two identical inert atoms when they have zero interaction energy, representing the onset of the hard core potential of the atom. The line on fig. 78 shows the energy of a W-like zero-phonon line calculated using its known stress response and modelling the perturbation by a uniaxial stress along the  $\langle 111 \rangle$  trigonal axis of the centre [202]. The silicon radius  $r_s$  has a best fitting value of 0.136 nm, close to half the Si–Si bond length (0.234 nm), the static shift  $E_s = -4.3$  meV, and  $c = 1.1 \times 10^{11}$  GPa/m. This corresponds in elastic continuum theory (section 10.1) to the inert atom being located  $\sim 0.3$  nm along the trigonal axis from the W centre [202]. The inert gas atom is then sufficiently close to the W centre that it will be stable in a unique site, producing the observed characteristic perturbation of the W centre. Applied to Xe, with  $r_i = 0.2035$  nm, the zero-phonon line is predicted at 994 meV; the observed value for this possibly different type of centre is 1000 meV [203].

The unique response to stresses of the W line ensures that it is perturbed to lower energy both by an extension of the lattice (a negative stress on fig. 52), and also by a large enough compression (fig. 52), so that both He and Kr atoms produce lines at lower energies than Ne.

## 10. Widths of zero-phonon lines

### 10.1. Stress-induced widths

Zero-phonon lines in silicon typically have full widths at half height of 0.1 meV, in the limit of low temperature. This width is not intrinsic to the transition—for example, lifetime broadening for the

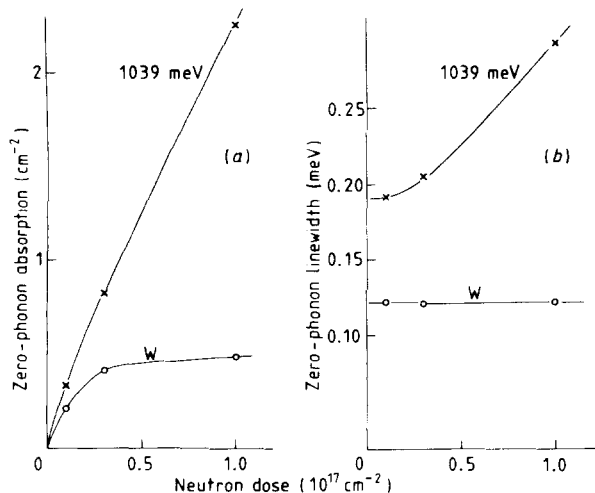


Fig. 79. Measured intensities and full widths at half height of the 1018 meV "W" and 1039 meV lines produced by fast neutron damage [202].

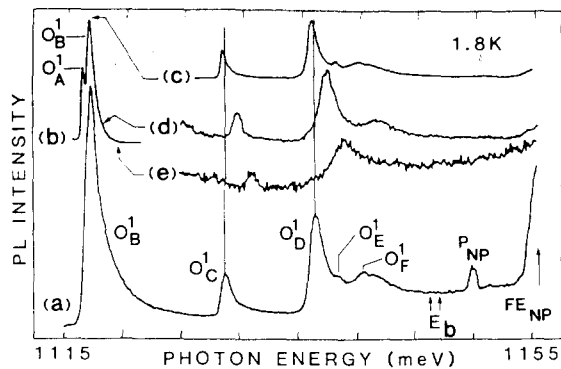


Fig. 80. (a) Luminescence excitation spectrum of the "O" series of lines. (b) Sequence c, d, e shows luminescence excitation detected at different parts of the main  $O_B^1$  line. The shifts in the  $O_C^1$ ,  $O_D^1$ , ... lines confirm the inhomogeneous broadening of the lines [147].

969 meV line is  $\sim 10^{-7}$  meV (using a lifetime of 4  $\mu\text{s}$ , table 1). The linewidth is a useful monitor of the state of the crystal—any strain resulting from a crystal being mounted badly in a cryostat is seen most obviously from the width (and shape) of the zero-phonon lines. Similarly, linewidths give information about the microscopic regions of the crystal which contain the optical centres. Figure 79 shows the widths of two lines produced by neutron damage and annealing at 525 K for 30 min to maximise the lines. The width of the 1039 meV line increases with neutron dose, suggesting that this centre occurs in the heavily damaged regions, while the 1018 meV line has a constant width suggesting that it results from a defect which has migrated from the heavy damage clusters.

One identifiable component of the width comes from the inhomogeneous distribution of strains through the crystals [265]. Photoluminescence centres in different parts of the silicon experience different strains, and so have zero-phonon transitions at slightly different energies. The observed line is the sum of all the differently perturbed lines occurring at each centre. A superb demonstration of inhomogeneous broadening is in fig. 80 [147], which shows photoluminescence excitation measurements on a series of excited states ( $O_C^1$  to  $O_F^1$ ) of an optical centre. The lines are asymmetrically broadened; detection of the luminescence at different points in the  $O_B^1$  line (fig. 80c, d, e) shows the  $O_C^1$  to  $O_F^1$  lines to occur at different energies because the excitation energy is trapped within the differently perturbed centres.

Figure 81 shows that the width of the 969 meV line increases in proportion to the radiation dose. In the limit of zero dose the width is larger in Czochralski than in float-zone samples. The difference

$$W(\text{CZ}) - W(\text{FZ}) = 0.03 \pm 0.005 \text{ meV} \quad (133)$$

is presumably caused by the large concentrations ( $\sim 10^{18} \text{ cm}^{-3}$ ) of oxygen in CZ silicon, which expands the lattice (eq. 55). The strain field produced by an atomic sized defect is most simply represented as a spherically symmetric displacement  $u$  in a lattice continuum such that [266]

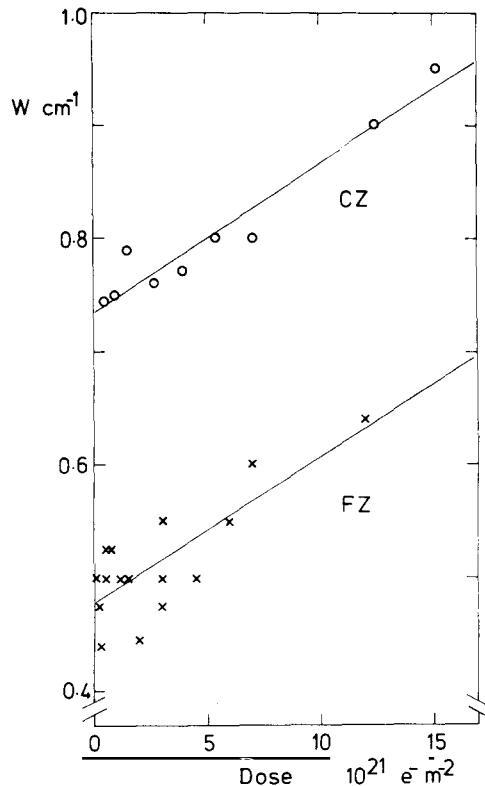


Fig. 81. Full widths at half height of the 969 meV absorption line as measured at 2 K in a set of float-zone and Czochralski samples irradiated with 2 MeV electrons.

$$u = A/r^2 \quad (134)$$

at a distance \$r\$ from the defect. A defect at coordinates \$x\_1, x\_2, x\_3\$ then gives strains at an optical centre at the origin of the coordinates with tensor components

$$e_{ij} = (A/r^3)(\delta_{ij} - 3x_i x_j/r^2).$$

To obtain \$A\$ we note that in a finite crystal

$$\Delta V/V = 12\pi Ap(1 - \sigma)/(1 + \sigma), \quad (135)$$

where \$p\$ is the density of defects, \$\sigma\$ is Poisson's ratio, and \$\Delta V/V = 1.2 \times 10^{-5}\$ at \$[\text{O}] = 10^{18} \text{ cm}^{-3}\$ (eq. 55). Since the largest responses of the 969 meV line are to \$s\_{zz}\$ and \$(s\_{xx} + s\_{yy})\$ stresses we use Poisson's ratio for \$\langle 001 \rangle\$ stresses (eq. 3). To calculate the shape of a zero-phonon line it is usual to assume that the optical centres and the strain sources are randomly distributed in the crystal [267]. The linewidth produced by the random distributions is a function of \$p\$ and the known effect of strain on the transition, and can be evaluated easily [268]. We find for the 969 meV line, when \$[\text{O}] = 10^{18} \text{ cm}^{-3}\$,

$$W = 0.018 \text{ meV}. \quad (136)$$

This is slightly less than the experimental value of eq. (133), probably because of the spatial correlation of the oxygen atoms producing the strain and the 969 meV centres. There is then a higher local concentration of strain centres near the optical centres than would be expected from random distributions of the defects. This spatial correlation is well known, for example from the formation of C-O pairs during growth [57].

In this example all the parameters in the calculation are known and so the width can be calculated explicitly. The 969 meV line is also broadened by the effects of radiation damage, the increase being the same in float-zone and Czochralski silicon (fig. 81), despite the different defects created in these crystals by electron irradiation (section 6). Assuming again that the effect is from the strain fields of damage clusters which can be represented as point strain sources, the increase in width is proportional to  $Ap$  for a particular optical transition. The increase for the 969 meV line, 0.016 meV at  $10^{18} \text{ cm}^{-2}$  2 MeV electron dose (fig. 81), implies that the volume expansion produced by the damage would be

$$\Delta V/V = 1 \times 10^{-5} \quad \text{at } 10^{18} \text{ cm}^{-2} \text{ 2 MeV electrons.} \quad (137)$$

Direct measurements of the increase in lattice parameter by X-ray diffraction give less than  $2 \times 10^{-6}$  [269]. The discrepancy with eq. (137) and the equality of the broadening in float-zone and Czochralski silicon are worth further investigation.

### 10.2. Isotope-induced widths

There is still a measurable linewidth remaining in the limits of low oxygen (e.g. float-zone silicon) and low radiation dose (fig. 81). For the 969 meV line the width  $W_0$  after correction for the resolution of the spectrometer ( $\sim 0.04$  meV) is

$$W_0 = 0.02 \text{ meV.} \quad (138)$$

It is likely that this width is caused by the mixed isotope nature of the lattice (eq. 1). This is suggested by the asymmetric form of many zero-phonon lines, with the high energy side being the broader (e.g. fig. 29). In a few cases discrete structure caused by the mixed isotopes breaks out of the line (e.g. the 969 meV line, fig. 48).

If all the Si atoms in a crystal were changed from  $^{28}\text{Si}$  to  $^{29}\text{Si}$  (with no change in the lattice volume) a typical zero-phonon line would move by  $D = +0.12$  meV to higher energy, with an uncertainty of a factor of 3 either way (section 7.5). To estimate the effect of the mixed isotopes we first note that a vibronic band involves tens of observable modes. For example, the 856 meV band (fig. 81) shows several sharp resonances. Taking the width of a resonant phonon as 1 meV implies at least  $\sim 65$  modes in the band. Because the selection rules for a phonon appearing in a sideband are more restrictive than the rules for a phonon producing an isotope shift, a considerable number  $N$  of atoms can be involved in producing isotope shifts, where  $N$  is several tens. The exact value is not critically important, and the structure of the centre is unimportant if we make the following simple assumptions. In the  $N$  atoms near the centre the numbers of  $^{28}\text{Si}$ ,  $^{29}\text{Si}$  and  $^{30}\text{Si}$  atoms are given by random distributions with the mean values of eq. (1). A single  $^{29}\text{Si}$  atom produces a shift ( $D/N$ ) and one  $^{30}\text{Si}$  atom produces twice the shift (since this proportionality is observed in the discrete isotope structure, fig. 48). Similarly the total shift from the energy of the 969 meV line in a pure  $^{28}\text{Si}$  lattice caused by  $p$   $^{29}\text{Si}$  and  $q$   $^{30}\text{Si}$  atoms is  $pD/N + 2qD/N$ . Evaluation with  $D = 0.12$  meV gives the full width at half height as  $W_0 = 0.016$  meV, in close agreement with eq. (138).

## Acknowledgement

The original research in this review was supported by the Science and Engineering Research Council.

## Appendix. Published photoluminescence and related electronic transitions in bulk crystalline silicon

Transitions are listed by their zero-phonon energies at 4 K. Luminescence lines are denoted L. Absorption lines are denoted A. Photoluminescence excitation lines are denoted PLE. Characteristic phonons are listed; TO: transverse optic, TA: transverse acoustic, G:  $k = 0$  optic. The names assigned to transitions are shown as "1F". Assignment of a transition to an impurity implies that the assignment is unambiguous, e.g. by isotope effects. References indicate useful sources of data, and are not intended to be comprehensive.

Energy (meV)	Mode	Phonons (meV)	Model
1152.5	L		Zero-phonon emission from modified 1094.5 meV F centre; "1F" [143]
1152	L		Zero-phonon emission from modified 1094.5 meV F centre; "2F" [143]
1150.7	L	TO = 58	B bound-exciton zero-phonon line [278]
1150.1	L	TO = 58	Sb bound-exciton zero-phonon line [157]
1150.0	L	TO = 58	P bound-exciton zero-phonon line; multi-bound-exciton lines involving $m$ excitons at $m = 2$ : 1146.5; $m = 3$ : 1143.7; $m = 4$ : 1141.7; $m = 5$ : 1140.5; $m = 6$ : 1139.3 meV [153, 157, 278]
1149.6	L	TO = 58	Al bound exciton zero-phonon line; multi-exciton zero-phonon lines for $m$ excitons at $m = 2$ : 1146.3; $m = 3$ : 1143.7; $m = 4$ : 1141.5; $m = 5$ : 1140.3 meV [157]
1149.2	L		As bound-exciton zero-phonon line [157]
1149.0	L	TO = 58	Ga bound-exciton zero-phonon line [153]
1148.8	L		Zero-phonon emission at P donor, associated line at 1147.9 meV; "a1" and "a2" [157]
1146.9	L	TA = 19	Bi bound-exciton zero-phonon line [154]
1143	L	TA = 19, TO = 58	"TD" produced in CZ Si by heating at 450°C [5]
1142.2	L		H <sup>+</sup> implantation and anneal 450–600°C [279]
etc.			
1141.0	L	TO = 58	In bound-exciton zero-phonon line
1132.6	L		Li bound-exciton line with TA emission [280]
1131	L		Radiation damage in Si:Li; "Y" [259]
1129.9	L		Emission from multi-bound excitons at Li donor involving two excitons; similar multi-exciton emission involving $m$ phonons at $m = 3$ : 1127.8; $m = 4$ : 1125.9; $m = 5$ : 1124.5; $m = 6$ : 1123.2 meV [278, 281]
1126	L		Radiation damage in Si:Li; "Z" [259]
1122	A, L		Trigonal isoelectronic centre involving N + Al? Shallow h <sup>+</sup> with pseudo-acceptor binding energy 36.7 meV; "ABC" [259]
1117.6	L	G = 66	"O <sub>1</sub> ", one of a series, O <sub>2</sub> = 1115.6, O <sub>3</sub> = 1113.7, O <sub>4</sub> = 1111.8 meV; thermally induced in CZ Si; asymmetric lineshape suggesting bound-to-free transition (?) or strain broadening (?) [282]
1117.5	L, PLE	9.2	Monoclinic II, In-related; associated lines at 1115.9, 1108.5 meV; "PQR" of In [283]
1117	L		Radiation damage of Si:Li; "X" [259]
1117	L		Isoelectronic centre involving Be + C [252]
1116.9	L		Strongest of 3 lines at 1116.1, 1116.9 and 1119.3 meV observed after B implantation and 10 min at 450°C; "NL1"; B isotope dependence [277]
1108.3	L		First in the series of "S" lines of which the other main lines are at 1104.6, 1100.5, 1092.7, 1090.5, 1088.1, 1085.5, 1070.4, 1067.2, 1060.8, 1034.2, 1023.4, 1014.4 meV; formed in CZ Si by 100 h at 500°C [144]
1108.1	L		Centre produced in FZ Si by neutron irradiation and anneal at 250°C [192]

Energy (meV)	Mode	Phonons (meV)	Model
1107.2	L	17	Luminescence from Si after laser annealing; "D1"; excited state transitions at D2: 1108.2; D3: 1108.7; D4: 1109 meV [284]
1100.6	L		Radiation damage centre produced by $\text{He}^+$ , $\text{H}_2^+$ , proton bombardment [279]
1095	L		TO phonon sideband emission of exciton bound to modified 1094.5 meV F centre; multi-bound-exciton emission from $m$ excitons at $m = 2$ : 1092; $m = 3$ : 1090; $m = 4$ : 1088.5 meV; "3F" [143]
1094.5	L		TO phonon sideband emission of exciton formed in CZ Si with $[\text{C}] > 5 \times 10^{16} \text{ cm}^{-3}$ after heating; multi-bound-exciton emission from $m$ excitons at $m = 2$ : 1092.5; $m = 3$ : 1090; $m = 4$ : 1088.5; $m = 5$ : 1087 meV; "F" [143]
1094.5	L		TO phonon sideband emission of exciton bound to modified 1094.5 meV F centre [143]
1093.2	L		Emission from exciton bound to Li donor with TO phonon creation [281]
1092.7	L		Emission from exciton bound to B acceptor with TO phonon emission; multi-exciton emission involving $m$ excitons at $m = 2$ : 1090.4; $m = 3$ : 1088.1; $m = 4$ : 1086.5 meV [278]
1091.9	L		Sb bound-exciton with TO emission [154]
1091.8	L		P bound-exciton and TO emission; similar multi-exciton lines involving $m$ excitons at $m = 2$ : 1088.2; $m = 3$ : 1085.6; $m = 4$ : 1083.7 meV [154]
1091	L		As bound-exciton and TO emission [154]
1090.0	L		Multi-bound exciton emission involving 2 excitons on Li donor and TO phonon creation; similar multi-exciton emission involving $m$ excitons at $m = 3$ : 1088.5; $m = 4$ : 1086.8; $m = 5$ : 1085; $m = 6$ : 1083.8; $m = 7$ : 1082.5; $m = 8$ : 1081.1 meV [281]
1086.9	L		Tl related lines, low $T$ version ( $T < 20$ K); associated lines at 1081.5, 1080.4 meV [260]
1082	A, L		Radiation damage of Si:(C + Li) and anneal at 300°C; very similar to 1045 meV; "S" [211]
1081.1			Observed in B-implanted Si after 400°C anneal [192]
1080	L	30.2, local	Monoclinic I centre produced by B implant or electron irradiation of Si:B; involves two B atoms; local modes 11B = 104.6, 10B = 109.4 meV; "I2" [78]
1076	L		Si:Be isoelectronic centre; trigonal? [259]
1067.2	L		One of the S series—see 1108.3 meV line [144]
1062.5	L		Produced by neutron irradiation and 300°C anneal of CZ Si [237]
1060	L		Radiation damage at 100 K in high C, high O [65]
1052	L		"O1"'; one of a series of 3 asymmetric lines produced by heating CZ Si for 130 h at 500°C; "O2'" at 1048, "O3'" at 1042 meV [148]
1050.2	L		Ga-related radiation damage centre; singlet line of singlet-triplet pair, triplet at 1047.2 meV; "Ga-2" [285]
1050.1	L		Tl-related lines observed at $T > 15$ K; other lines at 1048, 1042.7 meV; "Tl PQR" [260]
1049	L		Radiation damage of Si:Ga and anneal at 250°C [285]
1045	A, L	32.2, 47.9, 55.1	Radiation damage of Si:Li; trigonal centre of 4 Li atoms (at vacancy?); singlet line of singlet-triplet pair, triplet at 1044 meV; excited state at 1048 meV; "Q"; see section 5.5 [207, 211]
1039.8	L		Ion implantation, neutron damage and anneal at 500 to 800 K; tetragonal A to A or tetrahedral A to T transition; "I3" or "X" [192, 202]
1037	L		Produced by ion bombardment
1034.2	L		One of the S series—see 1108.3 meV S line [144]
1025	L		Produced in electron-irradiated FZ Si:Li and 450°C anneal [193]
1023.4	L		One of the S series—see 1108.3 meV S line [144]
1018.9	A, L	TA = 18, sharp resonances at 22, 51, 56, 60, local at 70.3	Ion implantation (or similar) damage line; trigonal centre, A to A transition; "II" or "W"; see section 5.4 [258]
1014.8	L		Line like 1018.3 meV W, but produced by Ne implantation; see section 9.2 [203, 258]
1014.7	L	7	Cu-related trigonal centre; see section 5.3 [199, 200]
1014.4	L		One of the S series—see 1108.3 meV S line [144]
1012	L		Line like 1018.3 meV W, but produced by He implantation; see section 9.2 [203, 258]
1010.3	L	15	See 707 meV
1009.7	L		Line like 1018.3 meV W, but produced by Ar implantation; A to A transition at trigonal centre; see section 9.2 [203, 258]

Energy (meV)	Mode	Phonons (meV)	Model
1004.8	L		Line like 1018.3 meV, but produced by Kr implantation; see section 9.2 [203, 258]
1003.7	L		Rhombic I centre produced by neutron irradiation and 400°C anneal in CZ Si
1000	L		Produced by Xe implantation; see section 9.2 [258]
997	L		Dislocation-related centre; "D4" [71]
990 ± 10	L		Ion implantation damage and hydrogenation [286]
996.8	L		Produced by neutron irradiation and anneal at 150°C [192]
988.8	L		Produced by neutron irradiation and 375°C anneal [192]
977.8	L, A		Observed in S-doped Si [73]
969.5	A, L, P	72	Monoclinic I centre involving two C and one unique Si atom; "G"; see section 5.2 DLTS, ODMR
967.4	L		Produced by neutron irradiation and anneal at 150°C [237]
965.2	L		Produced by 450°C heating of CZ Si; "I" [287]
957	L		Produced in CZ Si by 180 h at 450°C or by irradiation damage below 200°C?; same centre? [237, 288]
956.9	L		Perturbed form of 969 meV G; see section 9.1 [254]
953.9	L		Perturbed form of 969 meV G; see section 9.1 [254]
953	L		Perturbed form of 969 meV G; see section 9.1 [254]
951.2	L		Perturbed form of 969 meV G; see section 9.1 [254]
949.9	L		C-related radiation damage centre; monoclinic I symmetry; "F" [169, 192]
947	L		Produced by radiation damage and 450°C anneal [175, 193]
944.8	L	10.3, G	Observed in Mn + Zn-doped Si; luminescence from excited state at 945.8 meV [289]
943.7	L	6.4	Observed after Cu diffusion; similar to 1014.7 meV Cu centre [290]; trigonal centre
939	L		Dislocation-related centre; "D3" [71]
935.2	L		Produced by radiation damage at 20°C in C-doped FZ
935.1	L	29.4, 66.3	Rhombic I centre involving C produced by radiation damage and anneal at 450°C; "T" [78]
929.1	L		C-related radiation damage centre [169]
929	L	59.4	$\langle 100 \rangle$ symmetry axis?; singlet of singlet-triplet system; "Ga3" [271]
926	L		Radiation damage and anneal at 250°C of Si:Ga
925.5	L	TA, 20, 63	Radiation damage and anneal at 450°C in CZ Si; monoclinic I centre with dependence on C; "H" or "K" [169, 291]
922.3	L		Produced by high T anneal involving Al? + C? [145]
919.8	L		Radiation damage centre involving C [169]
903	L, ODMR		Produced by 300–400 h at 450°C in CZ Si; monoclinic I centre; "9" [287, 292]
897.9	L		Produced by radiation damage of CZ Si and anneal at 350°C [237]
878	L		Produced by radiation damage and anneal at 100°C of Si:Li [193]
875	L	55.8	Radiation damage of Si:Ga involving C in a rhombic I centre; "Ga1" [293]
874	L		Dislocation-related tetragonal centre; "D2" [71]
856	A		Rhombic I radiation damage centre produced in Si:C at $T < 300$ K; thermally destroyed at $T > 300$ K; no C isotope data but unambiguously interstitial C atom; see section 4.1.2.
844	L	14, G	Observed after Cr diffusion into Si:B [294]
836	L		Rhombic I radiation damage centre produced in Si:Al; "Al 1" [78]
829.8	A	15	Au-related centre?
811.1,	L	resonances	Produced by Pt(?) diffusion at 1150°C; rhombic I centre
810.5		at 7.2, 9.2, 16.5	
807	L		Dislocation-related tetragonal centre "D1" [71]
805.4	L, PLE	resonance at 15	Produced by Pt(?) diffusion at 1050°C; tetrahedral centre, T2 excited state, non-degenerate ground state
793.4,	L	3, 7	Au(?) associated [295]
793.0,			
792.8,			
791.9			
789.4	A, L	TA = 19, 65.5, 72.5, 138.1, 145	Monoclinic I radiation damage centre involving C and O; shallow donor e <sup>-</sup> state; "C"; see section 5.1
785	L		Produced by radiation damage and 300°C anneal of Si:Li [193]

Energy (meV)	Mode	Phonons (meV)	Model
775.1	L		Room temperature irradiation product with tetragonal symmetry(?) in Si:Al [296]
772.4			"N5"; see 745.6 meV N1 [297]
768.6	L		C-related radiation damage centre [169]
767.4	L		"N4"; see 745.6 meV N1 [297]
767.3	A, L	TA = 18, LA = 43, 65.6, 72	Monoclinic I C-related centre produced by radiation damage and annealing at 450°C in CZ Si; shallow effective mass-like e <sup>-</sup> with binding energy 34 meV; "P" [86, 169]
766.7	L		Produced by neutron irradiation and annealing at 375°C in CZ silicon [192]
761.5	L		"N3"; see 745.6 meV N1 [297]
760.6	L		Radiation damage centre involving C; "M" [78]
758	L		"N2"; see 745.6 meV N1 [297]
745.6	L	122.9, 71.3	Monoclinic I or trigonal centre involving N and C atoms; deep h <sup>+</sup> , shallow e <sup>-</sup> states; "N1" line; similar lines N2, ..., N5 [274, 297]
737.6,	L	resonances at 7.5, 10	Observed after Fe(?) diffusion [246, 270]
735.1,			
734.7			
707	A	15	Au-related centre?
677	L		Observed after Cr diffusion into Si:Ga [298]
567.9	L		See 564.7 meV
566.1			See 564.7 meV
565.7			See 564.7 meV
564.7	L	13, ~60	Mn-related(?) tetrahedral(?) centre [298]
488	A, L		Monoclinic I radiation damage centre involving C and O [240]

## References

- [1] P.McL. Colley and E.C. Lightowers, *Semicond. Sci. Technol.* 2 (1987) 157.
- [2] A.S. Oates, R.C. Newman, R. Woolley, G. Davies, E.C. Lightowers, M.J. Binns and J.G. Wilkes, *Appl. Phys. Lett.* 47 (1985) 705.
- [3] D.J. Robbins, D.B. Gasson, R.W. Hardeman and A.D. Pitt, in: *Proc. Symp. on Reduced Temperature Processing for VLSI* (Electrochem. Soc., Las Vegas, 1985) p. 159.
- [4] J. Weber, R.J. Davis, H-U. Habermeier, W.D. Sawyer and M. Singh, *Appl. Phys. A* 41 (1986) 175.
- [5] M. Tajima, S. Kishino, K. Kanamori and T. Iizuka, *J. Appl. Phys.* 51 (1980) 2247.
- [6] M.S. Skolnick, A.G. Collis and H.C. Webber, *J. Lumin.* 24/25 (1981) 39.
- [7] J.D. Cuthbert, *Phys. Rev. B* 1 (1970) 1552.
- [8] M.L.W. Thewalt, in: *Excitons*, eds E.I. Rashba and M.D. Sturge (North-Holland, Amsterdam, 1982) p. 393.
- [9] L.C. Kimerling, *Inst. Phys. Conf. Ser.* 31 (1977) 221.
- [10] K.M. Lee, K.P. O'Donnell, J. Weber, B.C. Cavenett and G.D. Watkins, *Phys. Rev. Lett.* 48 (1982) 37.
- [11] L.T. Canham, G. Davies, E.C. Lightowers and G.W. Blackmore, *Physica B* 117–118 (1983) 119.
- [12] G.S. Woods and A.T. Collins, *J. Phys. C* 15 (1982) L949.
- [13] A.T. Collins and G. Davies, *J. Lumin.* 40/41 (1988) 865.
- [14] G. Davies, *Chem. Phys. Carbon* 13 (1977) 1.
- [15] C.D. Clark, P.J. Dean and P.V. Harris, *Proc. R. Soc. London A* 277 (1964) 312.
- [16] B. Walter, *Ann. Phys. Chem.* 42 (1891) 505.
- [17] P.G.N. Nayar, *Proc. Indian Acad. Sci. A* 14 (1941) 1.
- [18] C.D. Clark, R.W. Ditchburn and H.B. Dyer, *Proc. R. Soc. London A* 234 (1956) 241, 361.
- [19] J. Walker, *Rep. Prog. Phys.* 42 (1979) 1605;  
for later work see, e.g., G. Davies, *J. Phys. C* 15 (1982) L149.
- [20] G. Davies, *Rep. Prog. Phys.* 44 (1981) 787.
- [21] M.I.B. Jorge, M.E. Pereira, M.F. Thomaz, G. Davies and A.T. Collins, *Port. Phys.* 14 (1983) 195;  
G. Davies, M.F. Thomaz, M.H. Nazare, M.M. Martin and D. Shaw, *J. Phys. C* 20 (1987) L13.
- [22] K. Godwod, R. Kowalczyk and Z. Szmid, *Phys. Stat. Sol. a* 21 (1974) 227.
- [23] J.S. Shah and M.E. Straumanis, *Solid State Commun.* 10 (1972) 2348;  
K.G. Lyon, G.L. Sangster, C.A. Swenson and G.K. White, *J. Appl. Phys.* 48 (1977) 117.

- [24] H.J. McSkimmin and P. Andreatch, *J. Appl. Phys.* 35 (1964) 2161.
- [25] A.D. Zdetsis, *Chem. Phys.* 40 (1979) 345.
- [26] G. Dolling, in: *Inelastic Scattering of Neutrons in Solids and Liquids*, Vol. 1 (IAEA, Vienna, 1983) p. 37.
- [27] G. Nilsson and G. Nelin, *Phys. Rev. B* 6 (1972) 3777.
- [28] A.D. Zdetsis and C.S. Wang, *Phys. Rev. B* 19 (1979) 2999.
- [29] V.J.B. Torres and A.M. Stoneham, *Handbk. of Interatomic Potentials III* (United Kingdom Atomic Energy Establishment, 1985).
- [30] J. Menendez and M. Cardona, *Phys. Rev. B* 29 (1984) 2051.
- [31] K. Uchinokura, T. Sekine and E. Matsuura, *J. Phys. Chem. Sol.* 35 (1974) 171.
- [32] F.A. Johnson, *Proc. Phys. Soc.* 73 (1959) 265.
- [33] F.A. Johnson and R. Loudon, *Proc. R. Soc. London A* 281 (1964) 274.
- [34] M.G. Holland and L.J. Neuringer, in: *Proc. Intern. Conf. on the Physics of Semiconductors* (Inst. of Phys., London, 1962) p. 475.
- [35] P.H. Keesom and G. Seidel, *Phys. Rev.* 113 (1959) 33.
- [36] G. Feher, *Phys. Rev.* 114 (1959) 1219.
- [37] W. Bludau, A. Onton and W. Heinke, *J. Appl. Phys.* 45 (1974) 1846.
- [38] M.A. Vouk and E.C. Lightowers, *J. Phys. C* 10 (1977) 3689; *J. Lumin.* 15 (1977) 17.
- [39] L. Eaves, R.A. Stradling, J.C. Portal, S. Askenazy, R. Barbaste and K. Hansen, *Solid State Commun.* 15 (1974) 1281.
- [40] J.C. Hensel, H. Hasegawa and M. Nakayama, *Phys. Rev.* 138 (1965) A 225.
- [41] H. Kodera, *J. Phys. Soc. Jpn.* 21 Suppl. (1966) 578.
- [42] T. Nishino, M. Takeda and Y. Hamakawa, *Solid State Commun.* 14 (1974) 627.
- [43] H.D. Barber, *Solid State Electron.* 10 (1967) 1039.
- [44] T. Ohya, T. Yoshihara, K. Murase and R.K. Oksuka, *Phys. Lett. A* 33 (1970) 55.
- [45] J.R. Chelikowsky and M.L. Cohen, *Phys. Rev. B* 10 (1974) 5095.
- [46] G.E. Jellison and F.A. Modine, *Appl. Phys. Lett.* 15 (1982) 180.
- [47] H.R. Philipp and H. Ehrenreich, *Phys. Rev.* 129 (1963) 1550.
- [48] K.L. Shaklee and R.E. Nahory, *Phys. Rev. Lett.* 24 (1970) 942.
- [49] T. Nishino, M. Takeda and Y. Hamakawa, *Solid State Commun.* 12 (1973) 1137.
- [50] N.O. Lipari and M. Altarelli, *Solid State Commun.* 18 (1976) 951.
- [51] G.G. Macfarlane, T.P. Lean, J.E. Quarrington and V. Roberts, *J. Phys. Chem. Solids* 8 (1959) 388.
- [52] M.A. Vouk and E.C. Lightowers, *J. Phys. C* 10 (1977) 3689.
- [53] P.J. Dean, J.R. Haynes and W.F. Flood, *Phys. Rev.* 161 (1967) 711.
- [54] R.B. Hammond, D.L. Smith and T.C. McGill, *Phys. Rev. Lett.* 35 (1975) 1535.
- [55] G.S. Mitchard and T.C. McGill, *Phys. Rev. B* 25 (1982) 5351.
- [56] G. Davies, *J. Phys. Chem. Solids* 31 (1970) 883.
- [57] K. Betzler, *Solid State Commun.* 15 (1974) 1837.
- [58] J.C. Merle, M. Capizzi, P. Fiorini and A. Frova, *Phys. Rev. B* 17 (1978) 4821.
- [59] Ya.E. Pikrovskii and K.I. Svistunova, *Sov. Phys. – Solid State* 13 (1971) 1241.
- [60] A.S. Kaminskii, Ya.E. Pokrovskii and N. Alkeev, *Sov. Phys. – JETP* 32 (1971) 1048.
- [61] R.B. Hammond, T.C. McGill and J.W. Mayer, *Phys. Rev. B* 13 (1976) 3567.
- [62] T.M. Rice, *Solid State Phys.* 32 (1977) 1.
- [63] J.C. Hensel, T.G. Philips and G.A. Thomas, *Solid State Phys.* 32 (1977) 87.
- [64] K. Betzler, T. Weller and R. Conradt, *Phys. Rev. B* 6 (1972) 1394.
- [65] A.G. Steele, W.G. McCullen and M.L.W. Thewalt, *Phys. Rev. Lett.* 59 (1987) 2899.
- [66] A. Hangleiter, *Phys. Rev. Lett.* 55 (1985) 2976.
- [67] L.D. Laude, F.H. Pollack and M. Cardona, *Phys. Rev. B* 3 (1971) 2623.
- [68] V.D. Kulakovskii, I.B. Levinson and V.B. Timofeev, *Sov. Phys. – Solid State* 20 (1978) 230.
- [69] M. Lax and J.J. Hopfield, *Phys. Rev.* 124 (1961) 115.
- [70] M.L.W. Thewalt, U.O. Ziemelis and R.R. Parsons, *Solid State Commun.* 39 (1981) 27.
- [71] R. Sauer, J. Weber, J. Stoltz, E.R. Weber, K.-H. Kusters and H. Alexander, *Appl. Phys. A* 36 (1985) 1.
- [72] M. Suezawa and K. Sumino, *Phys. Stat. Sol. a* 78 (1983) 639.
- [73] T.G. Brown and D.G. Hall, *Appl. Phys. Lett.* 49 (1986) 245.
- [74] T.G. Brown, P.L. Bradfield and D.G. Hall, *Appl. Phys. Lett.* 51 (1987) 1585.
- [75] E.M. Conwell, *Phys. Rev.* 135 (1964) A1138.
- [76] H. Weman, Q.X. Zhao and B. Monemar, *Phys. Rev. B* 36 (1987) 5054.
- [77] H. Weman, B. Monemar and Q.X. Zhao, *Phys. Rev. B* 38 (1988) 61.
- [78] E. Irion, K. Thonke and R. Sauer, *J. Phys. C* 18 (1985) 5069.
- [79] A.T. Collins, *J. Phys. D* 10 (1977) 1143.
- [80] A.M. Stoneham, *Theory of defects in solids* (Clarendon Press, Oxford, 1975).
- [81] R.C. Newman, *Infra-red studies of crystal defects* (Taylor and Francis, London, 1973).

- [82] R.A. Woolley, PhD thesis, Univ. of London, unpublished (1986).
- [83] A.R. Bean and R.C. Newman, Solid State Commun. 9 (1977) 271.
- [84] K.P. O'Donnell and G. Davies, J. Lumin. 26 (1981) 177.
- [85] J. Wagner, K. Thonke and R. Sauer, Phys. Rev. B 29 (1984) 7051.
- [86] J. Wagner, A. Dornen and R. Sauer, Phys. Rev. B 31 (1985) 5561.
- [87] J. Wagner and R. Sauer, Phys. Rev. B 27 (1983) 6568.
- [88] J. Wagner and R. Sauer, Physica B 117–118 (1983) 113.
- [89] J. Wagner, Phys. Rev. B 29 (1984) 2002.
- [90] A.P.G. Hare, G. Davies and A.T. Collins, J. Phys. C 5 (1972) 1265.
- [91] G. Davies, H. Brian, E.C. Lightowers, K. Barraclough and M.F. Thomaz, Semicond. Sci. Technol. (1989), in press.
- [92] G. Davies and M.F. Hamer, Proc. R. Soc. London A 348 (1976) 285.
- [93] J.R. Haynes and W.C. Westphal, Phys. Rev. 101 (1956) 1676.
- [94] A.V. Yukhnevich and V.D. Tkachev, Sov. Phys. – Solid State 7 (1966) 2746.
- [95] T.G. Brown and D.G. Hall, J. Appl. Phys. 59 (1986) 1399.
- [96] A.H. Kalma and J.C. Corelli, Phys. Rev. 173 (1968) 734.
- [97] K. Natarajan and E.L. Heasell, Phys. Stat. Sol. A 28 (1975) 603.
- [98] M. Kleverman, J.-O. Fornell, J. Olnjos, H.G. Grimmeiss and J.L. Lindström, Phys. Rev. B 37 (1988) 10199.
- [99] A.T. Collins and E.C. Lightowers, Phys. Rev. 171 (1968) 843.
- [100] M.L.W. Thewalt, D. Labrie and T. Timusk, Solid State Commun. 53 (1985) 1049.
- [101] M.L.W. Thewalt, S.P. Watkins, U.O. Ziemelis, E.C. Lightowers and M.O. Henry, Solid State Commun. 44 (1982) 573.
- [102] C.E. Jones, D. Schafer, W. Scott and R.J. Hager, J. Appl. Phys. 52 (1981) 5148.
- [103] E.C. Lightowers, private communication (1987).
- [104] Y.H. Lee, L.J. Cheng, J.D. Gerson, P.M. Mooney and J.W. Corbett, Solid State Commun. 21 (1977) 109.
- [105] T. Nozaki, Y. Yatsurugi and N. Akiyama, J. Electrochem. Soc. Solid State Sci. 117 (1970) 1566.
- [106] R.W. Series, K.G. Barraclough, D.T.J. Hurlie, D.S. Kemp and G.J. Rae, unpublished work (1985).
- [107] J.A. Baker, T.N. Tucker, N.E. Moyer and R.C. Buchert, J. Appl. Phys. 39 (1986) 4365.
- [108] R. Jones, J. Phys. C 20 (1987) L713.
- [109] R.C. Newman and J. Wakefield, J. Phys. Chem. Solids 19 (1961) 230.
- [110] U. Gosele and T.Y. Tan, in: Impurity diffusion and gettering in silicon, eds R.B. Fair, Ch.W. Pearce and J. Washburn (Mater. Res. Soc., 1985) p. 105.
- [111] S. Dannefaer, P. Mascher and D. Kerr, Phys. Rev. Lett. 56 (1986) 2195.
- [112] R.C. Newman and J.B. Willis, J. Phys. Chem. Solids 26 (1965) 373.
- [113] R.C. Newman and R.S. Smith, J. Phys. Chem. Solids 30 (1969) 1493.
- [114] T. Nozaki, Y. Yatsurugi and N. Akiyama, Anal. Chem. 4 (1970) 87.
- [115] Y. Endo, Y. Yatshifumi, N. Akiyama and T. Nozaki, Anal. Chem. 44 (1972) 2258.
- [116] Annual Book of ASTM Standards (Am. Soc. for Testing and Materials, Philadelphia, 1981) p. 543.
- [117] A.R. Bean and R.C. Newman, J. Phys. Chem. Solids 33 (1972) 255.
- [118] R.A. Foreman, M.I. Bell, D.R. Myers and D. Chandler-Horowitz, Jpn. J. Appl. Phys. 24 (1985) L848.
- [119] A. Brelot and J. Charlemagne, Rad. Effects 8 (1971) 161.
- [120] A.R. Bean and R.C. Newman, Solid State Commun. 8 (1970) 175.
- [121] A.R. Bean and R.C. Newman, Rad. Effects 8 (1971) 189.
- [122] R.A. Woolley, E.C. Lightowers, A.K. Tipping, M. Claybourn and R.C. Newman, Mater. Sci. Forum 10–12 (1987) 929.
- [123] K. Thonke, R. Teschner and R. Sauer, Solid State Commun. 61 (1987) 241.
- [124] G.D. Watkins and K.L. Brower, Phys. Rev. Lett. 36 (1976) 1329.
- [125] L.C. Kimerling, Inst. Phys. Conf. Ser. 46 (1979) 273.
- [126] Y.H. Lee, L.J. Cheng, J.D. Gerson, P.M. Mooney and J.W. Corbett, Solid State Commun. 21 (1977) 109.
- [127] M.T. Asom, J.L. Benton, R. Sauer and L.C. Kimerling, Appl. Phys. Lett. 51 (1987) 256.
- [128] A.K. Tipping and R.C. Newman, Semicond. Sci. Technol. 2 (1987) 389.
- [129] G. Davies, E.C. Lightowers, M.F. Thomaz and J.G. Wilkes, Semicond. Sci. Technol. 3 (1988) 608.
- [130] G.D. Watkins, private communication (1988).
- [131] G. Davies, E.C. Lightowers, D. Griffiths and J.G. Wilkes, Semicond. Sci. Technol. 2 (1987) 554.
- [132] S.P. Chappell and R.C. Newman, Semicond. Sci. Technol. 2 (1987) 691.
- [133] A.S. Oates, R.C. Newman, J.M. Tucker, G. Davies and E.C. Lightowers, Mater. Res. Soc. Symp. Proc. 59 (1985) 59.
- [134] R.C. Newman, A.S. Oates and F.M. Livingston, J. Phys. C 16 (1983) L667.
- [135] See papers in Proc. Fall Meeting, Mater. Res. Soc. Symp. Proc. 104 (1988).
- [136] J.C. Mikkelsen, Mater. Res. Soc. Symp. Proc. 59 (1986) 19.
- [137] T. Iizuki, S. Takasu, M. Tajima, T. Arai, T. Nozaki, N. Inoue and M. Watanabe, J. Electrochem. Soc. 132 (1985) 1701.
- [138] D.R. Bosomworth, W. Hayes, A.R.L. Spray and G.D. Watkins, Proc. R. Soc. London A 317 (1970) 133.
- [139] M. Stavola, Appl. Phys. Lett. 42 (1983) 73.

- [140] A.K. Tipping, R.C. Newman, D.C. Newton and J.H. Tucker, Mater. Sci. Forum 10–12 (1986) 887.
- [141] D. Mathiot, Mater. Res. Soc. Symp. Proc. 104 (1988) 189.
- [142] Y. Takano and M. Malei, in: Semicond. Silicon 1973, eds H.R. Huff and R.B. Burgess (Electrochem. Soc., Princeton, 1973) p. 469.
- [143] Ph. Vendage, N. Magena and K. Saminadayar, Mater. Res. Soc. Symp. Proc. 59 (1986) 187.
- [144] H. Nakayama, T. Nishino and Y. Hamakawa, Appl. Phys. Lett. 38 (1981) 623.
- [145] A.C.T. Drakeford and E.C. Lightowers, Mater. Res. Soc. Symp. Proc. 104 (1988) 209.
- [146] A.S. Oates, M.J. Binns, R.C. Newman, J.H. Tucker, J.G. Wilkes and A. Wilkinson, J. Phys. C 17 (1984) 5695.
- [147] M.L.W. Thewalt, A.G. Steele, S.P. Watkins and E.C. Lightowers, Phys. Rev. Lett. 57 (1986) 1939.
- [148] A.G. Steele, M.L.W. Thewalt and S.P. Watkins, Solid State Commun. 63 (1987) 81.
- [149] M.O. Henry and E.C. Lightowers, J. Phys. C 10 (1977) L601.
- [150] P.J. Dean, W.F. Flood and G. Kaminsky, Phys. Rev. 163 (1967) 721.
- [151] J.R. Haynes, Phys. Rev. Lett. 4 (1960) 361.
- [152] D.F. Nelson, J.D. Cuthbert, P.J. Dean and D.G. Thomas, Phys. Rev. Lett. 17 (1966) 1262.
- [153] M.L.W. Thewalt, Can. J. Phys. 55 (1977) 1463.
- [154] E.C. Lightowers, M.O. Henry and M.A. Vouk, J. Phys. C 10 (1977) L713.
- [155] M.L.W. Thewalt, G. Kirczenow, R.R. Parsons and R. Barrie, Can. J. Phys. 54 (1976) 1728.
- [156] M. Tajima, Appl. Phys. Lett. 32 (1978) 719.
- [157] A.S. Kaminskii, L.I. Kolesnik, B.M. Leiferov and Ya.E. Pokrovski, J. Appl. Spectrosc. 36 (1982) 516.
- [158] M.L.W. Thewalt, E.C. Lightowers and J.I. Pankove, Appl. Phys. Lett. 46 (1985) 689.
- [159] W. Schmid, Phys. Stat. Sol. b 84 (1977) 529; T. Steiner and M.L.W. Thewalt, Solid State Commun. 49 (1984) 1121.
- [160] M.L.W. Thewalt, Solid State Commun. 23 (1977) 733.
- [161] M.O. Henry and E.C. Lightowers, J. Phys. C 11 (1978) 1555.
- [162] G.K. Kirczenow, Solid State Commun. 21 (1977) 713.
- [163] G.K. Kirczenow, Can. J. Phys. 55 (1977) 1787.
- [164] R.C. Enck and A. Honig, Phys. Rev. 177 (1969) 1182.
- [165] Y.S. Vavilov, O.G. Koshelev, Yu.P. Koval' and Ya.G. Klyava, Sov. Phys. – Solid State 8 (1967) 2770.
- [166] R. Parsons, Solid State Commun. 29 (1979) 763.
- [167] P.E. Schmid, M.L.W. Thewalt and W.P. Durnke, Solid State Commun. 38 (1981) 1091.
- [168] A.V. Yukhnovich and V.D. Tkachev, Sov. Phys. – Solid State 8 (1966) 1004.
- [169] G. Davies, E.C. Lightowers, R.A. Woolley, R.C. Newman and A.S. Oates, J. Phys. C 17 (1984) L499.
- [170] K. Thonke, G.D. Watkins and R. Sauer, Solid State Commun. 51 (1984) 127.
- [171] C.P. Foy, Physica B 116 (1983) 276.
- [172] J.R. Noonan, C.G. Kirkpatrick and B.G. Streetman, J. Appl. Phys. 47 (1976) 3010.
- [173] J.M. Trombetta and G.D. Watkins, Mater. Res. Soc. Symp. Proc. 104 (1988) 93; Appl. Phys. Lett. 51 (1987) 1103.
- [174] S.P. Chappell, M. Claybourn, R.C. Newman and K.G. Barracough, Semicond. Sci. Technol. 3 (1988) 1047.
- [175] C.E. Jones and W.D. Compton, Rad. Effects 9 (1971) 83.
- [176] C.P. Foy, J. Phys. C 15 (1982) 2059.
- [177] K. Thonke, A. Hangleiter, J. Wagner and R. Sauer, J. Phys. C 18 (1985) L795.
- [178] R.A. Faulkner, Phys. Rev. 184 (1969) 713.
- [179] G. Davies, A.S. Oates, R.C. Newman, R. Woolley, E.C. Lightowers, M.J. Binns and J.G. Wilkes, J. Phys. C 19 (1986) 841.
- [179a] B.G. Svensson and J.L. Lindstrom, Phys. Stat. Sol. a 95 (1986) 537.
- [180] Y.H. Lee, J.W. Corbett and K.L. Brower, Phys. Stat. Sol. 41 (1973) 673.
- [181] S.H. Muller, PhD Thesis, Univ. of Amsterdam (1975).
- [182] P.F. Daly and W.P. Knox, private communication (1970).
- [183] L.J. Cheng and P. Vadja, J. Appl. Phys. 40 (1969) 4679.
- [184] C.G. Kirkpatrick and J.R. Noonan, Rad. Effects 30 (1976) 97.
- [185] L.W. Song, B.W. Benson and G.D. Watkins, Mater. Res. Soc. Symp. Proc. 104 (1988) 79; Appl. Phys. Lett. 51 (1987) 1155.
- [186] K.P. O'Donnell, K.M. Lee and G.D. Watkins, Physica B 116 (1983) 258.
- [187] K. Thonke, H. Klemisch, J. Weber and R. Sauer, Phys. Rev. B 24 (1981) 5874.
- [188] K.L. Brower, Phys. Rev. B 9 (1974) 2607; B 17 (1978) 4130.
- [189] A.V. Yukhnovich and A.V. Mudryi, Sov. Phys. – Semicond. 7 (1973) 815.
- [190] C.P. Foy, M.C. do Carmo, G. Davies and E.C. Lightowers, J. Phys. C 14 (1981) L7.
- [191] G. Davies and M.C. do Carmo, J. Phys. C 14 (1981) L687.
- [192] V.D. Tkachev and A.V. Mudryi, Inst. Phys. Conf. Ser. 31 (1977) 231.
- [193] C.E. Jones, E.S. Johnson, W.D. Compton, J.R. Noonan and B.G. Streetman, J. Appl. Phys. 44 (1973) 5402.
- [194] G. Davies, E.C. Lightowers, M.C. do Carmo, J.G. Wilkes and G.R. Wolstenholme, Solid State Commun. 50 (1984) 1057.
- [195] U. Gosele and T.Y. Tan, in: Impurity Diffusion and Gettering in Silicon, eds R.B. Fair, Ch.W. Pearce and J. Washburn (Materials Research Society, Pittsburgh, 1985) p. 105.
- [196] G.W. Ludwig and H.H. Woodbury, Solid State Phys. 13 (1962) 223.

- [197] N.S. Minaev, A.V. Mudryi and V.D. Tkachev, Sov. Phys. – Semicond. 13 (1979) 233.
- [198] R. Sauer and J. Weber, Solid State Commun. 49 (1984) 833.
- [199] S.P. Watkins, U.O. Ziemelis and M.L.W. Thewalt, Solid State Commun. 43 (1982) 687.
- [200] J. Weber, H. Bauch and R. Sauer, Phys. Rev. B 25 (1982) 7688.
- [201] J.A. Rostoworoski and R.R. Parsons, Can. J. Phys. 59 (1981) 496.
- [202] G. Davies, E.C. Lightowers and Z.E. Ciechanowska, J. Phys. C 20 (1987) 191.
- [203] N. Burger, K. Thonke and R. Sauer, Phys. Rev. Lett. 52 (1984) 1645.
- [204] V.D. Tkachev and A.V. Mudryi, J. Appl. Spectrosc. 29 (1979) 1485.
- [205] N.S. Minaev, A.V. Mudryi and V.D. Tkachev, Phys. Stat. Sol. b 108 (1981) K89.
- [206] E.S. Johnson, W.D. Compton, J.R. Noonan and J. Streetman, J. Appl. Phys. 44 (1973) 5411.
- [207] G. Davies, L.T. Canham and E.C. Lightowers, J. Phys. C 17 (1984) L173.
- [208] L.T. Canham, G. Davies and E.C. Lightowers, Inst. Phys. Conf. Ser. 59 (1981) 211.
- [209] M.J. Kane, P.J. Dean and M.S. Skolnick, J. Phys. C 17 (1984) 6127.
- [210] L.T. Canham, G. Davies and E.C. Lightowers, J. Phys. C 13 (1980) L757.
- [211] E.C. Lightowers, L.T. Canham, G. Davies, M.L.W. Thewalt and S.P. Watkins, Phys. Rev. B 29 (1984) 4517.
- [212] I.N. Haddad and P.C. Banbury, Philos. Mag. 14 (1966) 829.
- [213] J.W. Corbett and G.D. Watkins, Phys. Rev. 138 (1965) A555;  
see also B.G. Svensson, J. Svensson, J.L. Linstrom, G. Davies and J.W. Corbett, Appl. Phys. Lett. 51 (1987) 2257.
- [214] J.C. Bourgoin and B. Massarani, Rev. Phys. Appl. 11 (1976) 279.
- [215] I.N. Haddad and P.C. Banbury, Philos. Mag. 14 (1966) 829.
- [216] S.B. Fisher and P.C. Banbury, in: Atomic Collision Phenomena in Solids (North-Holland, Amsterdam, 1970) p. 232.
- [217] L.T. Canham, K.G. Barracough and D.J. Robbins (1988), private communication.
- [218] H. Flicker, J.J. Loferski and J. Scott-Monck, Phys. Rev. 128 (1962) 2557.
- [219] F. Seitz and J.S. Koehler, Solid State Phys. 2 (1956) 305.
- [220] G.D. Watkins, Inst. Phys. Conf. Ser. 23 (1975) 1.
- [221] G.D. Watkins, in: Radiation Damage in Semiconductors (Dunod, Paris, 1964) p. 97.
- [222] R.E. Whan and F.L. Vook, Phys. Rev. 153 (1967) 814.
- [223] F.L. Vook and H.J. Stein, in: Radiation Effects in Semiconductors (Plenum, New York, 1968) p. 99.
- [224] G. Davies, unpublished.
- [225] G.D. Watkins and J.W. Corbett, Phys. Rev. 138 (1965) A543.
- [226] T. Wada, K. Yasuda, S. Ikuta, M. Takeda and H. Masuda, J. Appl. Phys. 48 (1977) 2145.
- [227] A.S. Oates and R.C. Newman, Appl. Phys. Lett. 49 (1986) 262.
- [228] G. Davies, A.S. Oates, R.C. Newman, R. Woolley, E.C. Lightowers, M.J. Binns and J.G. Wilkes, J. Phys. C 19 (1986) 841.
- [229] G.S. Oehrlein, I. Krafcik, J.L. Lindstrom, A.E. Jaworowski and J.W. Corbett, J. Appl. Phys. 54 (1983) 179.
- [230] V.D. Akhmetov and V.V. Bolotov, Phys. Stat. Sol. a 72 (1982) 61.
- [231] G. Davies, E.C. Lightowers, R.C. Newman and A.S. Oates, Semicond. Sci. Technol. 2 (1987) 524.
- [232] G.A. Kholdar, Yu.V. Danovskii, V.V. Konoplyanyi and V.L. Vinetskii, Sov. Phys. – Semicond. 10 (1976) 1016.
- [233] J.L. Benton, M.T. Asom, R. Sauer and L.C. Kimerling, in: Proc. Fall Meeting, Mater. Res. Soc. Symp. Proc. 104 (1988) 85.
- [234] A.R. Bean, S.R. Morrison, R.C. Newman and R.S. Smith, J. Phys. C 5 (1972) 379.
- [235] P.M. Mooney and J.C. Bourgoin, Phys. Rev. B 29 (1984) 1962.
- [236] L.T. Canham and E.C. Lightowers, Mater. Sci. Forum 10–12 (1986) 1099.
- [237] A.V. Mudryi and A.V. Yukhnevitch, Sov. Phys. – Semicond. 7 (1973) 117.
- [238] C.G. Kirkpatrick, J.R. Noonan and B.G. Streetman, Rad. Effects 30 (1976) 97.
- [239] L.T. Canham, G. Davies and E.C. Lightowers, in: Proc. 17th Intern. Conf. on the Physics of Semiconductors (Springer, Berlin, 1985) p. 737.
- [240] G. Davies, E.C. Lightowers, M. Stavola, K. Bergman and B. Svensson, Phys. Rev. B 35 (1987) 2755.
- [241] M.V. Bortnik, V.D. Tkachev and A.V. Yukhnevitch, Sov. Phys. – Semicond. 1 (1967) 290.
- [242] A.A. Kaplyanskii, Opt. Spectrosc. 16 (1964) 329.
- [243] F.S. Ham, private communication (1987).
- [244] U. Lindfelt and A. Zunger, Phys. Rev. B 30 (1984) 1102.
- [245] B.A. Bunker, Mater. Res. Soc. Bull. 13 (2) (1988) 36.
- [246] T.E. Schlessinger, R.J. Hauenstein, R.M. Feenstra and T.C. McGill, Solid State Commun. 46 (1983) 321.
- [247] H.D. Mohring, J. Weber and R. Sauer, Phys. Rev. B 30 (1984) 894.
- [248] J. Weber and P. Wagner, J. Phys. Soc. Jpn. 49 (1980) 263.
- [249] J. Weber, R. Sauer and P. Wagner, J. Lumin. 24/25 (1981) 155.
- [250] T.E. Schlessinger and T.C. McGill, Phys. Rev. B 28 (1983) 3643.
- [251] A. Chantre and D. Bois, Phys. Rev. B 31 (1985) 7979.
- [252] M.O. Henry, E.C. Lightowers, N. Killoran, D.J. Dunstan and B.C. Cavenett, J. Phys. C 14 (1981) L255.
- [253] O.A. Valle do Amaril, A. Antonelli and A. Fazzio, Phys. Rev. B 35 (1987) 6450.

- [254] G. Davies, E.C. Lightowers and M.C. do Carmo, *J. Phys. C* 16 (1983) 5503.
- [255] A.A. Maradudin, *Solid State Phys.* 18 (1966) 273.
- [256] H. London, *Z. Phys. Chem.* 16 (1958) 302.
- [257] D.E. McCumber and M.D. Sturge, *J. Appl. Phys.* 34 (1963) 1682.
- [258] Z. Ciechanowska, G. Davies and E.C. Lightowers, *Solid State Commun.* 49 (1984) 427.
- [259] G. Davies, *J. Phys. C* 17 (1987) 6331.
- [260] S.P. Watkins and M.L.W. Thewalt, *Can. J. Phys.* 63 (1985) 1074.
- [261] S.P. Watkins, M.L.W. Thewalt and T. Steiner, *Phys. Rev. B* 29 (1984) 5727.
- [262] K. Thonke, private communication (1986).
- [263] V.D. Tkachev, A.V. Mudryi and N.S. Minaev, *Phys. Stat. Sol. a* 81 (1984) 313.
- [264] N. Burger, E. Irion, A. Teschner, K. Thonke and R. Sauer, *Phys. Rev. B* 35 (1987) 3804.
- [265] A.M. Stoneham, *Rev. Mod. Phys.* 41 (1969) 82.
- [266] J.D. Eshelby, *Solid State Phys.* 3 (1956) 79.
- [267] A.M. Stoneham, *Proc. Phys. Soc.* 89 (1966) 909.
- [268] G. Davies, *J. Phys. D* 4 (1971) 1340.
- [269] N.E. Moyer and R.C. Buschert, in: *Radiation Effects in Semiconductors*, ed. F.L. Vook (Plenum, New York, 1968) p. 445.
- [270] M.C. do Carmo, private communication (1988).
- [271] K. Thonke, N. Burger, G.D. Watkins and R. Sauer, in: *Proc. 13th Intern. Conf. on Defects in Semiconductors* (Metallurgical Soc. of AIME, Warrendale, PA, 1985).
- [272] G. Davies, E.C. Lightowers, R. Woolley, R.C. Newman and A.S. Oates, in: *Proc. 13th Intern. Conf. on Defects in Semiconductors* (Metallurgical Soc. of AIME, Warrendale, PA, 1985) p. 725.
- [273] L.T. Canham, G. Davies and E.C. Lightowers, in: *Proc. 13th Intern. Conf. on Defects in Semiconductors* (Metallurgical Soc. of AIME, Warrendale, PA, 1985) p. 847.
- [274] A. Dornen, G. Pensl and R. Sauer, *Phys. Rev. B* 35 (1987) 9318.
- [275] M. Tajima, *Jpn. J. Appl. Phys.* 21 Suppl. 1 (1982) 113.
- [276] R.B. Hammond and R.N. Silver, *Appl. Phys. Lett.* 36 (1980) 68.
- [277] J.J. van Kooten, T. Gregorkiew, A.J. Blakmeer and C.A.J. Ammerlaan, *J. Phys. C* 20 (1987) 2183.
- [278] K. Kosai and M. Gershenson, *Phys. Rev. B* 9 (1974) 723.
- [279] V.I. Obodnikov, L.N. Safronov and L.S. Smirnov, *Sov. Phys. – Semicond.* 10 (1976) 814.
- [280] M.O. Henry and E.C. Lightowers, *J. Phys. C* 13 (1980) 2215.
- [281] M.L.W. Thewalt, *Solid State Commun.* 28 (1978) 361.
- [282] J. Weber and H.J. Queisser, *Mater. Res. Soc. Symp. Proc.* 59 (1986) 147.
- [283] G.S. Mitchard, S.A. Lyon, K.R. Elliott and T.C. McGill, *Solid State Commun.* 29 (1979) 425.
- [284] J.A. Rostworowski and R.R. Parsons, *Can. J. Phys.* 59 (1981) 496.
- [285] K.R. Elliott, *Phys. Rev. B* 25 (1982) 1460.
- [286] J.I. Pankove and C.P. Wu, *Appl. Phys. Lett.* 35 (1980) 937.
- [287] N.S. Minaev and A.V. Mudryi, *Phys. Stat. Sol. a* 68 (1981) 561.
- [288] H. Werner, B. Monemar and P.O. Holtz, *Appl. Phys. Lett.* 47 (1985) 1110.
- [289] M.O. Henry, K.G. McGuigan and R.C. Barklie, *Solid State Commun.* 64 (1987) 31.
- [290] K.G. McGuigan et al., submitted to *Solid State Commun.* (1988).
- [291] N. Magnea, A. Lazrak and J.L. Pautrat, *Appl. Phys. Lett.* 45 (1984) 60.
- [292] J. Weber and G.D. Watkins, in: *Proc. 13th Int. Conf. on Defects in Semiconductors* (Metallurgical Soc. of AIME, Warrendale, PA, 1985) p. 661.
- [293] P. Clifton, G. Davies and E.C. Lightowers, *J. Phys. C* 17 (1984) L889.
- [294] H. Conzelman, *Appl. Phys. A* 30 (1983) 169.
- [295] D. Thebault, J. Barrau, G. Armelles, N. Lauret and J.P. Noguier, *Phys. Stat. Sol. b* 125 (1984) 357.
- [296] R. Mitra, private communication (1988).
- [297] A. Dornen, R. Sauer and G. Pensl, *Mater. Res. Soc. Symp. Proc.* 59 (1986) 545.
- [298] H. Conzelman, *Appl. Phys. A* 42 (1987) 1.

### Notes added in proof

Table 1 on radiative decay time measurements should be extended to include data on the 1018 meV “W” series of luminescence lines (sections 5.4 and 9.2). At low temperatures ( $T < 40$  K) the luminescence initially decays exponentially, with time constants  $28 \pm 2$  ns for each of the lines at the

basic W centre (1018 meV), and at the modified centres produced by He, Ne and Ar. For Kr the decay time is  $34 \pm 2$  ns. At longer times after excitation, the luminescence decays as for the free exciton, implying that excitation of the centres occurs through capture of the excitons. (G. Bohnert, A. Hangleiter, K. Weronek and K. Thonke, Mat. Sci. Forum 38–41 (1989) 361)

Tables 3 and 4 should be extended to include data by W. Kurner (Diploma thesis, University of Stuttgart, 1988) on the isotope shift of  $^{18}\text{O} - ^{16}\text{O} = + 0.024$  meV in the 789 meV ‘‘C’’ line. There is also a C isotope effect in its resonant phonon mode of quantum 30.9 meV, with  $^{13}\text{C} - ^{12}\text{C} = - 0.1$  meV.

The diffusion of carbon has been remeasured by F. Rollert, N.A. Stolwijk and H. Mehrer (Mat. Sci. Forum 38–41 (1989) 753) in close agreement with eq. (40).

The ‘‘branching ratio’’ modelling of reactions induced by radiation damage (section 6.5) has been extended by L.C. Kimerling, M.T. Asom, J.L. Benton, P.J. Drevinsky and C.E. Caefter (Mat. Sci. Forum 38–41 (1989) 141), including discussion of the relative magnitudes of the capture radii. Recent work on the annealing of radiation damage has emphasised the importance of the self-interstitial condensations which have aggregated on carbon-related centres during the irradiation (G. Davies and Kwok Tat Kun, Semicond. Sci. Technol. 4 (1989), in press). These aggregates (containing two or more self-interstitials) have still not been observed directly by spectroscopic methods; their decomposition during annealing can initiate further defect reactions.

Radiation-induced complexes involving Al have been reported by Latushko and Petrov (Mat. Sci. Forum 38–41 (1989) 1169) to give strong electronic absorption. Line series ‘‘AM1’’ (lowest energy line at  $774.8 \pm 0.1$  meV) and ‘‘AM2’’ (starting at  $797.6 \pm 0.2$  meV) are suggested to be transitions to shallow excited states of an electron on a singly ionised double donor formed by interstitial Al. The defect is stable in tetrahedral symmetry in the AM1 configuration, and in a lower symmetry for AM2.

The N1 (746 meV) and N5 (773 meV) centres have been confirmed as having monoclinic I symmetry (A. Dornen, R. Sauer and G. Pensl, Mat. Sci. Forum 38–41 (1989) 631). The N2 (758 meV) and N3 (762 meV) centres have lower symmetry and appear to be formed when an oxygen atom is placed near an N5 or N1 centre, respectively; the parent N2 and N3 centres contain nitrogen and carbon.

A detailed study of the 1060 meV photoluminescence system has been reported by W. Kurner, R. Sauer, K. Thonke, M.T. Asom and W. Zulehner (Mat. Sci. Forum 38–41 (1989) 159). Isotope shifts in the zero-phonon line of  $^{18}\text{O} - ^{16}\text{O} = + 0.04$  meV and  $^{13}\text{C} - ^{12}\text{C} = 0.14$  meV confirm the presence of these elements in this radiation damage centre. The centre is shown to be similar to the 789 meV ‘‘C’’ centre (section 5.1).

The photoluminescence lines labelled ‘‘TD’’ near 1143 meV [5] are suggested to occur at a boron–oxygen complex, the oxygen being in the form of thermal donors (A. Henry, H. Weman and B. Monemar, in: Proc. 3rd Intern. Conf. on Shallow Defects in Semiconductors, Inst. Phys. Conf. Ser. (1989); to be published). The ‘‘TD’’ lines could be the boron-related equivalents of the Al–O complexes proposed in ref. [145].

Band gap narrowing caused by the heavy strain in H-implanted silicon has been suggested to be the origin of the shift of  $-130$  meV of excitons trapped on shallow impurities (P, B or In). (M. Singh, J. Weber, M. Konuma and H. Cerva, Mat. Sci. Forum 38–41 (1989) 1033)